Chair of Physical Metallurgy and Metallic Materials

Master's Thesis

A tailored TiAl alloy for the powder bed based laser additive manufacturing

David Erich Schimbäck, BSc

March 2019

EIDESSTATTLICHE ERKLÄRUNG

Ich erkläre an Eides statt, dass ich diese Arbeit selbständig verfasst, andere als die angegebenen Quellen und Hilfsmittel nicht benutzt, und mich auch sonst keiner unerlaubten Hilfsmittel bedient habe.

Ich erkläre, dass ich die Richtlinien des Senats der Montanuniversität Leoben zu "Gute wissenschaftliche Praxis" gelesen, verstanden und befolgt habe.

Weiters erkläre ich, dass die elektronische und gedruckte Version der eingereichten wissenschaftlichen Abschlussarbeit formal und inhaltlich identisch sind.

Datum 21.03.2019

Unterschrift Verfasser/in
David Erich, Schimbäck
Matrikelnummer: 01335152

Acknowledgements

"A scientist in his laboratory is not a mere technician: he is also a child confronting natural phenomena that impress him as though they were fairy tales."

Marie Sklodowska Curie, (1867 – 1934)

A great number of people have helped me actively or with technical discussions to conduct this work. I would like to thank the most important ones:

First and foremost, I would like to thank my supervisors assoc.Prof. Dipl.-Ing. Dr.mont. Svea Mayer and Univ.-Prof. Dipl.-Ing. Dr.mont. Helmut Clemens for the technical support. Without the constant discussions and the technical input, the work would not have been possible in this form. Furthermore, I would like to thank the team of the Institute for Mechatronics from the University of Innsbruck with Univ.-Prof. Dipl.-Ing. Dr. Gerhard Leichtfried, Jakob Braun, MSc. and Lukas Kaserer, MSc. for their active support and the provision of the additive manufactured samples. Likewise, great thanks go to the TiAl working group of the Chair of Physical Metallurgy and Metallic Materials. Especially the support of the PhD students Dipl.-Ing. David Wimler and Dipl.-Ing. Reinhold Wartbichler, who have supported me through technical discussions and interpreting results anytime. Furthermore, I would like to thank the technical staff of the chair, above all Silvia Pölzl in metallography, Gerhard Hawranek at the scanning electron microscope and Bruno Krajnc during the creep tests and for any technical support.

Last but not least, I would like to thank my friends, fellow students, and my family for their moral support throughout my studies. I especially want to thank my parents Regina and Josef Schimbäck. The fulfillment of my dreams during the last years was always supported by them. Without this moral and financial support, my studies would never be conceivable in this form and private successes would not have been possible. For this reason, I would like to dedicate this work in deepest gratitude to my beloved parents.

"Ein Gelehrter in einem Laboratorium ist nicht nur ein Techniker, er steht auch vor den Naturgesetzen wie ein Kind vor einer Märchenwelt."

Marie Sklodowska Curie, (1867 – 1934)

Eine Vielzahl an Menschen haben mir durch tatkräftige Hilfe oder fachliche Diskussionen geholfen, diese Arbeit durchzuführen, wobei den Wichtigsten hier gedankt sei:

Zuallererst möchte ich mich bei meinen Betreuern assoz.Prof. Dipl.-Ing. Dr.mont. Svea Mayer und Univ.-Prof. Dipl.-Ing. Dr.mont. Helmut Clemens für die fachliche Unterstützung bedanken. Ohne die ständigen Gespräche und den fachlichen Input wäre diese Arbeit in der Form nicht möglich gewesen. Des Weiteren möchte ich mich bei dem Team des Instituts für Mechatronik der Universität Innsbruck rund um Univ.-Prof. Dipl.-Ing. Dr. Gerhard Leichtfried, Jakob Braun, MSc. und Lukas Kaserer, MSc. für die tatkräftige Unterstützung und das zur Verfügung stellen der additiv gefertigten Proben bedanken. Ebenso gilt größter Dank der TiAl-Arbeitsgruppe des Lehrstuhls für Metallkunde und metallische Werkstoffe.

Hierbei soll vor allem die Unterstützung der Doktoranden Dipl.-Ing. David Wimler und Dipl.-Ing. Reinhold Wartbichler erwähnt werden, die mich durch fachliche Diskussionen beim Interpretieren der Messergebnisse zu jeder Zeit unterstützt haben. Des Weiteren gilt mein Dank den technischen Mitarbeitern des Lehrstuhls, vor allem Silvia Pölzl in der Metallographie, Gerhard Hawranek am Rasterelektronenmikroskop und Bruno Krajnc bei der Durchführung der Kriechtests und bei jeglichen fachlichen Diskussionen.

Zu guter Letzt möchte ich mich bei meinen Freunden, Studienkollegen und meiner Familie bedanken, die mich bei der Durchführung der Arbeit und durch das ganze Studium moralisch begleitet und unterstützt haben. Ohne deren Hilfe in oft schwierigen Zeiten wäre ich nicht an diesem Punkt angekommen. Besonders möchte ich hier meinen Eltern Regina und Josef Schimbäck danken. Die Erfüllung meiner Träume während der letzten Jahre wurde stets von Ihnen mitgetragen und finanziell unterstützt. Ohne diese moralische und finanzielle Unterstützung wäre mein Studium in dieser Form niemals denkbar und die privaten Erfolge nicht möglich gewesen. Aus diesem Grund möchte ich diese Arbeit in tiefster Dankbarkeit meinen geliebten Eltern widmen.

Contents

Abbreviations and Symbols

5xxx ..... *aluminum alloy with magnesium as main alloying element*
A3 ..... *electrolyte for electropolishing*
AC ..... *air cooling*
A_e ..... *elastic contribution to the occuring strain*
A_f (t) ..... *time depending contribution to the occuring strain*
A_i ..... *inelastic contribution to the occuring strain*
Al ..... *aluminum*
Al_2O_3 ..... *aluminum oxide*
AlMgSc ..... *aluminum alloy with magnesium and scandium as main alloying elements*
AM ..... *additive manufacturing*
at.% ..... *atomic percent*
b ..... *sample width, exponential fitting parameter for the primary creep stage*
B ..... *boron*
bcc ..... *body centered cubic*
BDTT ..... *brittle-to-ductile transition temperature*
c ..... exponential fitting parameter for the ternary creep stage
C ..... *carbon*
CAD ..... computer-aided design
CO_2 ..... *carbon dioxide*
CORSIA ..... *carbon offsetting and reduction scheme for international aviation*
Cu K-α ..... *X-ray energy used on labscale instruments*
d ..... *sample height*
D ..... *duplex*
d_{50} ..... *mean particle diameter*
d_{HV} ..... *arithmetic mean of the two diagonals (vickers hardness)*
DIN ..... *German Institute for Standardization (Deutsches Institut für Normung)*
d_{lam} ..... *lamellar spacing*
D_s ..... *powder layer thickness*
DSC ..... *differential scanning calorimetry*
EBM ..... *electron beam melting*
EBSD ..... *electron backscatter diffraction*
EDX ..... *energy dispersive x-ray spectroscopy*
EIGA ..... *electrode induction melting gas atomization*
EN ..... *European Standard*
EU ..... *European Union*
E_V ..... *volume energy*
f ..... *exponential fitting parameter for the ternary creep stage*
F ..... *force*
FC ..... *furnace cooling*
FL ..... *fully lamellar*
GE ..... *General Electrics*
GTF ..... *geared turbofan*
hcp ..... *hexagonal closest packed*
HIP ..... *hot isostatic pressing*
HPC ..... high pressure compressor
HPT ..... high pressure turbine

h_s ..... *hatch distance*
HT ..... *heat treatment*
HV10 ..... *Vickers hardness with 10 kilopond testing force*
IATA ..... *International Air Transport Association*
ICAO ..... *International Civil Aviation Organization*
IM ..... *ingot metallurgy*
ISO ..... *International Organization for Standardization*
K_0 ..... *material constant for the minimum of creep rate*
K_1 ..... *fitting parameter for the primary creep stage*
K_2 ..... *fitting parameter for the secondary creep stage*
K_3 ..... *fitting parameter for the ternary creep stage*
k_y ..... *strengthening coefficient*
L ..... *support distance*
LOM ..... *light optical microscopy*
LPC ..... low pressure compressor
LPT ..... *low pressure turbine*
M_b ..... *bending moment*
Mo ..... *molybdenum*
Nb ..... *niobium*
NG ..... *near gamma*
NLγ ..... *nearly lamellar gamma*
NNS ..... *near net shape*
NO_x ..... *nitrogen oxides*
O ..... *oxygen*
P_L ..... *laser power*
PM ..... *powder metallurgy*
ppm ..... *parts per million*
Q_L ..... *lattice diffusion coefficient*
R ..... *gas constant*
ROI ..... region of interest
RT ..... *room temperature*
SEM ..... *scanning electron microscopy*
s_i ..... *island size*
Si ..... *silicon*
SiC ..... *silicon carbide*
SL ..... *single line*
SLM ..... *selective laser melting*
T ..... *temperature*
T_{abs} ..... *absolute Temperature*
TEM ..... *transmission electron microscopy*
T_{eut} ..... *eutectoide temperature*
Ti ..... *titanium*
Ti_2AlC ..... *hexagonal carbide*
Ti_3AlC ..... *perovskite-type carbide*
TiAl ..... *titanium aluminides*
TiB ..... *titanium monoboride*
TNM ..... *titanium aluminide alloy (Ti-Al-Nb-Mo)*
TNM^+ ..... *TNM alloy with additions of C and Si*

$T_{\gamma,solv}$ ..... *dissolution temperature of the γ phase*
v_s ..... *scanning speed*
W ..... *section modulus*
wt. ..... *weight*
XRD ..... *X-ray diffraction*
α_2' ..... *martensitic type of α_2 phase*
α_2-Ti_3Al ..... *ordered intermetallic TiAl phase with hexagonal $D0_{19}$ structure*
α_m ..... *massive type of α_2-phase*
α-TiAl ..... disordered intermetallic TiAl phase with hexagonal A3 structure
β_o-TiAl ..... *ordered intermetallic TiAl phase with cubic B2 structure*
β-TiAl ..... disordered intermetallic TiAl phase with cubic A2 structure
γ_m ..... *massive type of γ-phase*
γ-TiAl ..... ordered intermetallic TiAl phase with face centered tetragonal $L1_0$ structure
$\dot{\varepsilon}_{min}$ ..... *minimum of creep strain rate*
ε(t) ..... *time dependent strain*
ζ-Ti_5Si_3 ..... *hexagonal silicide with $D8_8$ structure*
σ ..... *yield stress*
σ_0 ..... *stress for dislocation movement in a single crystal structure*
ω_o-Ti_4Al_3Nb ..... *ordered intermetallic TiAl phase with $B8_2$ structure*

1 Introduction

The awareness of the importance in mitigating climate change in the context of its man-made origins found the way into the aviation and automotive industry. According to the International Air Transport Association IATA, air transport, for example, accounts for 2% of the global CO_2 emissions and 3% of the total EU greenhouse gas emissions [1]. The forecast of the International Civil Aviation Organization ICAO predicts a grow of the emissions by 2050 by further 300 - 700%. In 2017, civil aviation emitted around 859 million tons of CO_2 [2]. Due to the increasing number of worldwide annual air passengers, which is estimated to 7.8 billion in 2036, ICAO saw itself forced to implement a global design certification standard named CORSIA (Carbon Offsetting and Reduction Scheme for International Aviation) for the first time coming into effect in 2020 for new aircraft type designs to govern CO_2 emissions [1–3]. The aim of this regulation is to set limits to the CO_2 emissions for each aircraft regarding size and weight. Furthermore, aircraft manufacturers are forced to reduce fuel consumptions in order to gain competitive advantage and cut operating costs for airlines.

To fulfill the obligations established by such regulations concerning lower emissions of CO_2 and NO_x along with a decline of noise on the one hand, as well as economic feasibility on the other hand, research and development activities for the next generation of aircraft engines have been set up. One special focus was placed, in this context, on innovative structural materials in the course of new and improved design concepts, as they play a major role concerning the reduction of weight, fuel consumption and emissions, respectively. Due to their attractive properties, like high specific yield strength, high specific Young's Modulus, good creep properties up to higher temperatures, good oxidation resistance and resistance against "titanium fire", intermetallic β-solidifying titanium aluminides based on the ordered γ-TiAl phase appear to be promising for high temperature service. Especially their high strength level up to 800°C at a low density of 3.9 – 4.2 g/cm³ (depending on composition and constitution) make them superior to the currently used heavy Ni-based alloys as stated in Ref. [4–8] and shown in Figure 1. As a result, this group of alloy has already attracted the attention of the US Air Force in the 1980s and was commercially used 2011 in aircraft engines for the first time by General Electric (GE) [4,5]. GE put cast blades of the 2nd generation TiAl-alloy Ti-48Al-2Nb-2Cr [at.%] into service for the last stages of the low-pressure turbine (LPT) of the GEnx™-engine [4]. Recently, forgeable 3rd generation TiAl-alloys, where also the TNM-alloy Ti-43.5Al-4Nb-1Mo-0.1B [at.%] belongs, are used by Pratt & Whitney for the last LPT stage of the Geared Turbofan™ (GTF) engine, see Figure 2 [5,9].

Over the last decades, the manufacturing and processing routes were mainly driven by ingot metallurgy and forging. The TNM alloy was especially developed to be hot-die forged under near-conventional conditions on existing facilities [5]. However, relatively new fabrication techniques, like Additive Manufacturing (AM), can be seen as a promising approach to overcome processing difficulties of the casting or forging route [10]. This process is based on computer aided design (CAD) manufacturing of parts from formless material, e.g. metal

powders in a layer by layer approach. Qualified powder-based AM-techniques to process γ-TiAl alloys are for instance Electron Beam Melting (EBM) and Selective Laser Melting (SLM) [9].

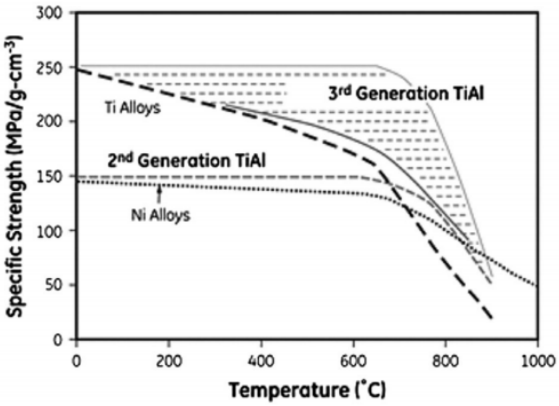

Figure 1: Comparison between Nickel-, Titanium-based alloys, 2nd and 3rd generation TiAl alloys concerning the specific strength as a function of the temperature, reprinted from Ref. [4], Copyright (2019), with permission from Taylor & Francis Group.

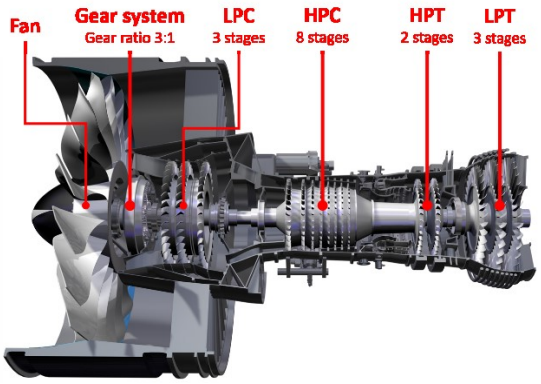

Figure 2: Cross-section of the Pratt & Whitney Geared Turbofan™ (GTF) PW1100G engine according to [11] with Fan, Gear system, Low Pressure Compressor (LPC), High Pressure Compressor (HPC), High Pressure Turbine (HPT) and Low Pressure Turbine (LPT).

Beside processing near-net shape (NNS) parts, the possibility of producing complex components in large numbers, which are not feasible with ingot metallurgy (IM) and require, in many cases, no mechanical post-processing, is one of the most important advantages, particularly regarding economically rapid manufacturing and weight-saving. By producing bionic structures with AM-techniques, allowing the designer of the future to consider entirely new and thus unconventional design options, weight reductions of up to 45% are already accessible [12]. The additive manufacturing of γ-TiAl alloys, in particular SLM, was already examined in literature [13–17]. At this point it should be particularly mentioned that difficulties with regard to pores and crack formation occur during the solidification and subsequent cooling due to induced thermal stresses. Thus, the heating of the baseplate of the SLM machine is essential, if crack formation should be reduced to a minimum. Therefore, SLM-produced TNM-samples are subject of this work and will be investigated in terms of the influence of manufacturing parameters, like laser power and scanning speed, on microstructure and crack formation during the process.

2 Fundamentals

To understand and evaluate the microstructural features of the AM-processed TNM-alloy, profound fundamentals of intermetallic titanium aluminides and a basic knowledge of the Selective Laser Melting (SLM) process is of great importance and will be discussed in the following chapters.

2.1 Titanium Aluminides

Basically, TiAl is an intermetallic compound consisting of Titanium and Aluminum. The metallic bonding has a share of ionic or atomic bonding, whereby the metal character decreases and thus also the ductility, whereas the hardness increases. The mixed bond results in a high stiffness (Young's Modulus) at high temperatures, as well as resistance to creep and oxidation [18]. Considering the Ti-Al binary phase diagram according to the assessments of Schuster and Palm [19] (see Figure 3), the important alloy range for technical (engineering) γ-TiAl based alloys is about 42 – 49 at.% Al. Within this range, two different types of solidification are evident. For Al-contents above 45 at.%, a peritectic solidification ($L + \beta \rightarrow \alpha$) takes place. This type of solidification is prone to segregation. Therefore, Al-contents below 45 at.% are used in the case of the TNM alloy to avoid this peritectic reaction and solidification takes place through the body centered cubic (bcc) β-phase ($L + \beta \rightarrow \beta$) [9].

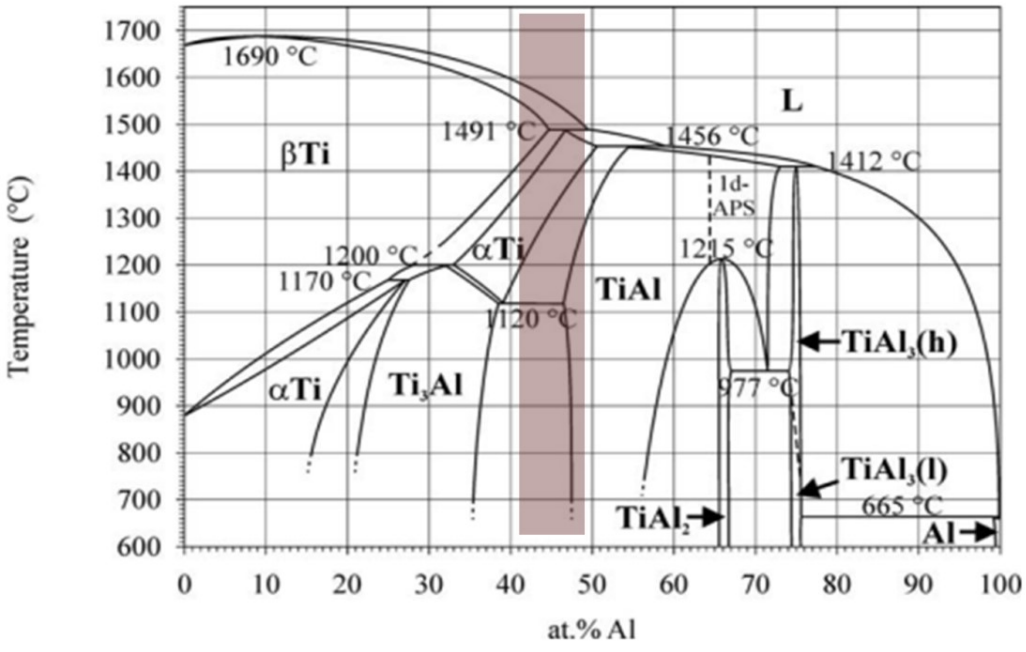

Figure 3:Binary Ti-Al phase diagram according to the assessment of Schuster and Palm [19] – the red area marks the important alloy range for technical γ-TiAl based alloys..

At further decreasing of the temperature, equiaxed hcp α-grains precipitate at the grain boundaries of the β-grains and grows according to the Burgers orientation relationship [20]:

$$\{110\}_\beta || (0001)_\alpha \text{ and } < 111 >_\beta \; || \; < 11\bar{2}0 >_\alpha$$

This leads to an intrinsic grain refinement and as the β-phase provides a number of independent slip systems and further suppresses grain growth, hot-working and heat treatments will be conducted within the (α + β)-phase field region [9]. In theory, there could be 12 different α-variants to be grown, but as the coherency at the interfaces of bcc β-matrix and hcp α-phase is very low and therefore the energy barrier very high, only a few variants can nucleate. Therefore, α-laths band together to form larger α-grains [21]. Furthermore, at subsequent cooling diffusion-controlled precipitation of the γ-phase ($L1_0$ lattice) from the α-phase occurs during the phase formation sequence $\alpha \rightarrow \alpha + \gamma \rightarrow \alpha_2 + \gamma$ according to the Blackburn orientation relationship [20]:

$$(0001)_\alpha || \{111\}_\gamma \text{and} < 11\bar{2}0 >_\alpha || < 1\bar{1}0]_\gamma$$

Beside the formation of γ lamellae, fine lens-shaped γ-grains can be observed in the β_o-phase, depending on the cooling rate. Underneath the ordering temperature, the disordered α- and β-phase exist as ordered α_2-Ti_3Al with $D0_{19}$-structure and as β_o-TiAl with B2-structure. An overview of the structures of all occurring phases is given in Figure 4 and an illustration of the orientation relationships is given in Figure 5 and Figure 6.

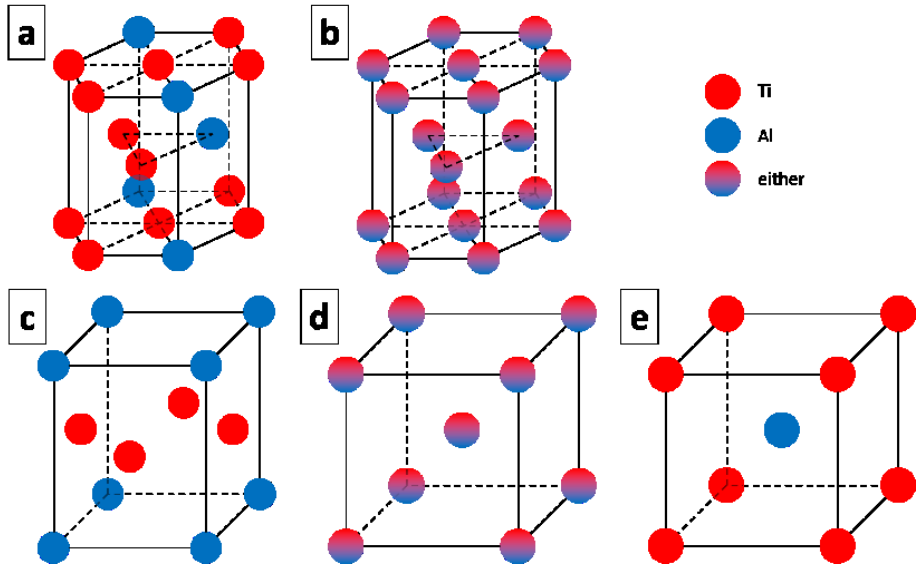

Figure 4: Important structures of the TNM alloy system: (a) hexagonal $D0_{19}$ $\alpha_2 - Ti_3Al$; (b) hexagonal A3 $\alpha - TiAl$; (c) face-centered tetragonal $L1_0$ $\gamma - TiAl$; (d) body-centered cubic A2 $\beta - TiAl$; (e) body-centered cubic B2 $\beta_o - TiAl$.

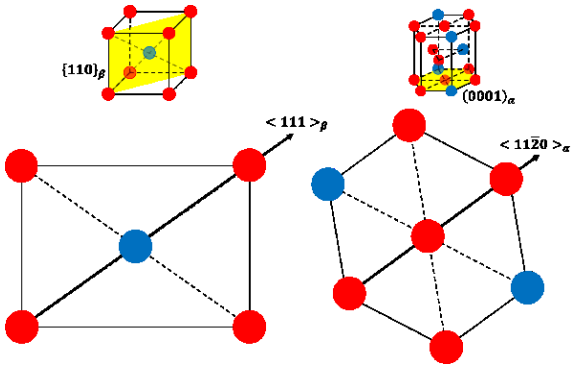

Figure 5: Illustration of the Burgers orientation relation.

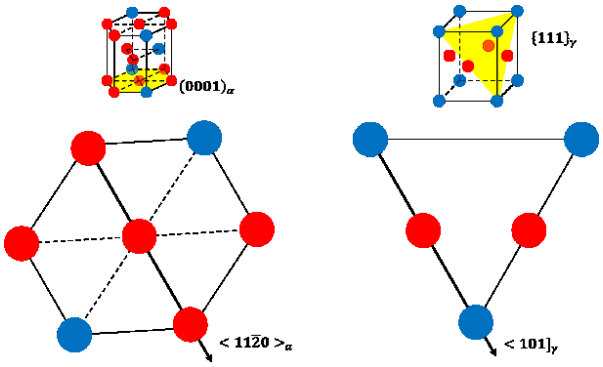

Figure 6: Illustration of the Blackburn orientation relation.

2.2 The TNM Alloy System

TNM-alloys (TNM = TiAl – Nb – Mo) are a β-solidifying γ-TiAl based alloy with an improved hot-workability. The nominal composition of TNM-alloys is Ti-43.5Al-4Nb-1Mo-0.1B [9] and as stated by Schwaighofer et al. [20], the associated quasi-binary phase diagram as well as the development of the phase fractions as a function of the temperature can be seen in Figure 7. The solidification path can be described as following: $L \rightarrow L+\beta \rightarrow \beta \rightarrow \alpha+\beta \rightarrow \alpha+\beta+\gamma \rightarrow \alpha+\beta+\beta_o+\gamma \rightarrow \alpha+\beta_o+\gamma \rightarrow \alpha+\alpha_2+\beta_o+\gamma \rightarrow \alpha_2+\beta_o+\gamma$.

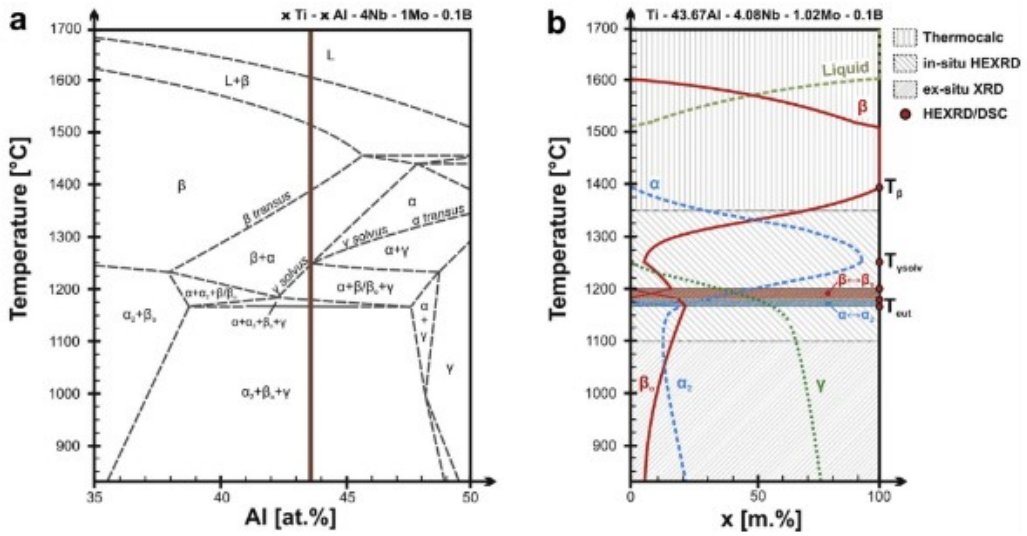

Figure 7: (a) quasi-binary section of the TNM alloy system and (b) phase fractions as a function of the temperature for the investigated alloy composition Ti-43.67Al-4.08Nb-1.02Mo-0.1B; reprinted from Ref. [20], Copyright (2014), with permission from Elsevier.

2.2.1 Heat Treatment and Microstructure

The recommended heat treatment of advanced γ-TiAl based alloys is performed in two steps starting from a fine-grained and isotropic as-cast and hot isostatic pressed (HIP) material. In the first step, the alloy is annealed in the α or $(\alpha+\beta+\gamma)$ phase field region, followed by air cooling (AC). After this step, a microstructure with supersaturated α_2-grains is obtained. The following ageing treatment within the $(\alpha_2+\beta_o+\gamma)$ phase field region causes the formation of ultra-fine lamellar α_2/γ-colonies by the decomposition of the supersaturated α_2-grains [20].

The properties of all advanced TiAl alloys is based on the microstructural features, such as colony size and shape, lamellar spacing or amount of globular γ-grains. Within the heat treatment strategy, four different types of microstructures can be obtained in engineering γ-TiAl based alloys. With increasing annealing temperature, the microstructures change from Near Gamma (NG) to Duplex (D), Nearly Lamellar γ (NLγ) and Fully Lamellar (FL) [22]. At annealing temperatures slightly above the eutectoid temperature, a NG-microstructure is formed with equiaxed and fine-grained microstructural constituents, resulting in a good deformability at elevated temperature. Increasing the temperature, a D-microstructure can be obtained, consisting of globular γ-TiAl grains and α_2/γ-colonies but also of a small volume fraction of α_2 and limited amounts fine equiaxed β_o grains at the colony and γ-grain

boundaries. At this point, the lamellar spacing in the colonies is dependent on the applied cooling rate. Annealing slightly below or above the γ-solvus temperature can produce a NL- or FL-microstructure, whereas the heat treatment in the single α-phase field is prone to extraordinary grain growth. In terms of balanced mechanical properties as creep resistance at elevated temperature and ductility below the brittle-to-ductile transition temperature (BDTT), a concept of a NLγ microstructure was developed and is schematically shown in Figure 8 [9]. This microstructure is characterized by a small volume fraction of globular γ and β_o grains and equiaxed lamellar α_2/γ-colonies with a fine lamellar spacing and can be obtained by the above mentioned two step heat treatment.

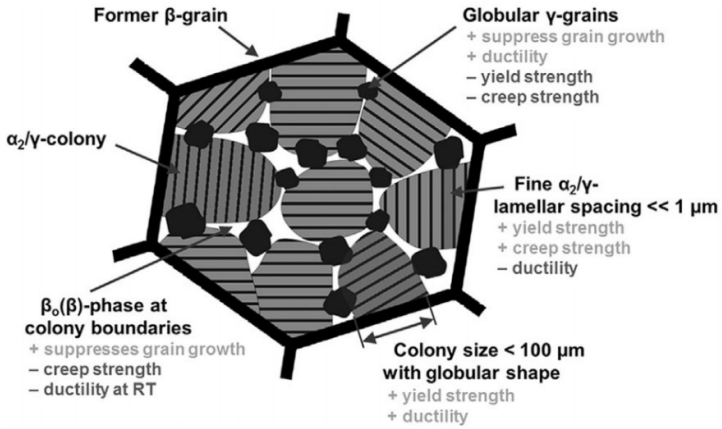

Figure 8: Schematic sketch of a NL + γ – microstructure; reprinted from Ref. [9], Copyright (2017), with permission from Advanced Engineering Materials.

The size of the mean interface spacing of the colonies are in the range of 15 – 30 nm. The lamellar spacing has a major impact on the creep resistance and yield strength, as the interfaces are obstacles for dislocation movement. Therefore, this effect can be described by the modified Hall-Petch relation as shown in equation *(2.1)* [18]:

$$\sigma = \sigma_0 + \frac{k_y}{\sqrt{d_{lam}}}, \tag{2.1}$$

where σ is the yield stress, σ_0 is the resistance of the lattice to dislocation movement, k_y is a material dependent constant and d_{lam} is the lamellar spacing.

Furthermore, to provide sufficient hot-workability, the β-phase at hot-working temperature is inevitable. Therefore, the forging temperature has to be chosen adequately to be in the $(\alpha + \beta)$- or in the $(\alpha + \beta + \gamma)$-phase field region. Within the bcc β-phase, there are a number of independent slip systems, which are necessary to be activated to carry the main part of the deformation. In contrast, an increased amount of the ordered β_o-phase at room temperature (RT) can lead to embrittlement of the alloy. Thus, this phase has to be avoided in the microstructure at RT by a well-adjusted heat treatment. Another disadvantage of the β_o-phase is the possibility of the appearance of decomposition products, e.g. the brittle ω_o-Ti_4Al_3Nb- phase with a $B8_2$-structure [23].

2.2.2 Alloying Elements

To get an insight into the alloy design of the TNM alloy, the main alloying elements will be discussed in terms of their effect on microstructure and properties.

2.2.2.1 Aluminum

Aluminum is the main alloying element and its range is from 42 – 49 at.% [5]. In combination with Titanium, it forms intermetallic phases as already discussed. As shown in Figure 3, Al is an α stabilizing alloying element. Furthermore, with varying the Al-concentration, the solidification path can be changed from β-solidifying to a peritectic solidification.

2.2.2.2 Niobium and Molybdenum

Beside Aluminum, Niobium and Molybdenum are the major alloying elements of the TNM alloy. Nb as well as Mo are β-stabilizing elements by extending the β-phase field region to higher Al-contents. It is noteworthy that Mo is approximately 4 times stronger than Nb. By strongly stabilizing the disordered β-phase at elevated temperatures, Mo makes, already in modest amounts, near conventional hot-working of TiAl feasible [24]. Furthermore, these elements increase the melting and eutectoid temperature and set the γ-solvus temperature, which is of advantage in terms of grain refinement to the Al-rich side. Due to the raising of activation energy of diffusion by adding Nb and Mo to both γ-TiAl and α_2-Ti_3Al, thermally activated dislocation climb is suppressed, and high temperature strength and creep resistance are increased significantly. A further influence of Nb is the reduction of stacking fault energy and therefore the increase in RT ductility, as twinning is enabled more likely [9].

2.2.2.3 Boron

Already small additions of Boron can lead to a strong grain refinement due to their thermally stable borides, mainly titanium monoborides TiB. For solidification as well as for the $\beta \rightarrow \alpha$ phase transformation, these borides act as heterogenous nucleation sites [24]. Already an addition of 0.1 at.% causes a recognizable grain refinement. As stated by D. Hu [21], when B is added to the TiAl-system, nearly all 12 α-variants can nucleate in the course of the ($\beta \rightarrow \alpha$)-phase transformation. Thus, grain refinement is enhanced.

2.2.2.4 Carbon and Silicon

The further advancement of TNM gives rise to the micro-alloying with C and Si. This leads to the development of the so-called TNM^+-alloys.

Basically, C is a strong α_2-phase-stabilizer. Depending on the alloy composition, interstitial Carbon acts as solid solution hardening element or as a strong carbide formation element. For solid solution hardening, C is mainly located at $T1_6$ octahedral sites, which exist predominantly within the α_2-phase. Therefore, the α_2-phase has the highest solubility for interstitials. By alloying especially transition metal, such as Nb, interstitial cavities are formed which result in enhancing the solubility limit in the γ-phase. In contrast, within the β_o-phase no favored sites

present in the stochiometric B2 structure can be formed by alloying, resulting in a very limited solubility of C [24]. If the C solubility is exceeded, C acts as precipitation hardening element, which forms cubic perovskite (p-type) Ti_3AlC carbides and hexagonal (h-type) Ti_2AlC carbides. These precipitations impede the mobility of dislocations [9]. Furthermore, Si has a significant impact on the microstructural stability. By micro-alloying, the dislocation mobility is lowered due to solute-drag effects [9], resulting in an increased operating temperature.

The highest solubility of Silicon can be observed in the α_2-phase, whereas the solubility in the γ- and β_o-phase is limited [25]. Comparable to C, Si tends to be in solid solution or precipitates as ζ-Ti_5Si_3 silicides with a $D8_8$-structure. As stated by Klein et al. [24], in TNM^+-alloys a substantial α_2-phase fraction dissolves the alloyed Si substitutionally and therefore solid solution hardening is the main hardening effect. For other TiAl alloy systems, the addition of Si leads to ζ-precipitations, which form mainly at lamellar interfaces and decrease the interfacial as well as the dislocation mobility.

2.3 Additive Manufacturing

Compared to subtractive processing routes, Additive Manufacturing (AM) builds up components layer-by-layer [26]. Therefore, shapeless materials, like powders, wires or liquids can be converted into a dense component by supplying energy, e.g. light, laser or electron beam. Within the last years, a variety of different CAD based techniques were developed and are objects of research. Within this work, Selective Laser Melting (SLM) was used and therefore this process will be described in the following.

2.3.1 Selective Laser Melting

Selective Laser Melting (SLM) is a powder bed-based process, where layers of powder are fully melted by a laser to form dense structures (see Figure 9) [27].

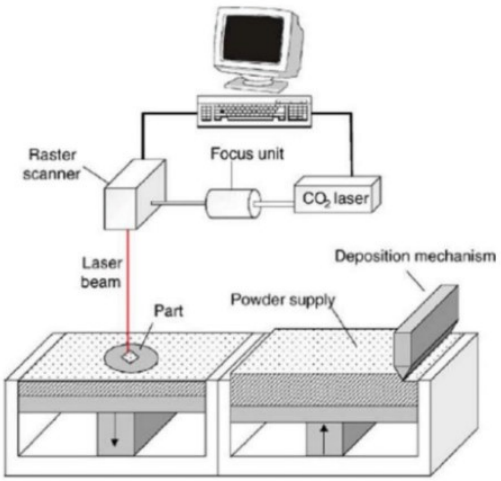

Figure 9: Schematic illustration of the SLM machine; reprinted from Ref. [27], Copyright (2015), with permission from Springer Verlag Berlin Heidelberg.

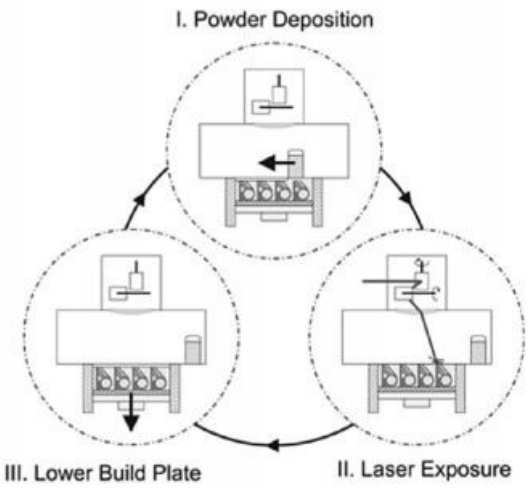

Figure 10: Schematic illustration of the three main process steps of SLM; reprinted from Ref. [26], Copyright (2016), with permission from Elsevier.

Figure 10 gives an overview of the basic steps of the SLM building process, which can be described as follows:

1. Powder is deposited from a powder supply next to the work area onto the build platform. This powder layers have usually a thickness of 20 – 1000 µm. [26]
2. The laser with a power P_L in between 20 W and 1 kW [26] is applied to the work area to locally melt the powder. The generated volume energy E_V can be calculated with

$$E_V = \frac{P_L}{v_s \cdot h_s \cdot D_s}, \tag{2.2}$$

   where P_L is the power of the laser, v_s the scan speed of the laser, h_s the hatch distance and D_s the layer thickness.
3. After this exposure, the build plate is lowered by the amount of D_s and powder is deposited anew.

2.3.2 Process Parameters

In order to characterize the microstructure of SLM-built parts, the “unique” parameters of this manufacturing process have to be taken into account. The aim of the SLM-process is to produce fully dense components, typically > 99.5%, compared to the Selective Laser Sintering (SLS). Due to the continuous improvement of the laser, melting of powder is feasible [27]. Therefore, the SLM process is carried out under inert gas atmosphere, like Nitrogen or Argon, to prevent the powder and the melt, respectively, so that the residual Oxygen content is less than 0.1%. Especially materials, which tend to pick up Oxygen, like TiAl, or passivate by building up a stabile oxide layer on the surface (Ti, Al), are very sensitive to O_2-impurities of the inert gas atmosphere as this not only influence the powder flow behavior but also impact the melt pool under changing the bulk material composition. To minimize this cause of error, on a first step the whole building space will be thoroughly purged with inert gas or placed under vacuum. During processing, a homogenous stream of inert gas, mostly Ar, protects the build platform to prevent melt pool oxidation. Nevertheless, a lack of fusion between the single scan lines can occur, leading to a degradation of the part’s mechanical properties. Additionally, the inert gas provides a gas flow, so that secondary products of the process, like weld fume and weld spatter, are removed from the processing zone [26].

The component is built up layer-by-layer, comparable to weld cladding. As seen in Figure 11, the material itself can be considered as stacked welding beads and therefore the process parameters have to be improved to avoid lack of fusion, pores or impurities. As a result of this process, usually SLM parts have a pronounced anisotropy in the mechanical properties. There are two main directions of manufacture, as shown in Figure 12. Applied to a complex geometry, directions other than z and xy, like 45° or 60°, may occur as well.

As shown in Figure 12, direction of manufacture z shows larger effective cross sections of the remaining pores and oxide layers resulting from the process. Therefore, the mechanical properties of this direction are generally inferior compared to direction of manufacture xy.

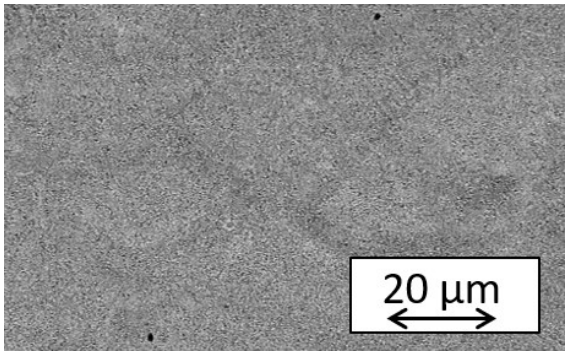

Figure 11: Typical microstructure of a SLM-produced TNM specimen (Printjob 1, specimen 1.4); cross section perpendicular to the welding beads.

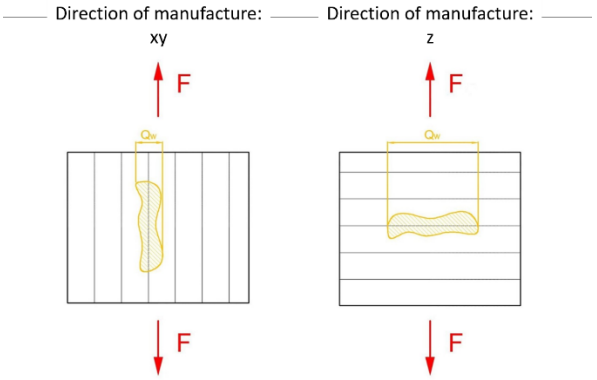

Figure 12: Schematic drawing of the direction of manufacture and the effective cross-section of pores in relation to an applied force.

Furthermore, the SLM process shows very unique and complex thermal conditions due to the very small melt pool size and high scan speed. As powder has to be molten, high laser energy has to be applied. Due to the very local and high energy input, high temperatures and high temperature gradients traceable to the low chamber and baseplate temperature are obtained. As stated by Spierings et al. [28], wherein simulations for a SLM processed Al-Mg-Sc alloy was conducted to fully understand the solidification and precipitation reactions from the melt. The SLM-processing temperature of the melt-pool can be reached for this 5xxx Aluminum alloy with up to 2520°C, the cooling rates of up to $1.5 \cdot 10^6$ K/s and temperature gradients as high as $20 \cdot 10^6$ K/m. Depending on material properties, like thermal conductivity or specific heat capacity, as well as on processing conditions, like hatch distance or laser energy, these values may vary for different materials. Nevertheless, this simulation can be seen as a reference for the general SLM process. To rate the process for TNM, the thermal properties of the TNM-alloy can be taken from the literature Gaitzenauer et al. [29]. By adapting this simulation to TNM based alloys and crosslinking the output to the chemical and microstructural properties, this can be considered as a profound basis for further research. However, despite the difference in the material used, the fundamentals of the simulation will be discussed in chapter 4.5 and applied to the TNM alloy.

In terms of lightweight design, SLM has an outstanding potential. The process itself allows bionic inspired and weight saving structures to be built, as any other conventional manufacturing process can. Nevertheless, SLM parts are limited in terms of size by the build volume of the SLM machine.

2.3.3 Powder Requirement

The starting powder represents a critical parameter for the SLM processability and has a significant influence on the quality of the SLM parts. The basic powder requirements are described by Herzog et al. [26]. To achieve a uniform powder layer across the whole building space, AM powders need good flow properties. Furthermore, to avoid a disproportionably large number of holes, a good bulk density is required by choosing a well-adapted particle size

distribution and spherical shape of the powder. Therefore, a tradeoff between very fine particles, which tend to agglomerate, and coarse particles, which limit the bulk density, has to be found. To further enhance the density of the powder layers, a bimodal size distribution can be used. In the current work, a particle size of about 30 µm was chosen. Moreover, the form of the powder particles can also contribute positively towards the processability. Hence, spherical and non-hollow particles are the aim for powder fabrication.

To obtain metallic powders within the size and shape specifications, as well as in terms of chemical purity, the EIGA (Electrode Induction Melting Gas Atomization) process is most commonly used. For this process, rotating ingot feedstock material is inductively melted, and the melt is atomized by a high-velocity inert gas stream [30].

2.3.4 Challenges faced with SLM of TNM Alloy

The challenges discussed, lead to difficulties in the processing of TNM-alloys by SLM. Firstly, the process parameters have to be evaluated based on a parameter study to obtain a stable melt pool. Investigations were already conducted by various authors [17,31] to avoid instable melt pool or melt tracks with cracks.

As the TNM alloy is very sensitive to Oxygen pick up, embrittlement is a consequence of impurities in the inert gas atmosphere [32]. Therefore, a very pure Ar atmosphere has to be established to minimize the risk of embrittlement during the SLM process. Furthermore, the oxygen content of the powder has to be regulated and minimized to keep impurities at a low level. Due to the large surface of the powder particles, this poses a challenge for future developments. Beside the oxygen-embrittlement, oxide layers can lead to a lack of fusion and pores. To minimize the number of pores, HIP was established as a state-of-the-art treatment of SLM-built parts and is inalienable for critical parts, especially in aerospace application, see refs. [16,31].

As TNM alloys have a reduced ductility and fracture toughness compared to other materials [33], thermally induced residual stresses during the rapid solidification and due to the temperature gradients can cause crack formation and growth. Thereby, it is essential to preheat the installation space and the work platform to avoid thermal stresses. Thus, a further development in terms of machine improvement has to be conducted to maintain this temperature during the whole building process. Furthermore, considering the induced stresses between the baseplate and the SLM-specimen, the baseplate has to be ideally of the same material. This will minimize thermal stresses, warping of the baseplate and inducing of cracks and pores in the specimen.

Due to the high temperature obtained by the laser, a loss of volatile alloying elements, like Al, with a high vapor pressure and a low evaporation temperature cannot be avoided. Thus, the chemical composition of the starting powder has to be adjusted to the SLM process to achieve the required chemical composition in the SLM-built component. Especially for Electron Beam Melting (EBM), the loss of Al was reported by various authors [31,34,35] but was also observed in the present work, as described in chapter 4.1.

3 Experimental Methods

3.1 Powder Production

Both, the pre-alloyed electrode feedstock material for the gas atomization and the powder were fabricated and dispatched with an enclosed chemical and powder fraction analysis by GfE Metalle und Materialien GmbH in Nuremberg, Germany (see chapter 4.1 and 4.2). For the atomization, the crucible free EIGA process was used. For this process, a rod-shaped ingot material of the TNM alloy is continuously melted inside of an induction coil and the melt is atomized by an inert gas, preferably Argon. The melt flow rate is dependent on the induction power and the forward speed of the rod leading to very fine powders. However, segregations of the ingot material are transferred to the powder particles [36,37]. To compensate a possible occurring aluminum loss during the manufacturing, the Al content was purposely set to the higher limits of the TNM specification (45 at.% Al). Further chemical analysis of the stored and used powder was also done by GfE Metalle und Materialien in Nuremberg, Germany. A particle size distribution analysis of the stored and used powder was conducted by the Chair of Process Technology and Industrial Environmental Protection using a Sympatec Helos Vario KF Magic device at the Montanuniversität Leoben, Austria.

3.2 Selective Laser Melting

The SLM samples were fabricated by the Institute for Mechatronics, University of Innsbruck, Austria, using a self-modified AconityLAB® machine. For the purpose of this thesis, a high temperature heating unit was integrated into the installation space. This heating unit consists of an induction coil underneath the baseplate. Therefore, preheat temperatures of the baseplate of up to 1200°C can be reached. The installation space has a diameter of 170 mm and a height of 200 mm. The remaining oxygen content in the atmosphere is specified as less than 10 vol. ppm. For all printjobs, a cooling rate of 1 K/min and inert gas purging after the printing was adjusted. To detach the specimens from the baseplate, wire cutting at Haumberger Fertigungstechnik GmbH in Judenau, Austria, was conducted.

3.2.1 Parameter Studies (Printjob 1, 2 and 3)

For the pretests, the laser power P_L, scan speed v_s, island size s_i and preheat temperature T were altered to investigate their influence onto density and microstructure. For all printjobs, the hatch distance was constant with $h_s = 100\ \mu m$ and the powder layer thickness was $D_s = 30\ \mu m$. An overview of the process parameters is given in Table 1. In case of printjob 1, the aborted specimens with the label 0.1, 0.2 and 2.2 are notable (see Figure 13). The first two aborted specimens were used for process parameter iteration to determine the stable process window. For specimen 2.2 irregularities appeared and therefore abortion was inevitable. Due to a small change in the setup geometry of Printjob 3, specimen 2.5 was not build.

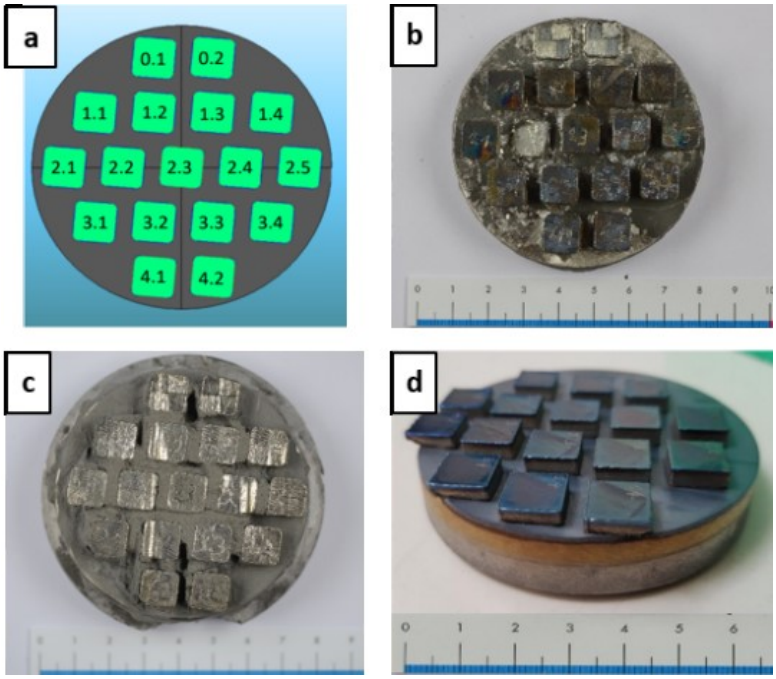

Figure 13: (a) Setup geometry and nomenclature of the SLM specimens and (b) images of printjob 1, (c) printjob 2 and (d) printjob 3.

Table 1: Process parameter iteration of laser energy P_L, scan speed v_s, island size s_i, and preheat temperature T for printjob 1, 2 and 3.

Nr	Printjob 1				Printjob 2				Printjob 3			
	P_L [W]	v_s [mm/s]	s_i [mm]	T [°C]	P_L [W]	v_s [mm/s]	s_i [mm]	T [°C]	P_L [W]	v_s [mm/s]	s_i [mm]	T [°C]
0.1	80	450	5	900	80	450	5	1200	120	666	10	900
0.2	80	450	5	900	80	450	5	1200	140	777	10	900
1.1	80	450	10	900	80	450	10	1200	160	888	10	900
1.2	80	300	10	900	80	300	10	1200	120	747	10	900
1.3	80	450	10	900	80	450	10	1200	140	848	10	900
1.4	80	450	10	900	80	450	10	1200	160	969	10	900
2.1	120	675	10	900	120	675	10	1200	120	800	10	900
2.2	160	900	10	900	160	900	10	1200	140	933	10	900
2.3	60	300	10	900	60	300	10	1200	160	1066	10	900
2.4	80	450	5	900	80	450	5	1200	120	666	10	900
2.5	80	450	5	900	80	450	5	1200	-	-	-	-
3.1	60	300	5	900	60	300	5	1200	120	666	10	900
3.2	120	675	5	900	120	675	5	1200	120	666	10	900
3.3	80	450	2.5	900	80	450	2.5	1200	120	666	10	900
3.4	60	300	2.5	900	60	300	2.5	1200	120	666	10	900
4.1	120	675	2.5	900	120	675	2.5	1200	140	777	10	900
4.2	100	550	2.5	900	100	550	2.5	1200	160	888	10	900

For all specimens, a rotation of 67° between each single layer was used to have a random distribution of grain growth according to the thermal field. Zhou et al. [38] proved, that equally orientated layers are furthest from each other when the layers are rotated 67° to each other. For the process parameter studies, samples with a base of 10 x 10 mm² were built and arranged as seen in Figure 13. The height of the specimens varied with the printjob, to reduce printing times. For specimen 2.4, 3.1, 3.2, and 3.3 of printjob 3, all above outlined parameters were constant but the laser beam focus diameter was varied from setting 1 to 4. As substrate plate for the first three printjobs, a titanium plate was used. Compared to the first two printjobs, further enhancements were made for the third printjob. On the one hand, the applied powder layer was leveled a second time by the scraper and on the other hand, the delay times of the laser system were calibrated to take over the overlap at the island borders and avoid pores at the island interfaces. Both enhancements were made to reduce the formation of pores.

3.2.2 Printjob 4

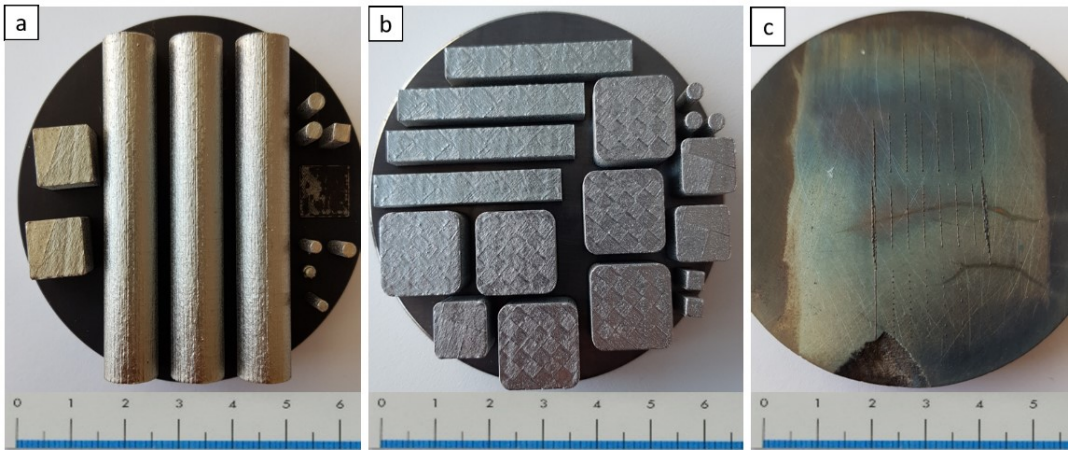

Figure 14: Printjob 4 with (a) creep test, cubic and cylindrical specimens, (b) 3-point bending specimens, cubic and cylindrical specimens and (c) single line experiments.

For printjob 4, the parameter settings are shown in Table 2. An overview of the baseplates with the specimens is given in Figure 14. As for all other printjobs, the hatch distance was $h_s = 100\ \mu m$ and the layer distance was $D_s = 30\ \mu m$. Within this printjob, creep test specimens, 3-point bending specimens, cubic specimens to investigate the quality of heat treatment processes and cylindrical specimens for analysis in the X-ray microscope Zeiss Versa were built. Technical difficulties in terms of warping due to a discrepancy in the thermal expansion coefficients of the Titanium baseplate and the TNM specimen occurred. Therefore, a TNM baseplate was used for printjob 4, to overcome those differences in the thermal properties. In addition, further improvements were made to the SLM machine in response to an increased concentration of Oxygen and further impurities like Fe, Cr and Mo (see chapter 4.1). Seals at the bottom of the heating unit were exchanged to avoid oxygen pick up. Due to detected impurities in the course of the chemical analysis, reinforcements of the powder containment, which are difficult to clean and are prone to deposition of powder, were removed to avoid unintended cross-contaminations with prior fabricated powders.

3.2.3 Single Line Experiment

The Single Line (SL) Experiment was conducted with the parameters of Printjob 4, as stated in Table 2. An overview of the baseplate with the single line experiments is given in Figure 14c. Therefore, a single powder layer was applied, and a single line was melted. This experiment was executed to analyze the microstructural evolution and melt pool expansion as well as the track stability, surface morphology and microsegregations for a single line. For sake of avoidance of contaminations, a TNM material of previous investigations by Schwaighofer et al. [20] was used as baseplate.

Table 2: Parameter settings of laser energy P_L, scan speed v_s, island size s_i, and preheat temperature T for printjob 4.

	Amount	Printjob 4			
		P_L [W]	v_s [mm/s]	s_i [mm]	T [°C]
Creep specimen (Ø10 mm² x 60 mm)	3	140	848	5	900
Bending specimen (6 x 6 x 40 mm³)	4	140	848	5	900
Cubes (10 x 10 x 10 mm³)	5	140	848	5	900
Cubes (15 x 15 x 10 mm³)	6	140	848	2.5	900
Cylinders (Ø 3 mm² x 10 mm)	9	140	848	5	900
Towers (3 x 3 x 10 mm³)	3	140	848	5	900

3.3 Microstructure Characterization

The preparation of the as-built SLM specimens for the Light Optical Microscopy (LOM) or the Scanning Electron Microscopy (SEM) was performed on a Tegramin-30 and a LectroPol by Struers GmbH, Germany. Therefore, specimens were grinded and electrolytically polished. The parameters for the electropolishing are shown in Table 3.

Table 3: Parameters for electropolishing.

Electrolyte	A3 [39] 55 – 57 % Methanol 25 – 45 % 2-Butoxy-ethanol
Voltage	36 V
Flow rate	8
Duration	24 s
Temperature	18 °C

3.3.1 Light Optical Microscopy

The LOM analysis of the metallographically prepared sections were carried out on an Axio Imager.M2 with an AxioCam ICc5 by Karl Zeiss AG, Germany. The image analysis software Stream Motion 1.9.3 by Olympus Soft Imaging Solutions GmbH, Germany, was used to evaluate the as-SLM specimens in terms of porosity and density and the powder in terms of sphericity. Therefore, a representative area of 5 x 5 mm² from the center of the LOM images from each specimen was taken for this analysis (see red area in Figure 15). This overview images should avoid any influence of the dense surface layers or cracks of the samples of the third print job, which were introduced due to a wrong cutting.

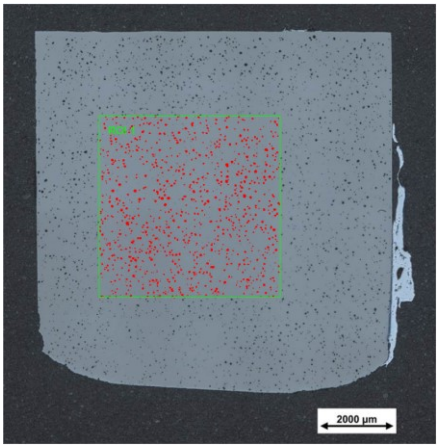

Figure 15: Lightoptical image of the specimen 1.2 of printjob 1 with the region of interest (ROI), where the porosity analysis was conducted; redly marked areas define pores.

Next to the phase analysis, various geometrical factors were evaluated: form factor, sphericity and the equivalent diameter. The form factor gives the relation between the measured area of the object compared to the area of a circumference-equal circle. Therefore, a perfect circle has a form factor of 1 and with more complex forms of the powder particle, the value for the form factor decreases. The sphericity reports the squared quotient of width and length of an object and so a perfect spherical object has a sphericity of 1. The equivalent diameter gives the diameter of a circle with the equal area. For further information about geometrical factors, the reader is referred to Wimler et al. [10] and Schatt et al. [40].

3.3.2 Scanning Electron Microscopy

For the microstructural analysis, a Zeiss Evo® 50 Scanning Electron Microscope with an acceleration voltage of 15 kV was used. For further investigations in terms of Electron Backscatter Diffraction (EBSD) measurements a FEI Versa 3D™ DualBeam™ Focused Ion Beam device was used.

3.4 Differential Scanning Calorimetry

In order to determine the temperatures of the phase transitions, $T_{\gamma,solv}$ and T_{β} to perform a well-adjusted heat treatment, differential scanning calorimetry (DSC) was applied. The DSC

measurements were conducted on a LABSYS evo STA from Setaram Instrumentation SAS, France. This method is based on the change of the heat flow rate of a specimen while phase transitions. Therefore, a crucible with the sample and a reference crucible are placed into the device and the electrical voltage of both samples is measured, while heating up to a defined temperature under Argon inert gas atmosphere. If the heating is disturbed due to a phase transition, a differential signal between the specimen and the reference crucible is generated [41]. The DSC equipment takes advantage of this measurable exo- (negative heatflow) or endothermal (positive heatflow) processes during different heating rates of the specimen (see Figure 16). Three different heating rates were applied: 10, 15 and 20 K/min. As these heating rates do not meet the thermodynamic equilibrium, a linear extrapolation to the phase transition temperature for a theoretical heating rate of 0 K/s has to be calculated. For the measurements, specimen 1.3 of the third printjob and two specimens of the fourth printjob were used to excise samples of 50 ± 2 mg. To ensure a sufficient heat transfer, the surface was grinded with SiC abrasive papers up to grit #4000. Afterwards, the specimen was placed into an Al_2O_3 crucible with the grinded surface downwards. For further information, the reader is referred to Höhne et al. [41]. The data were processed with Calisto v1.066 by Setaram Instruments SAS, France.

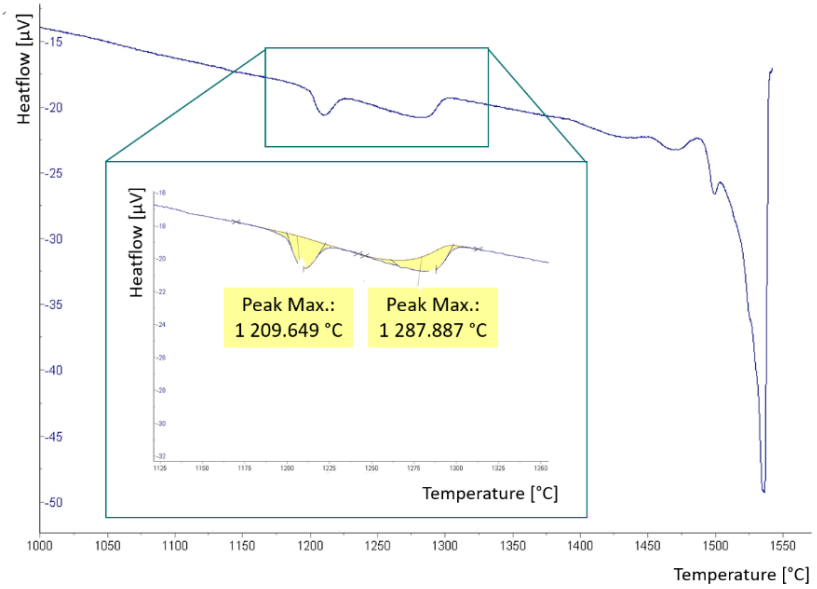

Figure 16: Representative Differential Scanning Calorimetry (DSC) measurement of specimen 1.3 of printjob 3 with a heating rate of 15 K/min; the Insert shows the analysis of the peaks in the course of the heat flow changes with the respective peak maxima for the eutectoid (1209.649°C) and the γ-solvus temperature (1287.887°C).

3.5 Heat Treatments

To obtain a microstructure with balanced mechanical properties, a heat treatment (HT) has to be applied. Two-stage heat treatments similar to Schwaighofer et al. [20] were conducted using a RHF 1600 furnace from Carbolite Gero GmbH & Co. KG, Germany. Therefore, two different microstructures for the specimens of the parameter study were adjusted: a nearly lamellar gamma (NLγ) and a fully lamellar (FL) microstructure. The temperature profile of the different HTs can be seen in Figure 17.

3.5.1 Heat Treatment Study of Printjob 1 to 3

To adjust a NLγ and a FL microstructure, different types of heat treatments were performed. This HTs are displayed in Figure 17. Firstly, a heat treatment according to ref. [20] was conducted. The first stage was held for 1h at 1220°C with subsequent air cooling (AC). The second HT was conducted as an improved heat treatment to the reference treatment based on the DSC measurement. As a result of this measurement, the T_{eut} and the $T_{\gamma,solv}$ were slightly higher than reported in [20]. For this reason, the annealing of HT2 was held for 0.5h at 1250°C with subsequent AC. HT3 was conducted to evaluate $T_{\gamma,solv}$ by means of ensuring microstructure analysis and therefore the specimen was held for 0.5h at 1280°C with subsequent AC. With HT4, a FL microstructure was obtained by an annealing temperature above $T_{\gamma,solv}$ for 0.5h at 1300°C with subsequent AC. HT5 was performed with a preceding solution annealing to fully dissolve the existing lamellas. This heat treatment was held for 0.5h at 1300°C and afterwards furnace cooled (FC) to 1250°C and held for 0.5h with subsequent AC.

Afterwards, all specimens were tempered for 6h at 850°C, followed by FC.

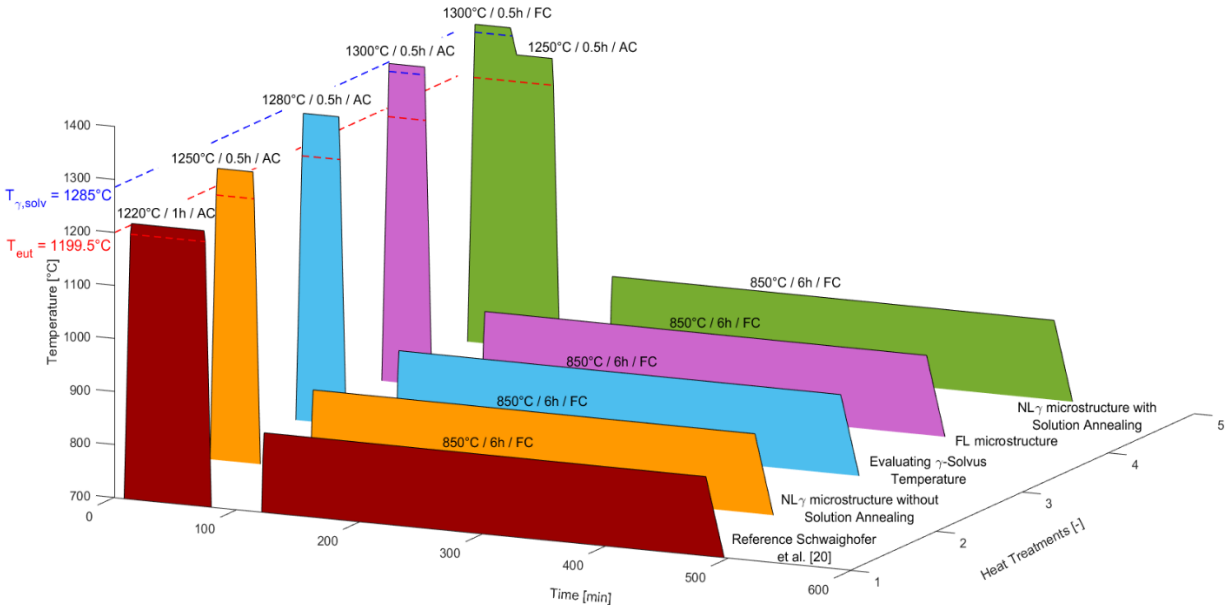

Figure 17: Overview of the conducted heat treatments starting from an as-SLM and HIPed condition, whereas HT1 was conducted acc. to ref. [20] with an annealing step of 1220°C / 1h / AC; HT2 was an improved heat treatment based on the DSC measurement to adjust a NLγ microstructure with 1250°C / 0.5h / AC; HT3 was performed at 1280°C / 0.5h / AC to evaluate the γ-solvus temperature measured by differential scanning calorimetry; HT4 was performed to obtain a FL microstructure at 1300°C / 0.5h / AC; HT5 was a further improvement of HT2 with a solution annealing step at 1300°C / 0.5h / FC prior to the annealing step at 1250°C / 0.5h / AC. All subsequent aging steps were conducted at 850°C / 6h / FC.

3.5.2 Heat Treatment for Mechanical Testing Specimen

Due to the improved creep properties of a FL microstructure and for sake of comparability, all SLM mechanical test specimens were heat treated according to HT4 (see Figure 17). Afterwards the specimens were tempered for 6h at 850°C with a subsequent FC.

3.6 X-Ray Diffraction

In order to obtain quantitative information about the phase distribution of the as-SLM compared to the heat-treated specimens, X-Ray Diffraction (XRD) measurements on the D8 Advance from Bruker AXS Advanced X-ray Solutions GmbH, Germany were conducted, using Cu K-α radiation with an energy of $8.04\ \mathrm{keV}$. This energy corresponds to a wavelength of $1.54\ \text{Å}$. Due to the polycrystalline structure of the material, the specimen has to be rotated during the measurement. In contrary, the powder samples do not have to be rotated. The analysis was conducted by means of a Rietveld refinement on TOPAS. Therefore, a given pattern of the TNM alloy with the peaks corresponding to the respective crystallographic phases were taken as an initial template. By iteration, the measured pattern was fitted to this initial model, whereas the variables correlate to the amount of the phase fraction.

3.7 Chemical Analysis

The chemical analysis of the as-SLM specimens, as well as of the powder was delivered by GfE Metalle und Materialien GmbH, Germany. This analysis was performed to quantify the loss of different alloying elements in the course of AM, in this case mainly Al. Therefore, different bulk specimens (e.g. printjob 1, specimen 2.5; printjob 2, specimen 2.4 and various specimen of printjob 3 one specimen of printjob 4) were analyzed to see an influence of the processing parameters onto the mean alloying composition, compared to the initial powder composition. Powder samples were also analyzed to evaluate the ability of storage of powder under atmospheric conditions and the recyclability of powder which was already applied in the installation space and therefore has been exposed to moderate temperatures. Furthermore, locally chemical differences and microsegregations of the bulk material due to the manufacturing process were analysed by microprobe on the device JXA 8200 from JEOL GmbH, Germany at the Department of Applied Geological Science and Geophysics, Chair for Resource Mineralogy at the Montanuniversität Leoben, Austria. Therefore, an as-built SLM specimen, an as-HIPed specimen and a specimen with a single line experiment were analyzed.

3.8 Mechanical Testing

Prior to mechanical testing, all specimens of the fourth printjob were hot isostatically pressed (HIP), heat treated according to HT4 (see chapter 3.5), and surface processed at the Institute of Physics at the Montanuniversität Leoben, Austria. The HIP process was conducted by voestalpine Böhler Edelstahl GmbH & Co KG in Kapfenberg, Austria. The parameters of this treatment are strictly confidential but correspond to industrial HIP-parameters of this material. For the heat treatment, the previously stated temperatures and times were used to obtain specimens with a FL microstructure, as this microstructure shows the optimized creep properties up to higher temperatures, as already stated in literature [5,6,9,42–44]. These tests were performed to analyze the mechanical properties and correlate them to the microstructural features. Furthermore, the data were compared to conventional manufactured TNM alloy.

3.8.1 Creep Tests

The creep tests were conducted at the Chair of Physical Metallurgy and Metallic Materials at the Montanuniversität Leoben, Austria. Therefore, testing machines of the type TC 30 from Dension Mayes Group, Great Britain, were used to execute short time creep tests. A drawing of the sample geometry according to DIN EN 10291 is given in Figure 18. Due to the limited space of the installation space of the SLM machine, the specimens were adjusted confirming to the standard to a length of 60 mm. During the tests, a temperature of 800°C and a load of 170 MPa had to be held on a constant level, while the occurring creep strain was recorded. These parameters were chosen according to Kastenhuber et al. [43,44], where conventional manufactured TNM alloys were tested. Nevertheless, due to impurities of the material, the testing procedure was adapted and the load had to be decreased (see chapter 4.6.2).

The occuring strain can be divided into an elastic contribution A_e, an elastic plastic contribution A_i and a time dependent creep contribution $A_f(t)$ [45]. According to Heine [45]and Garofalo et al. [46], three stages during a creep test can be observed: primary creep, stationary or secondary creep and ternary creep. In the primary stage, the creep rate ($d\varepsilon/dt$) is decreasing with increasing time until the beginning of the secondary creep, where the creep strain rate is on a constant level. The start of the third stage of creep is marked by an increase of the strain rate up to the failure of the specimen. The time-dependent strain ε(t) can therefore be written as:

$$\varepsilon(t) = A_e + A_i + A_f(t)\,. \tag{3.1}$$

Inserting exponential concepts for the first and third creep stage and a linear concept for the second creep stage into *(3.1)* results in:

$$\varepsilon(t) = (A_e + A_i) + K_1 \cdot \left(1 - e^{(-bt)}\right) + K_2 \cdot t + K_3 \cdot e^{\left(c \cdot t^f - 1\right)}, \tag{3.2}$$

whereas $K_1 \cdot \left(1 - e^{(-bt)}\right)$ is describing the primary, $K_2 \cdot t$ the secondary and $K_3 \cdot e^{\left(c \cdot t^f - 1\right)}$ the ternary creep stage, with t as creep time. K_1, K_2 and K_3, as well as b, c and f are constants to fit the function to the obtained data.

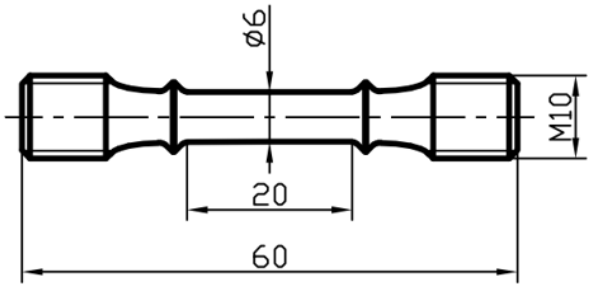

Figure 18: Geometry of the creep test specimen according to DIN EN 10291; due to the limitation of the installation space, the specimen were adjusted confirming the standards to a length of 60 mm.

For the evaluation of the creep tests, the data were processed with Matlab R2017a. The results were fitted for visualization with equation (*3.2*) and the creep strain and the creep strain rate were plotted over the time. To obtain the minimum creep strain rate, the derivative of the strain was calculated.

3.8.2 Three-Point Bending Tests

In order to compare the SLM TNM alloy with conventionally processed TNM material based on Ref. [44], a three-Point Bending Test according to DIN EN ISO 7438 was conducted. Therefore, four SLM fabricated specimens were HIPed, heat treated according to HT4 and surface processed.

For sake of comparison, two three-point bending tests on a powder metallurgical (PM) material were conducted, whereas the material was already the basis of study [44]. The analyzed chemical composition of the provided TNM material is listed in Table 4. This alloy was manufactured via a PM process and further solidified by a HIP process. Prior to testing, the specimens were heat treated according to [44] with a two-step heat treatment consisting of 1275°C for 0.5h with subsequent AC and 850°C for 6h with subsequent FC.

Table 4: Chemical composition of the powder metallurgical processed Three-Point bending test specimen as stated in Ref. [44].

	Ti [at.%]	**Al** [at.%]	**Nb** [at.%]	**Mo** [at.%]	**B** [at.%]	**C** [at.%]	**Si** [at.%]	**O** [at.%]
TNM PM	Bal.	44.09	3.93	0.94	0.098	0.037	0.036	0.181

Both batches of specimens were surface treated and tested at the Institute of Mechatronics, University of Innsbruck, Austria. Therefore, the specimens were inserted into the testing machine and a bending moment was applied with a load application of 200 N/s. Therefore, an assessment for the bending strength can be provided by [47]:

$$\sigma_b = \frac{M_b}{W} = \frac{3FL}{2bd^2}, \tag{3.3}$$

where M_b is the bending moment, W is the section modulus, F is the applied force, L is the distance between the supportings, b the sample width and d the sample height.

3.8.3 Hardness Tests

In order to compare the specimens after the heat treatment with existing literature, hardness tests according to DIN EN ISO 6507 (HV10) were conducted, using a testing machine ZWICK 3212. Therefore, a diamond pyramid with a square base area and an opening angle of 136° is pressed with a constant load into the surface of a material. Afterwards, the indentation diagonals are measured, an arithmetic average of the diagonals is calculated, and the hardness of the material is delivered by equation:

$$HV = 0.189 \cdot \frac{F}{{d_{HV}}^2}, \tag{3.4}$$

where F is the applied force and d_{HV} is the arithmetic average of the diagonals. Five hardness indentations were made in the middle of each specimen and analyzed. For further information, the reader is referred to Heine [45].

4 Results and Discussion

4.1 Chemical Analysis

The chemical composition of the different powder batches and the bulk material is listed in Table 5. Due to already existing literature [16,35,48] for processing TiAl with additive manufacturing techniques, Aluminum evaporates during the process, which leads to a decrease of the overall Al content in the chemical composition of the bulk material compared to the starting powder composition. This phenomenon is also observed for different alloying elements in AM of other material systems, as already described in refs. [28,49]. Alloying elements with the highest equilibrium vapor pressure tend to evaporate selectively during the manufacturing process. Therefore, the Al content of the powder in the present work is at the upper limit of the specification range for the TNM alloy system, to compensate any occurring loss. The difference in the Al content between the starting powder and the reference chemical composition stated in [20] is about 1.5 at.%. The chemical analysis of the as-atomized powder was conducted directly after atomizing the powder.

Table 5: Chemical compositon of the powder and SLM specimens. The reference nominal composition was taken from Schwaighofer et al. [20] for comparability; the chemical analysis was conducted at GfE Metalle und Materialien GmbH, Germany, and shows an overall value over the whole specimen.

	Ti [at.%]	**Al** [at.%]	**Nb** [at.%]	**Mo** [at.%]	**B** [at.%]	**C** [at.%]	**H** [at.%]	**N** [at.%]	**O** [at.%]
Ref. composition [20]	Bal.	43.67	4.08	1.02	0.095	0.014	0.041	0.003	0.108
Powder Batch 1 as-atomized	Bal.	45.01	3.97	0.98	0.1	-	-	-	0.28
Powder Batch 1 stored	Bal.	44.82	3.96	1.01	0.10	0.03	0.08	0.02	0.33
Powder Batch 1 heat affected by SLM	Bal.	44.87	3.96	1.04	0.10	0.03	0.04	0.01	0.28
Powder Batch 2 stored	Bal.	44.93	3.93	0.97	0.11	0.02	0.04	0.01	0.25
As-SLM Printjob 1	Bal.	42.99	3.98	0.98	0.10	0.03	0.04	0.14	0.84
As-SLM Printjob 2	Bal.	43.26	3.85	0.90	0.11	0.06	0.04	0.25	1.36
As-SLM Printjob 3	Bal.	43.80	3.93	0.97	0.11	0.30	0.12	0.05	0.61
As-SLM Printjob 4	Bal.	44.35	3.93	1.00	0.11	0.08	0.04	0.03	0.51

Noticeable is the comparable high O content of the as-atomized powder with 0.28 – 0.33 at.% (1100 – 1300 wt. ppm). This content is already above the specification of maximal 0,2 at.% (800 wt. ppm) for ingot materials [50]. It has to be stated, that already the pre-alloyed feedstock material exhibited higher O contents. Neither the storage under atmospheric conditions, nor the influence of 300°C in the overflow containment have a major influence onto the Oxygen level, respectively onto the chemical composition. The second powder batch, which was used to manufacture the fourth printjob, showed no irregularities regarding the chemical composition of the main alloying elements. The O impurities with 0.25 at.% (980 wt. ppm) are at the same level as for the powder of the first batch.

As it can be seen, the overall chemical composition of the bulk material (see Table 5) shows, that there is an Al loss after the SLM process comparable to literature for SLM [16] and EBM, where also a loss of several atomic percent was observed [35,51,52]. The examined specimens of printjob 1 and 2 were processed at line energies of 60 J/mm³ with lower laser powers. In comparison, the specimen of printjob 4 was exposed to a line energy of 55 J/mm³, but with an increased laser power. This had an impact onto the content of Aluminum, i.e. higher line energies led to more evaporation of Al. Furthermore, the comparison between the first and second printjob was done to evaluate the influence of the preheat temperature during the SLM process on the chemical composition. There is no significant change of the Al content. Noticeable is, that there is a major O pickup during the SLM process, leading to O concentrations of up to 0.84 at.% (3300 wt. ppm) for the first printjob and 1.36 at.% (5400 wt. ppm) for the second printjob. The O content increases with increasing preheating temperature. This can be related to the elevated temperatures and therefore the higher reactivity and diffusivity of Oxygen. A considerable increase of Nitrogen for the first two printjobs from 0.02 at.% (60 wt. ppm) up to 0.14 at.% (490 wt. ppm) for the first and up to 0.25 at.% (870 wt. ppm) for the second printjob suggests a leakage of the processing machine. As a result, the machine was examined for any defects, where a leakage of the preheat unit of the SLM machine was found, which was sealed for all further printjob. This results in lower O contents of 0.61 at.% (2400 wt. ppm) for the third and 0.51 at.% (2000 wt. ppm) for the fourth printjob. The content of N decreased also substantially. Nevertheless, compared to the as-atomized powder, the O content of the as-SLM part nearly doubled from 1100 wt. ppm to 2000 wt. ppm. As stated by [53–55], O impurities result in a major embrittlement of the alloy. Therefore, yield stress and work hardening coefficient is increasing, because of solid solution hardening of the α_2-phase and for higher amounts of precipitation hardening by $\alpha - Al_2O_2$ [55]. Furthermore, O is an element which is stabilizing the α/α_2-phase due to its very high solubility in this phase of up to 6 at.%, compared to 300 at. ppm for the γ-phase [8,56,57]. Hence, the microstructure will be influenced by these impurities in terms of phase composition, grain size and lamellar spacing [55,57,58]. Moreover, the solidification path of the alloy is shifted towards a peritectic solidification [59] according to the phase diagram given in Figure 7a $L + \beta \rightarrow \alpha$. At this point the reader is also referred to chapter 4.4, where the increased O level is discussed regarding to the phase transition temperatures. Furthermore, higher impurity concentrations were found due to contaminations from previous printjobs with other materials, like steels or Mo-

based alloys. For the first two printjobs, an enhanced content of Fe and Cr was detected. For Fe, an increase from 0.066 at.% (350 wt. ppm) to 0.078 at.% (600 wt. ppm) and for Cr, an increase from 0.003 at.% (20 wt. ppm) to 0.057 at.% (400 wt. ppm) took place. The third printjob had impurities of Carbon and Hydrogen, as the C content increased from 0.03 at.% (100 wt. ppm) for the first printjob up to 0.3 at.% (880 wt. ppm) and the H content from 0.04 at.% (10 wt. ppm) for the first printjob up to 0.12 at.% (30 wt. ppm). This high C content is already within the nominal composition for TNM^{+} alloys [43,44,60]. For the fourth printjob, an increase of the molybdenum content was analyzed, where the content increased from 0.9 at.% for the second printjob up to 1.0 at.% for the fourth printjob.

4.2 Powder Characterization

The powder, as the starting material for the SLM process, has a major influence on the process. The chemical composition of the powder is shown in Table 5. It is noticeable, that the powder had a very high O content of up to 0.33 at.% (1300 wt. ppm). The powder storage did not have any further influence on the chemical composition. The particle size distribution delivered with the gas-atomized powder by GfE Metalle und Materialien GmbH in Nuremberg, Germany is shown in Figure 19. For comparison, the particle size distribution of the stored powder of the first batch and the heat affected powder of the first batch with an influence of ~300°C within the installation space, as well as unused powder of the second batch is shown in Figure 20. The mean particle diameter d_{50} of the delivered powder fraction is 36 µm (see Figure 19). Compared to the initial powder, the measured powder fractions had a slightly lower mean particle diameter of 33.7 µm for not heat affected powder of the first batch, 32.8 µm for the heat affected powder of the first batch and 34.2 µm for the not heat affected powder of the second Batch (see Figure 20). The differences between the single powder fractions is negligible and not process affecting.

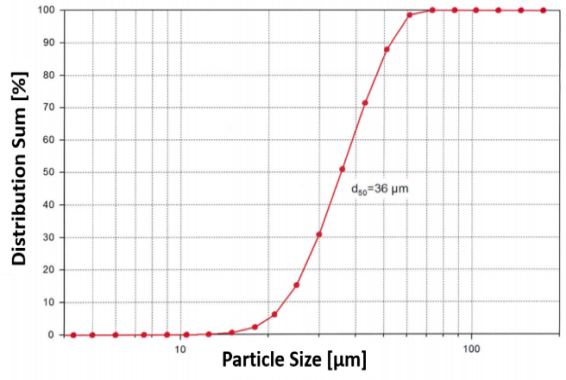

Figure 19: Particle Size Distribution of the as-atomized powder fraction conducted by Gesellschaft für Elektrometallurgie mbH. The mean particle diameter d_{50} is 36 µm.

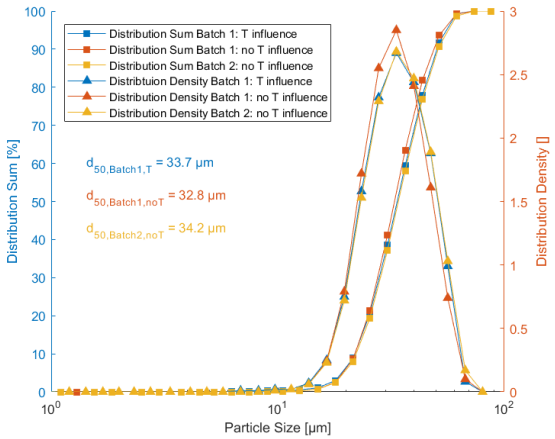

Figure 20: Particle Size Distribution of the stored powder without influence of temperature (i.e. within the overflow containment) and the used powder with influence of temperature (within the installation space) conducted by the Chair of Process Technology and Industrial Environmental Protection.

Nevertheless, the measurements confirm the results of Strondl et al. [61], whereas the powder already processed by SLM has a coarser mean particle size (compare Figure 20 $d_{50,Batch1,noT}$ and $d_{50,Batch1,T}$). The explanatory approach in [61] suggests, that smaller powders are dusted away by the stream of the inert gas atmosphere. Furthermore, the layer thickness of the individual layers is in the same order of size as the mean particle size and therefore, the bigger particles tend to be pushed in front of the scraper into the overflow compartment when applying the powder [61].

Furthermore, LOM and SEM images were taken from three different particle fractions: not heat affected powder from the overflow compartment, heat affected powder from the installation space and sintered powder from in between the cubic specimens of the second printjob. The microstructure was verified by XRD (see Annex A, Table 8). Observing the powder cross section, the shape of the particles is globular almost everywhere (see Annex B, Table 9). The form factor, the elongation and the sphericity are slightly improved for the sintered powder compared to the other powder fractions taking the mean values and the standard deviation into account. Occasionally small satellites and holes in the center of the particles can be observed in the LOM (see Figure 21, a1 – c1).

As shown in Figure 21, a2 – c2, the microstructures of the different powder fractions observed in the SEM differ according to the temperature profile they were exposed to. For the powder from the overflow containment (a2) and from the installation space (a3), a dendritic structure is clearly visible. The bright dendritic phase can be identified as the α_2-phase and the dark interdendritic phase as β_{prim}-phase. The phase fractions calculated by XRD measurements delivered consistently results to the SEM images, as can be seen in Figure 22 and in Annex A, Table 8. Furthermore, these results were also reported in literature [10,16,62]. A closer examination by Kastenhuber et al. [62] revealed two different solidification reactions occurring due to rapid solidification. When undercooling the melt into the two-phase field region of L + β, the remaining melt has higher Al contents as the first β-grains, according to liquidus line. This leads to a peritectic reaction of the remaining melt and a massive type transformation $\beta \rightarrow \alpha_m$ at further cooling. In contrary, the lower Al content in the nucleated β-grains leads to a martensitic transformation $\beta \rightarrow \alpha'$. The powder of the overflow containment was exposed to temperatures of about 300°C, but not high enough to enable diffusion-controlled phase transformations of the dendritic microstructure to a globular one. As stated in [62], at temperatures above 600°C a change in microstructure can be observed. In accordance with this investigation, the sintered powder has already seen temperatures of up to 1200°C, which results in a very fine, globular microstructure. The XRD measurement reveals a majority of γ-phase and α_2-phase, as can be observed in Figure 22. Furthermore, small amounts of β_o-phase are also present and can be seen in the SEM image as bright spots (see Figure 21, c2). To verify the phase analysis of the second powder batch, further XRD measurements were conducted. As seen in Annex A, Table 8 and Figure 22, and taking measurement inaccuracies into account, the stored powder of the second batch has similar phase fractions as the powder of the first batch.

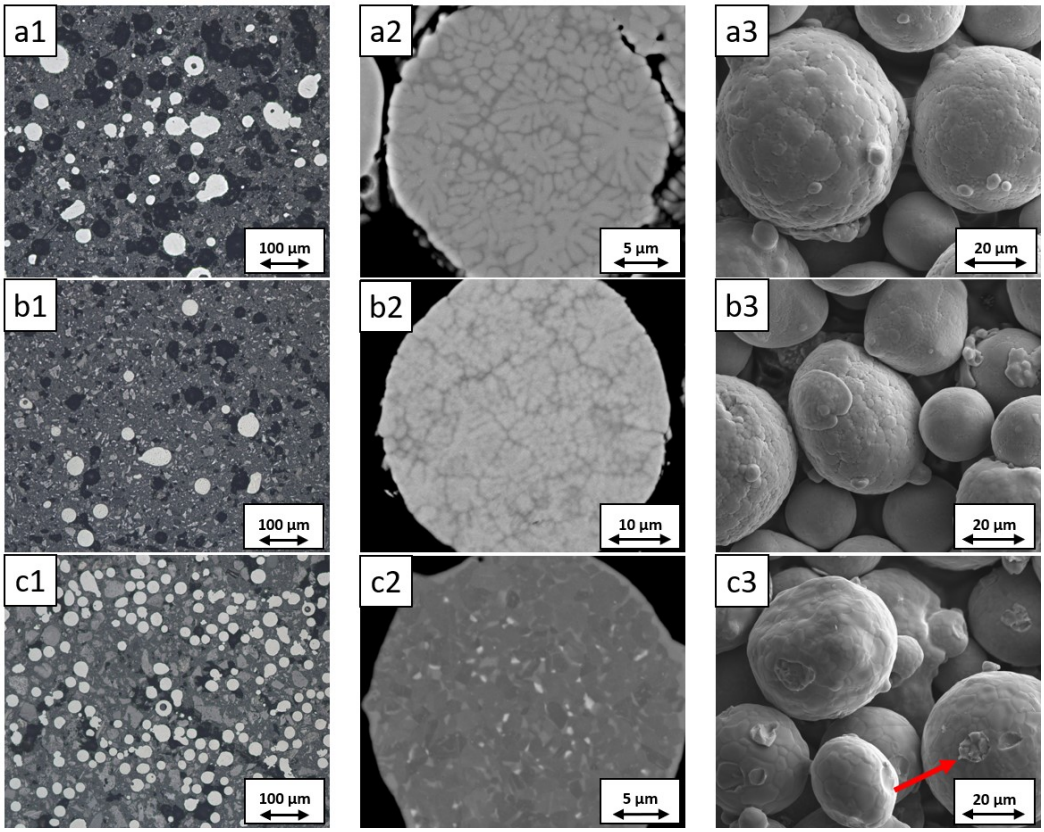

Figure 21: Powder characterization on a powder cross-section (1) under the light microscope, (2) in the SEM and (3) the powder surface morphology in the SEM of the three different powders: (a) powder without influence of temperature (overflow containment), (b) powder with influence of temperature (installation space) and (c) sintered powder from the space inbetween the cubic specimens of the second printjob (1200°C); Red arrow in (c3) indicates sintered necks.

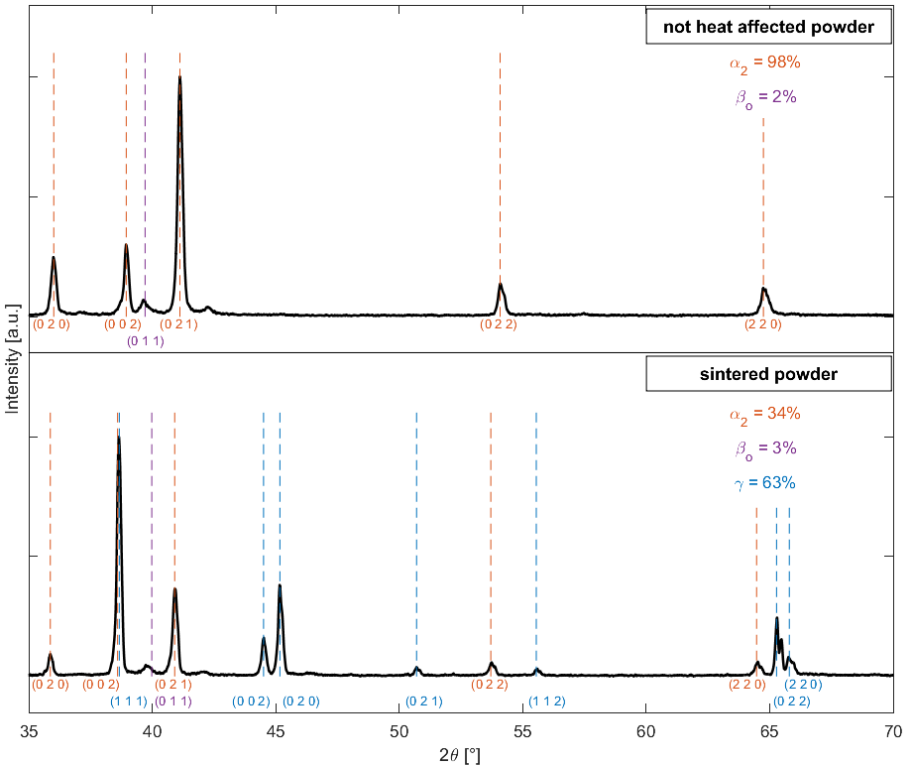

Figure 22: Comparison of the XRD measurements of not heat affected powder and sintered powder of the first batch; the phase fractions (vol.%) are summarized at each graph, details are listed in Annex A.

The surface morphology of the powder particles was observed by SEM (see Figure 21, a3 – c3). As already seen in the LOM pictures (see Figure 21, a1 – c1), satellites are observable at the surface of the powder particles. As stated by Özbilen [63], the formation of satellites occur during the flight, where finer particles collide with coarser particles. While colliding, the particles weld together due to their semiliquid surface. The amount of fine particles can be controlled by the pressure of the atomization gas, the oxygen and water vapor in the atmosphere; but also when the shape of the coarser particles is irregular and the surface texture is rough due to oxidation a major influence on the formation of satellites exists [63]. Furthermore, the microstructure and adhering satellites can be seen by means of the relief on the surface. For the sintered powder sintered necks are visible (see Figure 21, c3, red arrow). This necks between two adjoining powder particles are broken due to the mechanical extraction of the powder from the specimen.

4.3 Process Parameter Study

An overview of the parameters is given in chapter 3, Table 1 and Table 2, as well as in Figure 23. A more detailed list of the density analysis conducted with the image analysis software Stream Motion 1.9.3 by Olympus Soft Imaging Solutions GmbH, Germany, is given in Annex B, Table 10, Table 11 and Table 12 for the respective printjob.

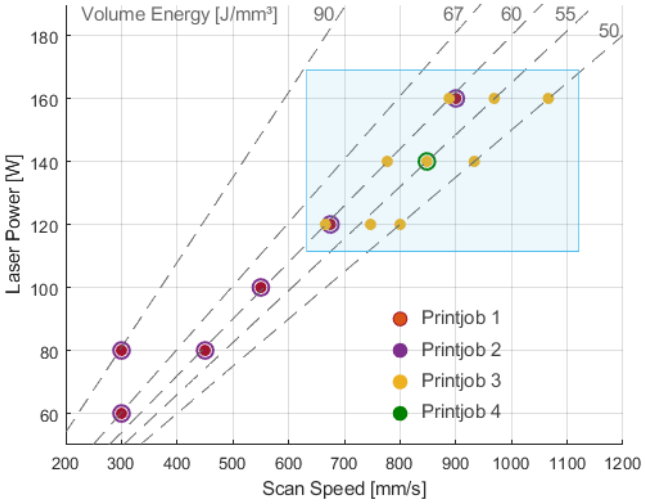

Figure 23: Depiction of the parameter study for printjob 1 - 4; highlighted area marks the parameters of samples with the highest densities; all specimens of Printjob 4 were built with the optimized set of parameters.

The parameters of printjob 1, as given in chapter 3, Table 1 and in Figure 23, were based on the parameters already investigated by Gussone et al. [16]. The results of the density analysis of the LOM images with a low magnification showed a high number of pores in the samples of the first and second printjob (see Table 10, Table 11 and Figure 24a and b). However, dense areas were found for some specimen zones, as marked in Figure 24a. These areas indicate, that process stability was not constant during the whole building process and therefore has to be improved. It can be seen, that the amount of pores and therefore the density differs with the variation of parameters for the respective samples. The critical process parameters for the

creation of pores were the applied energy in terms of laser energy and volume-based energy density, as already described in chapter 2. Dense specimens of the first and second printjob can be seen for higher laser energies (see highlighted lines in Annex B, Table 10, Table 11 and Table 12 and highlighted area in Figure 23). Therefore, the parameters for the third printjob were adapted to this result. The density analysis of the third printjob revealed nearly dense specimens (see Table 12). Furthermore, the shape of the pores in the third printjob became more spherical, as the form factor and the sphericity approached the factor 1. The equivalent diameter of printjob 1 and 2 is approximately twice the diameter of printjob 3, which indicates that both, the amount and the size of the pores became smaller. In addition, a dense marginalized layer of 500 µm is noticeable at all specimens, as it is shown representatively in Figure 25 for a selected specimen. It has to be stated, that the outer contour of the specimen differs in terms of thermal management.

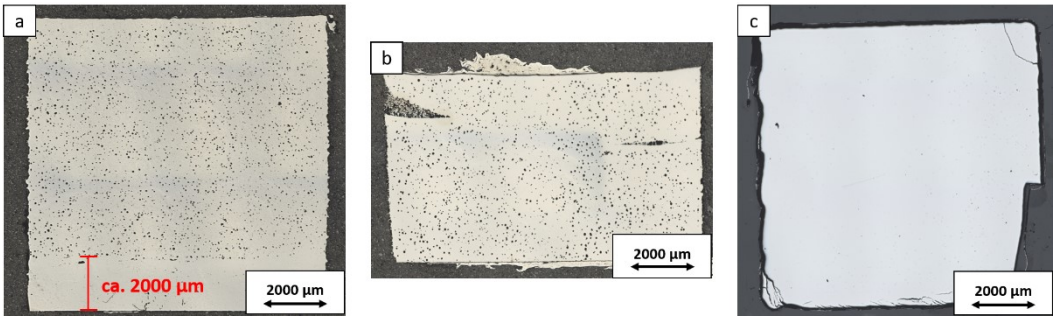

Figure 24: Comparison between the samples of different printjobs: (a) Printjob 1, specimen 2.3; (b) Printjob 2, specimen 2.3 and (c) Printjob 3, specimen 2.3. As seen in the makred area of image (a), the process stability was not given for the first two printjobs.

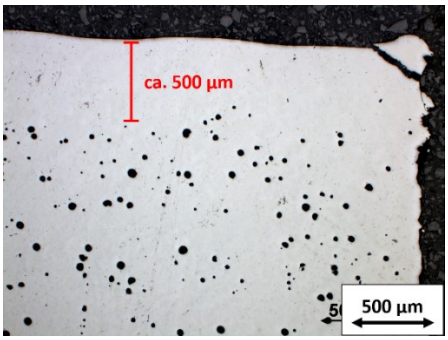

Figure 25: Representative, LOM image of the grinded and polished specimen 2.4 of printjob 1; clearly visible is a ca. 500 µm thick dense layer.

The formation of pores in the SLM process can be attributed either to a keyhole-effect as described by Zhao et al. [64] or to hydrogen induced porosity as described by Weingarten et al. [65]. Zhao et al. [64] conducted high-speed X-ray imaging of the SLM-process and showed, that basically two physical principals compete. On the one hand, the Marangoni convection results in a flow of the surface liquid from the center of the laser-heated zone with lower surface tension to surrounding regions with higher surface tension. On the other hand, the recoil pressure has strong metal evaporation around the laser beam as a consequence. This rapid moving vapor generates recoil pressure gradients and consequent melt ejaculations. For high laser energies Zhao et al. [64] stated, that the cavity depth of the melt pool is relatively large and if the laser is turned off, the molten material flows from the surrounding area into

the center of the melt pool. For the high solidification rates, the movement of the molten material at the bottom level is too slow to fill up the cavity. Furthermore, it is stated, that the molten material has 50 µs to fully close a keyhole, otherwise pores will be formed [64]. Another approach to explain the formation of pores by Hydrogen, which is mainly observed in Aluminum alloys, is given by Weingarten et al. [65]. The mandatory condition for this effect is a higher hydrogen solubility of the melt compared to the bulk material. Ma et al. [66] stated for the bulk material a hydrogen solubility of about 300 ppm for 1400 K with increasing solubility for higher temperatures. Su et al. [67] found that the hydrogen solubility in molten TiAl alloys is dependent on the hydrogen partial pressure but can increase easily to higher numbers than the solubility of the bulk material. Therefore, if the local solubility limit of the melt is reached, pores nucleate, and the growth will be stopped if the pore is captured by the solidification front. Basically, the solubility is increased for higher solidification rates. Furthermore, if the scan speed is increased, a higher partial alloying element evaporation leads to a chemical gradient. Therefore, the system is seeking to decrease this gradient and a mass flow from the bottom to the top of the melt will develop. This tendency can also be seen in chapter Annex B, Table 10, Table 11 and Table 12, as the volumetric energy density of the specimen is increasing with decreasing scan speed and increasing laser power. Weingarten et al. [65] have also shown, that a layer preparation respectively a drying step of the powder by laser or a remelting of each layer decrease hydrogen induced porosity.

To prove, that these pores are gas filled, a hot-isostatic pressing (HIP) treatment was conducted by voestalpine Böhler Edelstahl GmbH & Co KG in Kapfenberg, Austria. The parameters of this treatment are confidential but correspond to industrial production of this material. Afterwards, the specimens were annealed. As seen in Figure 26, the residual porosity of the SLM process was closed due to the HIP treatment but reopened less pronounced after annealing at elevated temperatures of 1100°C for 4h with subsequent FC. Nevertheless, there is an increase of density of more than 99.9% for the HIPed and annealed specimen, compared with the as-SLM material. Due to these results, it can be reasonably assumed, that the pores are gas filled. As pores have a major influence on mechanical properties, especially at elevated temperatures, this porosity has to be avoided already in the SLM process.

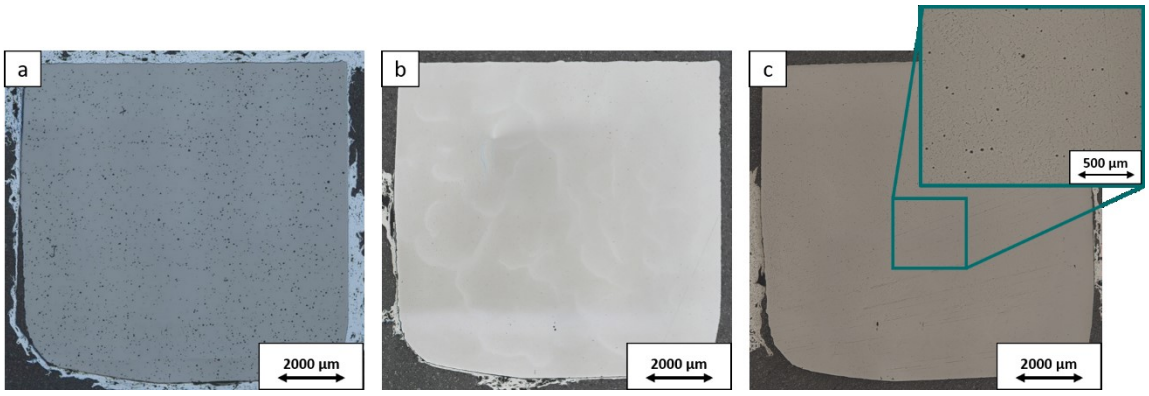

Figure 26: Overview of the results of HIP and subsequent annealing of specimen 1.4 of the first printjob: (a) a major amount of pores with an investigated density of 94.1% (see Annex B, Table 10) due to the manufacturing proces; (b) nearly fully dense sample due to the HIP process; (c) partly reopening of gas filled pores after an annealing at 1100°C for 4h with FC, the insert shows a higher magnification of the pores.

For the third printjob, three different volume energies according to equation (*2.2*) were applied: 50, 55 and 60 J/mm³. To take the porosity analysis of printjob 1 and 2 and the approach of Zhao et al. [64] and Weingarten et al. [65] into account, parameters were adapted to higher scan speeds and therefore also higher laser energies as listed in chapter 3.2. The density of selected specimens of the third printjob can be seen in chapter Annex B, Table 12. Furthermore, enhancements in terms of powder supply and laser parameter settings were done. For these samples, the powder was levelled twice by the scrapper and the delay-times on the island borders were calibrated. This enhancement avoids the formation of pores due to well-adjusted overlapping laser tracks on island borders. These improvements and iterations resulted into fully dense specimen as shown in Figure 24c and Annex B, Table 12.

4.4 Transformation Temperatures

An overview over the results of the Differential Scanning Calorimetry (DSC) measurements for the third printjob is given in Figure 27, in Annex C Figure 44 and in Table 6.

4.4.1 Parameter Study

As already stated in chapter 2, high aluminum and oxygen contents stabilize the α/α_2-phase and shift the solidification path to a peritectic reaction (see Figure 27) [59]. Therefore, in contrary to the nominal TNM alloy composition investigated in [20], a single α-phase field region occurred for the composition in this thesis. This enabled the possibility to adjust a FL microstructure by heat treating due to the necessity of annealing in the α-single phase field. For heat treatments important phase transition temperatures in the course of the parameter study are given in Table 6 and a further detailed depiction is given in Annex C, Figure 45. A comparison to Ref. [20] shows clearly higher transition temperatures. This deviation is according to the difference in the chemical composition, more precisely to the elevated oxygen content of up to 5400 wt. ppm within the alloy, compared to 420 wt. ppm in [20], as well as the increased aluminum content of up to 44.35 at.%, compared to 43.67 at.% in [20]. Furthermore, the peak between 1400°C and 1450°C of the DSC measurement (see Figure 27) was verified by heat treatment studies on specimens, which were annealed for 30 min at 1400°C and 1450°C with subsequent AC. Both specimens, show supersaturated α_2-grains, whereby a possible precipitation of fine γ-lamellae on AC could not be resolved in the SEM (Annex C, Figure 47). The specimen annealed at 1400°C did not exhibit major grain growth, whereas the specimen annealed at 1450°C showed pronounced grain growth. Due to this investigation, this peak can be considered as a measurement artifact because there is still a single α-phase region present. Furthermore, to prove the accuracy of the γ-Solvus temperature, a heat treatment for 30 min at 1280°C with subsequent AC was performed, which is according to the DSC measurement slightly below the γ-Solvus temperature. As the specimen showed a microstructure comparable to Figure 47, the γ-Solvus temperature has to be slightly decreased compared to the DSC measurement according to Table 6.

As stated in the previous chapters, Oxygen has a major influence on the solidification path and phase evolution of TNM alloys [59]. Therefore, Zollinger et al. [59] investigated four different compositions of binary TiAl based alloys adding 0.0 – 1.5 at.% O to each alloy batch. With higher oxygen contents, a change from β-solidifying towards peritectic or even with high Al and O contents towards α-solidifying is favored by the thermodynamic system. Furthermore, the stability of the α-phase is increased significantly and therefore a single α-phase field region occurs, which is in accordance with the present work.

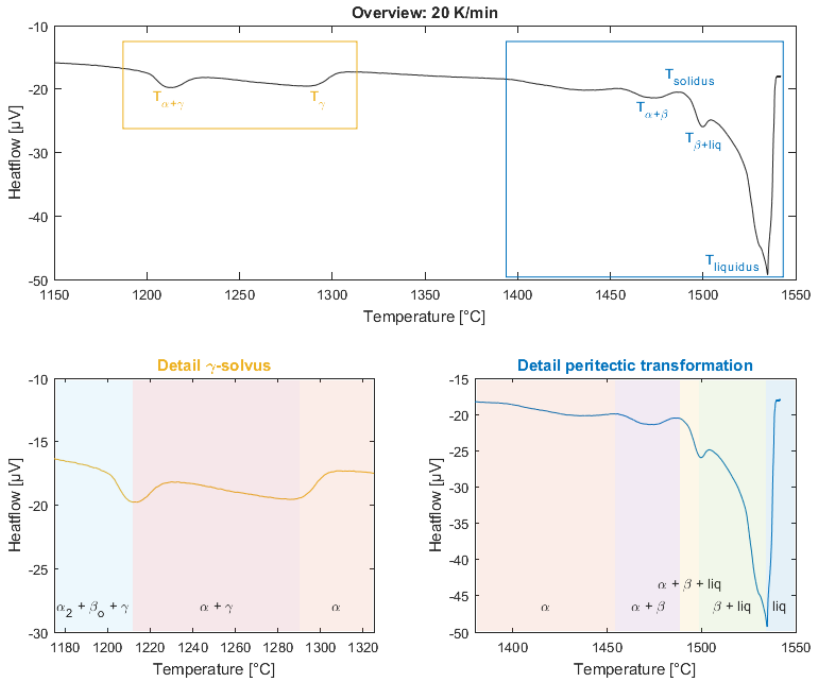

Figure 27: Phase transitions of the parameter study shown at the DSC curve with 20K/min heating rate with detailed views of the γ-solvus temperature (orange box) and the peritectic transformation (blue box); the different phase field regions are differently highlighted.

4.4.2 Printjob 4

Due to a different chemical composition of the as-built specimens of the fourth printjob, as seen in chapter 4.1, a DSC measurement was also conducted. The results can be seen in Table 6 and in the Annex C in Figure 46. As contaminations of Molybdenum were introduced into the specimens of the fourth printjob, the transition temperatures changed slightly compared to the parameter study. Notable is, that for the measurements of this printjob the results scatter considerably (see Figure 46) and therefore, the linear regression is connected with a significant uncertainty. Nevertheless, the measurements of the γ-Solvus temperature were very constant for all heating rates and showed good accordance with the parameter study. Therefore, heat treatments were adjusted according to the γ-Solvus temperature of the fourth printjob (see Table 6) since this was the printjob for the mechanical test samples. Schmölzer et al. [68] investigated the influence of Molybdenum on the phase transition and ordering temperatures in TiAl-Mo alloys. In general, Mo is stabilizing the β/β_o-phase and therefore competes with the high Al and O content. Furthermore, it is shown for the ternary Ti-Al-Mo system at low contents of Mo of 1 – 2 at.%, minor additions increase the eutectoid

transformation temperature T_{eut} significantly. This is in good accordance with the measured transition temperatures in the present work. Nevertheless, it has to be stated, that Mo is present in the form of particles (see Figure 30 in the next chapter) and to a lesser extent in solid solution.

Table 6: Phase transition temperatures of the TNM alloy measured by differential scanning calorimetry and compared to literature as stated by [20].

	T_{eut} [°C]	$T_{\gamma,solv}$ [°C]
Ref. measurement [20]	1160	1255
Parameter study	1199.5	1285.1
Fourth printjob	1226.7	1288.5

4.5 Microstructural Characterization

4.5.1 As-built Microstructure

As seen in Figure 28, the microstructure of the as-SLM specimen consists either of three phases α_2, β_o and γ (Figure 28a, d and e) or of two phases α_2 and γ (Figure 28 b, c and f). Generally can be stated, that the microstructural evolution is dependent from the preheat temperature, the laser power, the scan speed and from that the laser energy which is introduced into the specimen. The higher the introduced energy either by preheat temperature or by laser energy, the coarser the microstructure is. Furthermore, the higher the introduced laser energy was, for a given preheat temperature, the more Al evaporated and therefore the phase composition changed. For lower laser energies (Figure 28a, b, c and f), mainly a microstructure with hardly no β_o-phase is observable due to the minor overall Al evaporation. In contrary, for higher laser energies (Figure 28d and e), a microstructure with a significant amount of β_o-phase is observable due to an enhanced overall Al loss. Therefore, the required microstructure and thereof the resulting properties can be already set by the manufacturing process. What is more, a graded microstructure from the bottom of the specimen up to the top was visible, whereas the center showed coarser grains than the top area of the specimen (see Annex D, Figure 48). This is a result from the layer-wise manufacturing of the samples. The heat affected zone of the overlying layer is equating to a heat treatment for the previous layers. Combined with the dwell time on high preheat temperatures, a diffusion-controlled coarsening of the microstructure as a function of the sample height can be observed. Therefore, a very fine lamellar microstructure which is ideal for further heat treatments occur at the marginalized layers.

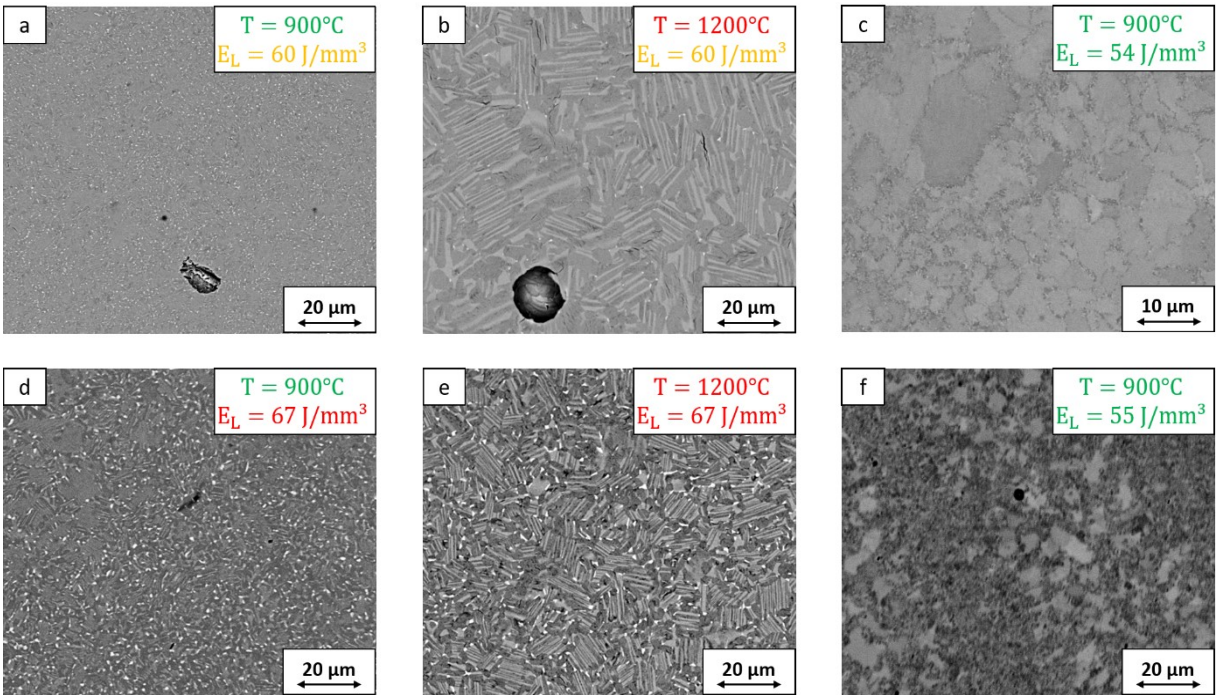

Figure 28: SEM images in BSE contrast of as-SLM specimens: (a) Printjob 1, specimen 2.1 with a very fine microstructure; (b) Printjob 2, specimen 2.1 with a coarser microstructure at the center of the specimen due to a higher preheat temperature; (c) Printjob 3, specimen 1.2 with a very fine NLγ microstructure; (d) Printjob 1, specimen 2.3 with a coarser microstructure due to introducing higher energy compared to (a); (e) Printjob 2, specimen 3.4 with coarser microstructure; (f) Printjob 4 with a very fine NLγ microstructure compared to the other printjobs.

To analyze the phase fraction quantitatively, XRD measurements of all printjobs were conducted (see Figure 29). For all printjobs, the content of β_o-phase stayed approximately the same. For printjob 1 and printjob 2, the same parameters ($P_L = 60$ W, $v_s = 300$ mm/s and $E_v = 66.7$ J/mm^3) were applied and therefore a direct comparison of the different preheating temperatures of 900°C (printjob 1) and 1200°C (printjob 2) can be made. For printjob 2, the influence of the higher thermal energy introduced into the material is visible, because at this temperature more α_2-phase is stable in thermodynamic equilibrium [20]. For printjobs 3 ($P_L = 160$ W, $v_s = 1066$ mm/s and $E_v = 50$ J/mm^3) and printjob 4 ($P_L = 140$ W, $v_s = 848$ mm/s and $E_v = 55$ J/mm^3), the introduced energy was lower than for the first two printjobs. Therefore, the phase composition tends to be more on the thermodynamic equilibrium with a higher γ-phase content. Moreover, an influence of the SLM process on the grain size and the aspect ratio of the microstructure is visible. Due to the unique conditions of the laser melting (see Figure 32), a bimodal grain size distribution is developed, as clearly shown in Figure 28f and is also reported for various materials manufactured by SLM [13,16,28]. Also, island borders and the laser scan direction can be seen in the metallographic cross-sections (see Figure 33) which is a result of different phase fractions, respectively local differences in the chemical compositions. The hardness of the as-SLM specimen is shown in Annex D, Table 13. Compared to the conventional manufactured material [20], the SLM specimen had improved hardness values with an average of 465 HV10.

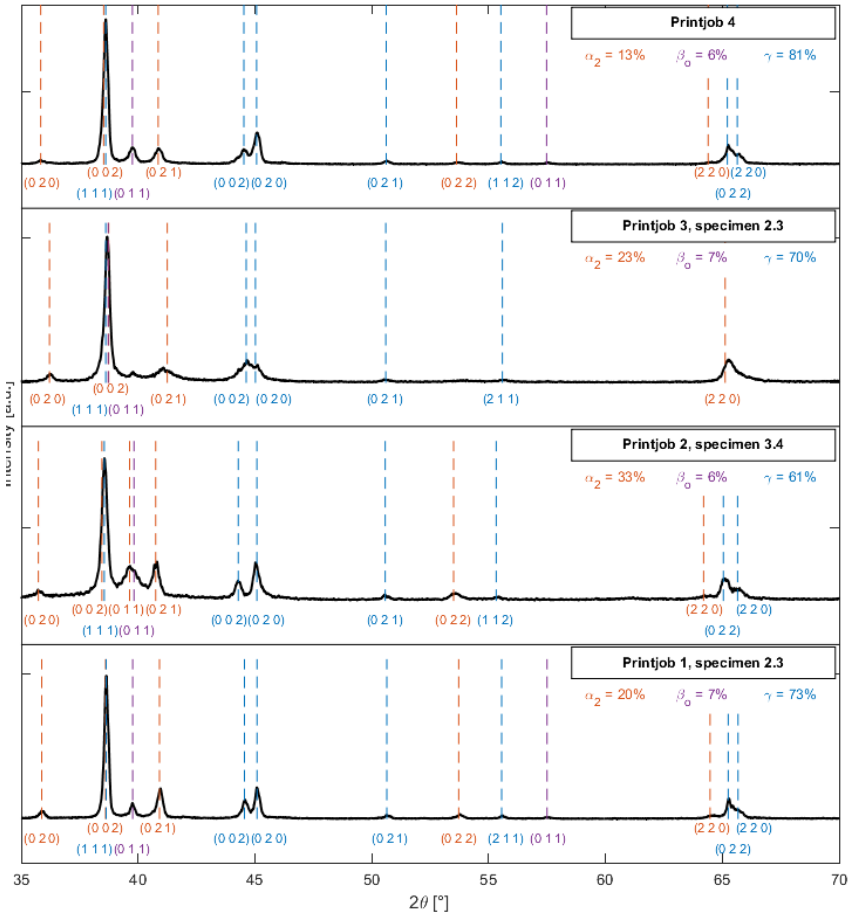

Figure 29: XRD measurements of as-SLM samples of all four printjobs: For printjob 1 and printjob 2, the same parameters were used but different preheating temperatures were applied. For printjob 3 and printjob 4 lower energies were applied.

The composition of the bulk material, as conducted by GfE Metalle und Materialien GmbH, is a mean value over the whole specimen, whereas locally fluctuations are not considered in this analysis. For a local chemical analysis, microprobe measurements at the Department of Applied Geological Science and Geophysics, Chair for Resource Mineralogy at the Montanuniversität Leoben, Austria, were conducted. As the SEM images already showed, only the as-SLM material has visible chemical inhomogeneities, which can be concluded on the different local amount of phase compositions. These inhomogeneities were reduced due to the HIP- and heat treatment. Therefore, line analysis and chemical mapping were conducted at as-SLM specimens and on the single line experiments. Above all, there is a major amount of spherical Mo particles with an average particle size diameter of 30 µm in the microstructure (see Figure 30 a and b), which are evenly distributed over the whole samples of the fourth printjob. With the aid of the microprobe device, an Electron Dispersive Spectroscopy (EDS) was conducted to evaluate the composition of the particle qualitatively. As shown in Figure 30 c and d, the core of the particle consists of nearly pure Molybdenum and the developing shell consists of Mo beside the major contributions of the bulk composition. The core to shell ratio decreased by exposure of temperature due to diffusion processes. This Mo-contamination is a consequence of an insufficient cleaning of the SLM machine. To avoid such cross-contaminations structural improvements on the device were made, as described in 3.2.2.

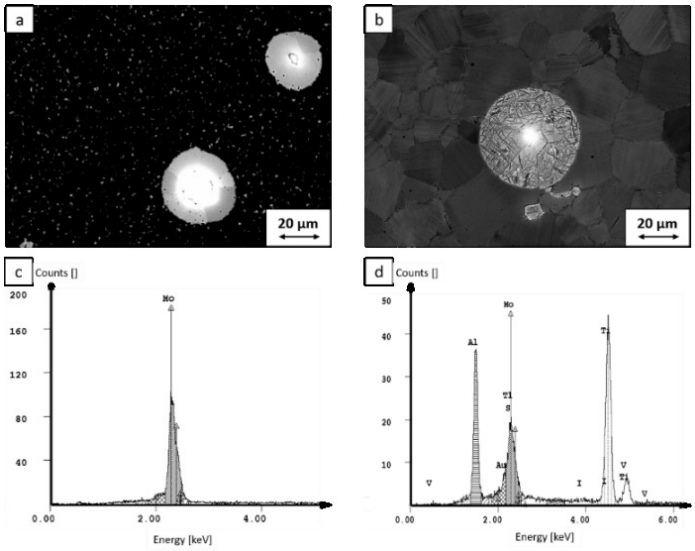

Figure 30: Molybdenum particles due to insufficient cleaning of the SLM machine.(a) as-HIP state of the specimen with core-shell Mo particles dependent on diffusion, the small white dots represent the remaining β_o-phase; (b) heat treated specimen with an decreased core-shell ratio due to diffusion of Mo into the bulk material; (c) EDS spectrum of the core of the particle revealing a pure Mo composition; (d) EDS spectrum of the shell of the particle revealing a combined Mo and bulk composition due to diffusion processes occuring at elevated temperatures.

Due to the alternating structure of the as-SLM specimen with different phase fractions, a mapping of the most important alloying elements (Ti, Al, Nb, Mo, O) was conducted and is shown in Figure 31. As the mapping in the ROI reveals, for the as-SLM specimen 3.4 of printjob 2 (see Figure 31), that the chemical distribution of the alloying elements Mo and Nb are very homogeneous. A closer inspection of the alternating structure of the as-SLM specimen regarding the Al content revealed a weak pronounced inhomogeneous structure, according to the structure seen in the SEM (see Figure 31, dashed lines). Within the brighter areas of the SEM image, less Al was detected. This is also consistent with the phase diagram, as the brightest areas of the SEM image contain a higher amount of β_o- and α_2- phase. In contrary, the darker areas of the SEM image, which consist therefore of more γ-phase, are enriched in Al. Although O cannot be detected quantitatively, the O mapping was conducted to analyze any oxygen enrichments or oxide precipitations. The mapping shows that the oxygen content is below the resolution limits of the microprobe and no precipitations formed during the process.

A simulation of the temperature distribution within the melt pool for a AlMgSc alloy was conducted by Spierings et al. [28] and is shown in Figure 32. Although the laser energy and the thermal material properties differ between the AlMgSc and the TNM alloy, the underlying concept of the simulation can be transferred as the basic principles are qualitatively equal. The temperature gradient for the aluminum alloy within the melt pool is indicated by isothermal lines (see Figure 32) and shows a radial decreasing temperature from the point of impact by the laser on the surface. This thermal distribution derives from the unique heat input and cooling conditions, which vary within the melt pool. As the aluminum loss for the TNM alloy is a function of temperature, more aluminum will evaporate at areas with higher temperatures, i.e. near the point of impact, and consequently the aluminum loss is less pronounced at areas with lower temperatures, i.e. further away from the point of impact. This

leads to a local chemical difference within the melt track as also reported by the microprobe measurements in Figure 31. With Figure 33, a top view on the melt pool is provided. For areas with higher Al loss the chemical composition in the phase diagram shifts to lower Al contents and according to the lever rule, more β_o-phase is developing. This is also visible in the SEM images by the brighter areas (see Figure 33). In contrary, areas with lower Al loss and therefore with more γ-phase occur darker in the SEM image. The alternating structure of bright and dark areas at the top view is in accordance with the hatch distance of 100 µm. The typical SLM structure with the phase distribution is also visible for the cross-section of the melt track. This reflects the temperature distribution of the simulation in [28].

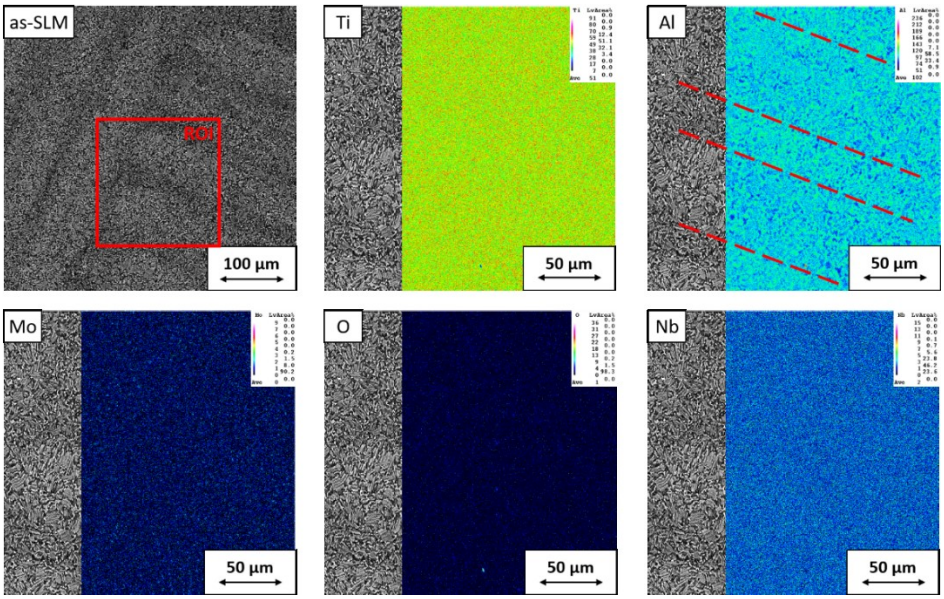

Figure 31: Microprobe mapping of the main alloying elements Ti, Al, Nb, Mo and O of specimen 3.4 of the second printjob in the area of an island border, where the red area marks the region of interest (ROI): very homogeneous distribution of the alloying elements Nb and Mo; Al shows an alternating concentration-profil due to the layer-wise manufacturing of the specimen, as the dashed line indicates; the O content is not detectable for the mapping and a higher local distribution can be ruled out.

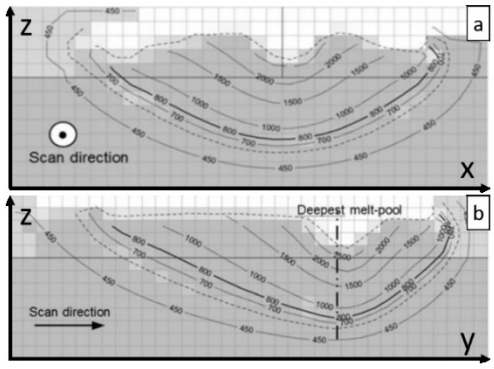

Figure 32: Meltpool Simulation according to Spierings et al. [28] for a AlMgSc alloy with an indicated temperature gradient as isothermal lines which can be transferred qualitatively to the TNM alloy; (a) shows a cross-section of the position with the deepest melt pool perpendicular to the scan direction of the laser and (b) shows a cross-section parallel to the scan direction of the laser.

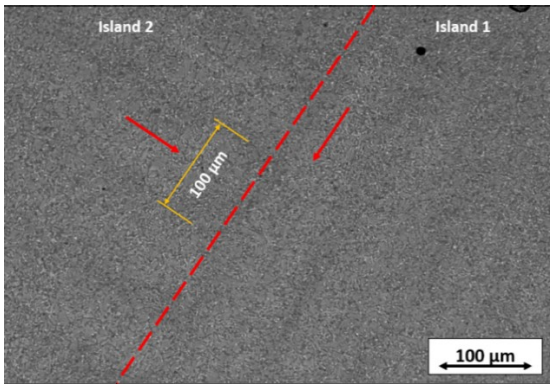

Figure 33: As-SLM microstructure of specimen 2.2 of the second printjob with a clearly visible island boarder. The single laser tracks of the processing can be seen and correlate with the hatch distance of 100 µm.

To evaluate near-equilibrium state of the as-SLM microstructure, specimen 2.1 of the second printjob was annealed at 1100°C for 4h with FC. The annealed specimen revealed no significant change in the microstructure compared to the as-SLM specimen. As a consequence, it can be assumed, due to the high preheat temperature of 1200°C for this specimen and the ongoing heat treatment by the overlying layers, that this process is close to thermodynamic equilibrium. Only a minor grain growth and broadening of the lamellae was visible.

4.5.2 Heat-Treated Microstructure

Due to the higher Oxygen content of the as-built SLM specimen, an α-single-phase field occurred according to the DSC measurements (see chapter Annex C). This phase field can be used to achieve a FL microstructure. This microstructure shows an optimized creep resistance. Due to the absence of a second phase, there is still the danger of an uncontrolled grain growth and, hence, a lower ductility at RT [69]. A NLγ microstructure has balanced mechanical properties in terms of high-temperature creep resistance and fracture toughness at room temperature [5,9]. The respective phase transition temperatures, especially the γ-solvus temperature, have a major influence on the performance of the heat treatment and the resulting microstructure. As for the first three printjobs, the γ-solvus temperature was around 1285.1°C, for the fourth printjob it was at 1288.5°C.

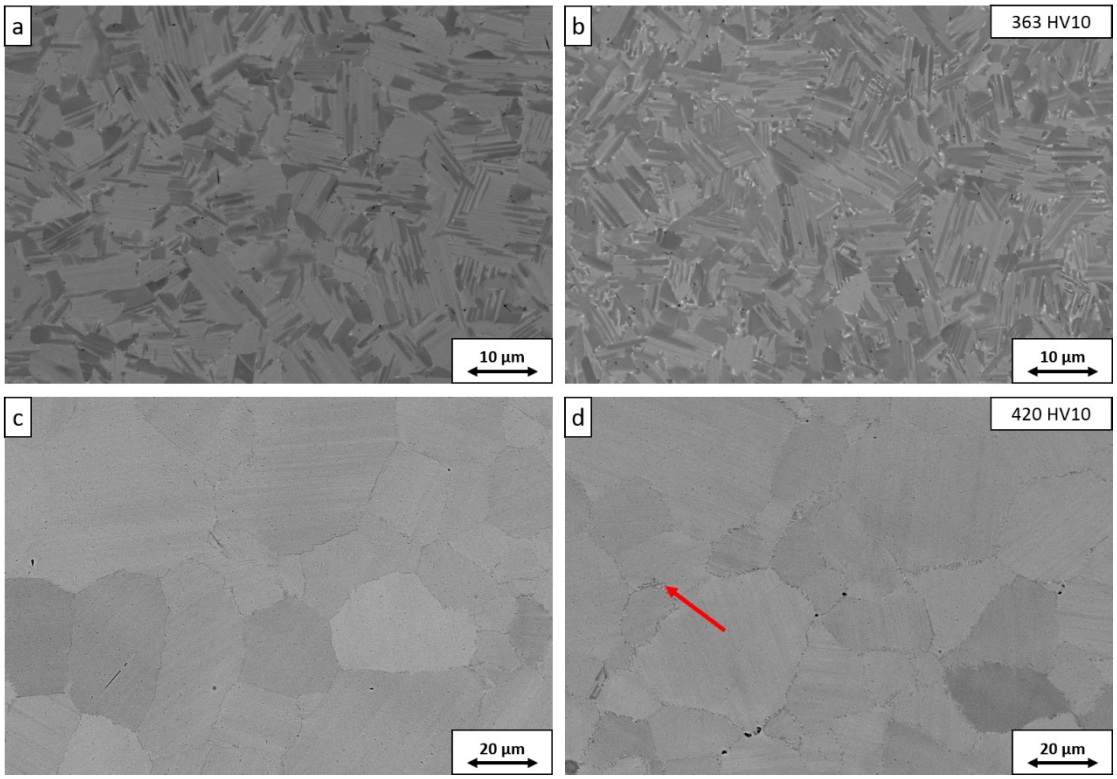

Figure 34: Microstructure of the heat treated specimens determined by SEM: (a) Annealed specimen (1250°C / 30min / AC) shows supersaturated α_2 (bright) and γ-phase (dark); (b) Annealed (1250°C / 30min / AC) and tempered (850°C / 6h / FC) specimen shows a NLγ microstructure with α_2- (bright), γ- (dark) and β_o-phase (white points); (c) Annealed (1300°C / 30min / AC) shows supersaturated α_2-grains; (d) Annealed (1300°C / 30min / AC) and tempered (850°C / 6h / FC) shows a FL microstructure with α_2-/ γ-colonies, where the small lamellae are not visible due to the limited spacial resolution of the SEM, the red arrow marks cellular reactions at the grain boundaries of the colonies.

For a nearly lamellar γ (NLγ) microstructure, the specimen has to be annealed about 30°C underneath the γ-solvus temperature with a subsequent rapid cooling, as already stated by [20]. Therefore, a microstructure of supersaturated α_2- and γ-phase is achieved (see Figure 34a). With an ageing treatment at 850°C for 6h and FC, within the supersaturated α_2-phase, lamellas of γ are precipitating (see Figure 34b). This heat treatment is HT2 according to Figure 17. At this point it can be seen, that the occurring γ-phase has a blocky formation compared to the globular morphology described in [5,9,20] for conventionally produced TNM.

For a FL microstructure, the specimen has to be annealed in the α-single-phase field above the γ-solvus temperature (see HT4 in Figure 17), whereas grain growth has to be taken into account. Therefore, approximately 20°C above $T_{\gamma,solv}$, an annealing was conducted to obtain after fast cooling supersaturated α_2-grains (see Figure 34c). Already after 0.5h of annealing, grain growth within the microstructure is visible, compared to the as-SLM specimen (Figure 28). After the ageing step, within the supersaturated α_2-phase γ-lamellas are formed (see Figure 34d). Furthermore, cellular reaction can be observed, as marked by a red arrow in Figure 34d. This discontinuous precipitation process can be observed for materials with nano-lamellar spacing as described by Guyon et al. [70]. At this effect, the elastic coherency strain and the stored interfacial energy is the driving force for a recovery process, leading to the formation of globular grains of γ, α_2 and β_o at the grain boundaries of the α_2/γ-lamella colonies. This discontinuous precipitation leads to a degradation of mechanical properties by decreasing strength along with deteriorating creep properties due to an eased dislocation movement within coarse γ-lamellas or globular γ-grains at the grain boundary as investigated by Kastenhuber et al. [71]. Therefore, minimization of this discontinuous precipitation is an important factor to enhance the mechanical properties of the specimen. In Annex D, Figure 49, a comparison of the two heat-treated microstructures (NLγ and FL) is given. For the NLγ microstructure, an enhanced γ phase fraction was measured compared to the FL microstructure. This is due to the additional globular γ-phase at the grain boundaries of the α_2/γ- colonies. Noticeable is a residual β_o-phase occurring in the FL-microstructure, which is might be due to cellular reactions, where β_o is also forming [70]. Nevertheless, it has to be stated, that the measurement error of XRD with Rietveld analysis is up to 3% for perfectly isotropic materials. The data obtained by XRD-measurements showed very good agreement with previous data from literature [20]. Furthermore, no major inhomogeneities were noticeable for HIPed and heat-treated specimens (see Figure 35). The welding structure due to the manufacturing process, which was clearly visible at the as-SLM samples (see Figure 33), was not observable after proceeding heat treatments. As given in Annex D, Figure 50, XRD-measurements of the different microstructural states of the printjob 4 were conducted to evaluate the influence of the respective treatment quantitatively. As already shown in Figure 29, the phase distribution of the as-SLM specimen of the fourth printjob has an enhanced content of γ-phase, compared to the other printjobs. This can be led back to the lower laser power and therefore the lower overall energy introduced into the material during the manufacturing process. Nevertheless, due to the preheat temperatures of 900°C, very fine distributed β_o phase is already forming by means of diffusion-controlled processes, as

indicated by XRD. For HIP treatment, the specimens were exposed to temperatures slightly underneath the eutectoid temperature and therefore it can be seen as a homogenization by diffusion annealing. This treatment reduced chemical inhomogeneities in the specimen. The phase composition as obtained by XRD-measurements can be seen as an equilibrium state of the present alloy. Taking the high content of oxygen stabilizing the α/α_2-phase into account, this phase composition is in good accordance with the quasi-binary section of the TNM alloy system (see Figure 7b) as stated by Schwaighofer et al. [20]. The adjusted FL-microstructure of the fourth printjob showed very isolated cellular reactions at the grain boundaries. Therefore, no noticeable contents of β_o-phase were detected by XRD. Moreover, the phase composition measured by XRD is in good accordance with literature for similar microstructures [44]. Furthermore, hardness tests were conducted at various specimens, which can be seen in Annex DAnnex D, Table 13. The hardness values for the FL and the NLγ microstructure were in good accordance with [20].

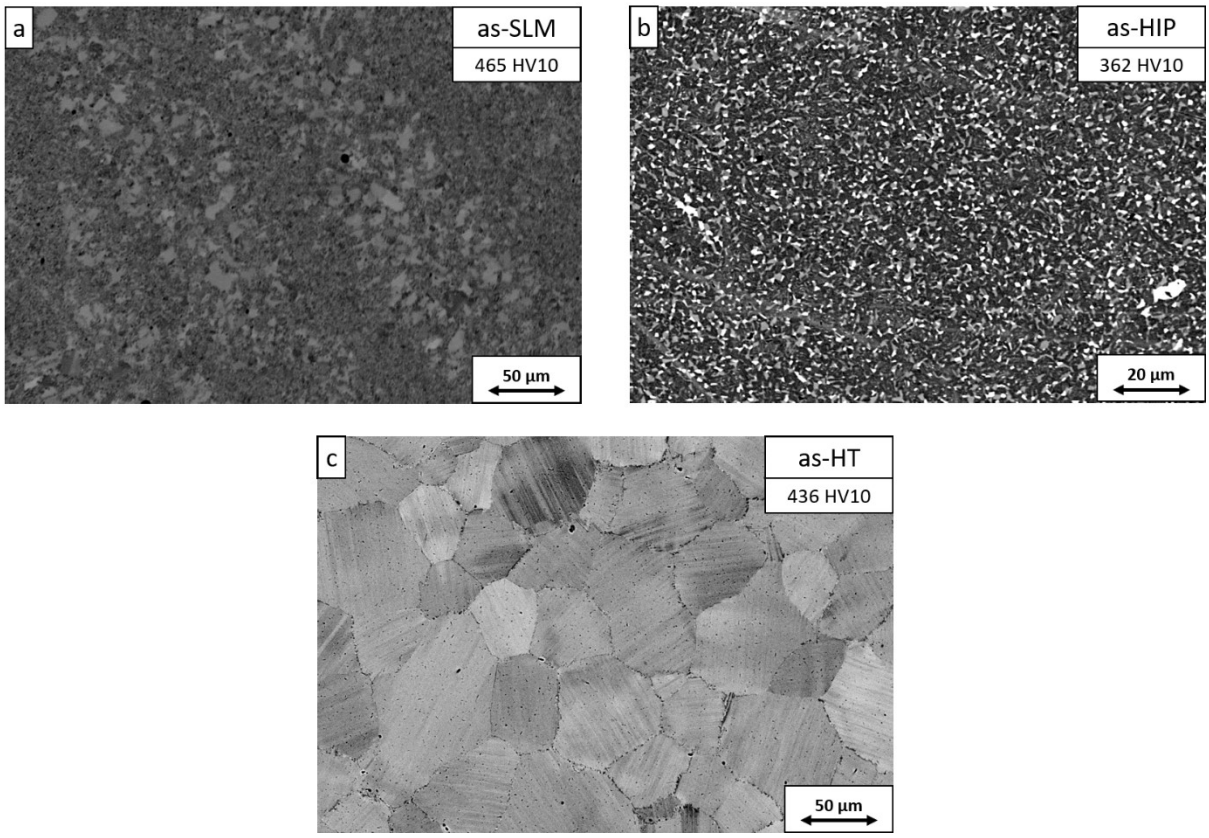

Figure 35: Microstructural evolution during the different heat treatment stages on a specimen of printjob 4: (a) shows an overview of the as-SLM specimen; (b) shows the microstructure after the HIP treatment, whereas relative coarse β_o-phase is visible and (c) shows the FL microstructure of the heat-treated specimen.

As stated in ref. [44], the absence of β_o-phase contributes positively to a reduction of the creep strain and a decrease of the minimum of the creep rate. Moreover, there is no according literature for the blocky shaped γ-phase and the influence of the shape onto mechanical properties. For those reasons, the favorable microstructure for high-temperature mechanical tests is a FL microstructure, which was finally adjusted for all mechanical test specimens.

4.5.3 Single Line Experiment

A Single Line (SL) experiment was conducted to get a profound understanding of the melt pool dynamics and solidification. Therefore, cross-sections of the SL experiments were made and chemical analysis by microprobe as well as EBSD measurements were conducted. A closer look at the microstructure revealed a very pronounced solidification structure as seen in Figure 36a. With higher magnification, a growth of formerly β-grains was visible, whereas non-favorable grains were stopped by the growth of favorable grains (see Figure 36b). The substructure suggests a $\beta \rightarrow \alpha$ and a lamellar reaction during subsequent cooling. This diffusion controlled process might occur due to the high preheat temperature of 900°C. As seen in Annex D, Figure 51b, phase fraction measurements revealed that the major phases are the α_2- and γ-phase. Compared to the work conducted by Bürstmayr [51], the β-solidification results in a very pronounced texture of the microstructure. This was not observable in the present work, whereby it can be assumed that the solidification is peritectical. For rapid solidification, a massive type transformation $\alpha \rightarrow \gamma_m$ occurs most likely, which can be assumed by the phase fraction measurements. As this transformation requires short-range diffusion since no composition change has to take place, it is in contradiction to the SEM images in Figure 36. The clarification of the phase transformation of the γ-phase was not delivered with the tests conducted in this work and so further investigations by means of transmission electron microscope (TEM) have to be made. What is more, the EBSD measurements revealed a preferred crystal orientation, in terms of an orientation of the (0001) basal levels of the hexagonal α_2-phase crystal mostly radial outwards (see Annex D, Figure 51c). Here it can be assumed, that crystal growth occurs along the highest temperature gradient. Non-favorable crystal orientations, which were not orientated according to the temperature gradient were overgrown by favorable grains. This could be observed in the root of the single line, as the plotted crystals of the smaller grains are randomly distributed. As many of the crystal structures in Figure 51c were slightly tilted, it can be assumed that the laser moving direction was pointing out of the cross-sectional plane. At the top and to some degree at the sides of the SL, higher cooling rates are assumable and therefore small randomly oriented grains were visible. The results of the EBSD measurements were in good accordance with the melt pool analysis of [28] in terms of temperature distribution. For the single line experiment, a very homogeneous distribution of the alloying elements was observable, compared to the cast material used as baseplate (see Figure 37). Nevertheless, a slight gradient of the Al content was visible, whereas the top of the SL showed a higher concentration of Al than the bottom of the SL. This could also be seen by the phase composition in the SEM image, whereas the upper part of the melt pool is clearly darker, which indicates a higher content of γ-phase. A reason for this phenomenon is the different chemical compositions of the powder and the baseplate material. As the baseplate material was taken from previous investigations by Schwaighofer et al. [20], the overall chemical composition of the powder and the baseplate differed of about 1.5 at.% Al, as already stated in Table 5. The solidification structure , as visible in the SEM image (see Figure 36), cannot be imaged by the chemical mapping due to resolution limits of the used device.

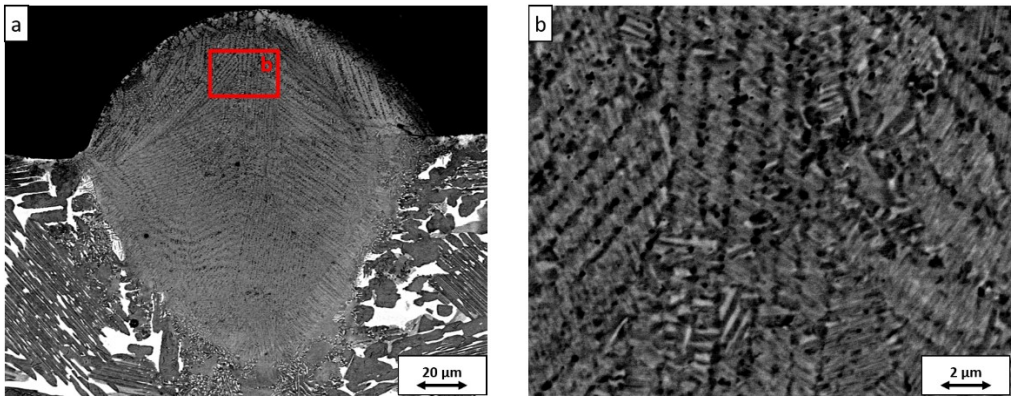

Figure 36: SEM image of the microstructure of a Single Line Experiment: (a) overview of the whole single line with very pronounced solidification structures and (b) a detail image of the marked area revealing stem like structures whereas non-favorable directions were overgrown by favorable directions.

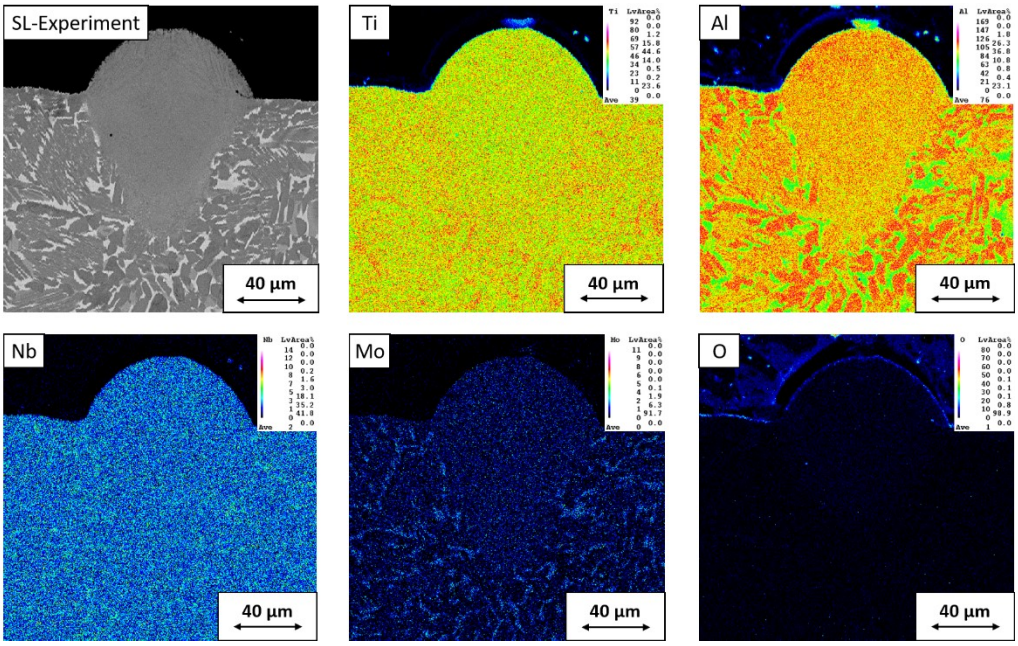

Figure 37: Microprobe mapping of the main alloying elements Ti, Al, Nb, Mo and O of a cross-section of a single line experiment: very homogeneous distribution of the alloying elements Nb, Mo and O; Al shows a slight gradient from areas of higher Al content at the top to areas of less Al at the bottom of the singe line; the O content is not detectable for the mapping.

4.6 Mechanical Testing

For all mechanical tests, the SLM specimens were heat treated according to chapter 3.5.2 to adjust a FL microstructure.

4.6.1 Three-Point Bending Tests

For the three-point bending test four TNM SLM specimens and one TNM PM specimen were tested. For any further information regarding the chemical composition, manufacturing and heat treatment, the reader is referred to chapter 3. The results of the tests are shown in Figure 38 and Annex E, Table 14. The red marked area at the beginning of the testing indicates influences of the testing machine in terms of adjusting of the support rollers and therefore,

this phenomenon will not be further discussed. The experimental data of the 3-Point-Bending tests are in good accordance with literature [20,44,51,72,73], where the obtained data are also compared to tensile tests at room temperature. The according fracture surfaces can be seen in Annex E, Figure 52. The TNM SLM specimens show a brittle transgranular fracture surface, where a delamination of single lamellas is visible (see Figure 52a and b). This behavior is visible for all TNM SLM specimens, tested within this work. Compared to the TNM PM specimen, an intergranular fracture is observable (see Figure 52c and d).The size of the individual grains for the PM specimen is about 20 µm which is approximately the same for the SLM specimen (see Figure 39).

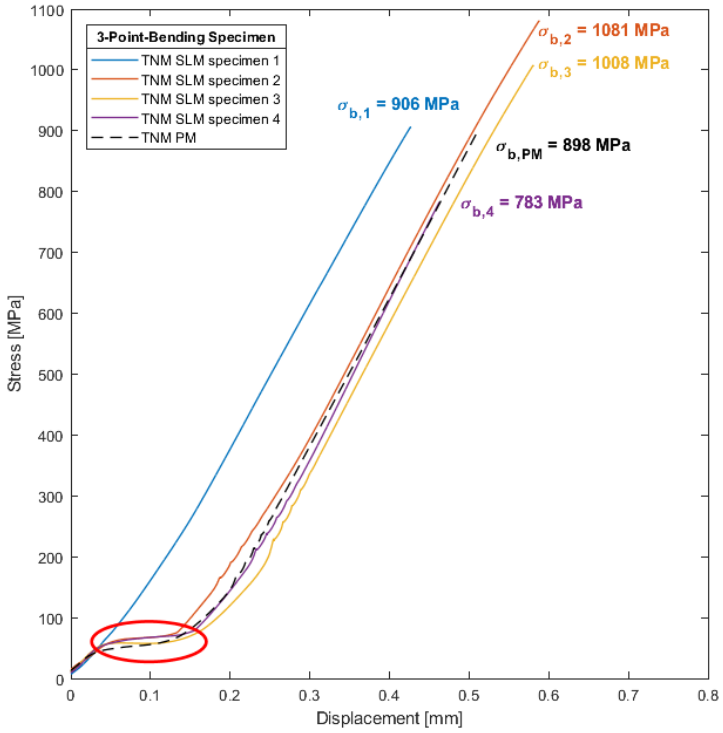

Figure 38: Results of the 3-Point-Bending Tests of the TNM SLM specimen 1 - 4 and of a TNM PM reference sample for comparison; red circle indicates influences of the testing machine at the beginning of the test cycle.

4.6.2 Creep Tests

For the creep tests, three specimens were manufactured with the same parameters and exposed to the same heat treatments as stated in chapter 3.2.2 and 3.5.2. Due to Mo impurities, discussed below, the first creep specimen fractured during preloading while installing into the testing machine. Hence, the installation sequence was adapted for the second specimen. For preloading a steel specimen was used to adjust the weights. Afterwards the steel specimen was removed, and the second creep specimen was installed and heated up to test temperature. As the first specimen, the second broke as well during loading at a stress of 150 MPa. The recorded data can be seen in Annex F, Figure 53. As a consequence, the test procedure for the third specimen was again adapted to a multi-stage creep test where the load was reduced from 170 MPa to 100 MPa for the first, 135 MPa for the second and 150 MPa for the third stage. For these reduced loads, a creep test could be conducted as shown in Figure 40 and Figure 41. The microstructure of the creep specimen prior to testing were

analyzed at the screw thread of the first fractured specimen (see Figure 39). Hence, the microstructure was adjusted to a FL microstructure. The Mo impurities, as seen in Figure 39b, are also regularly distributed over the whole specimen.

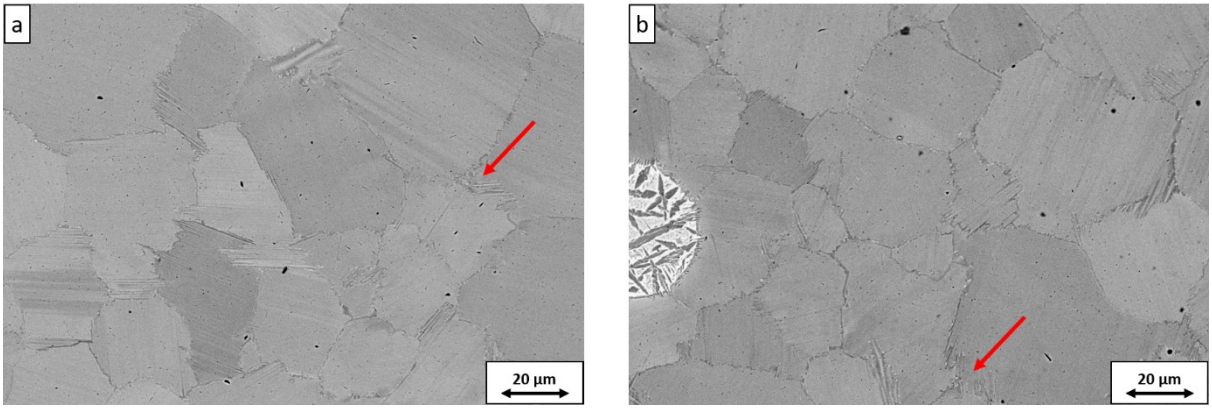

Figure 39: FL microstructure of the heat-treated creep specimen: (a) shows the upper screw thread and (b) shows the lower screw head; the bright spherical impurity in (b) shows a Mo impurity as they are regularly distributed over the whole specimen; red arrows mark pronounced interlocking of lamellar colony grain boundaries.

In Figure 40, the creep curve as a function of the exposed time of the creep specimen is shown. By means of a Levenberg-Marquardt-Alogrithm (see Annex F, Figure 54), the coefficients for the fitting function were calculated and the function was plotted. According to this fitting, the strain rate was plotted over the strain (see Figure 41).

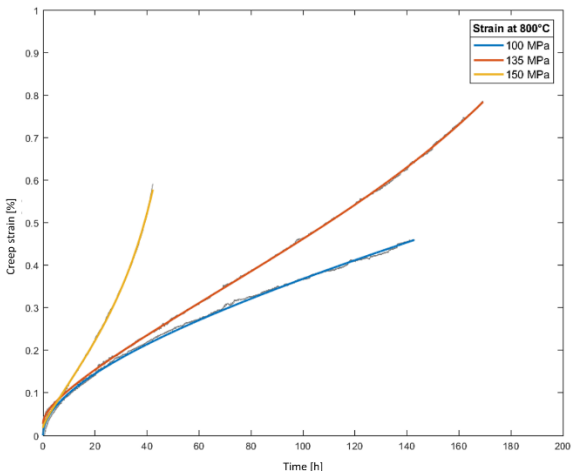

Figure 40: Time-strain-graph for the third creep specimen at 800°C and 100 MPa with the according fitting function and parameters obtained by Levenberg-Marquardt-Algorithm.

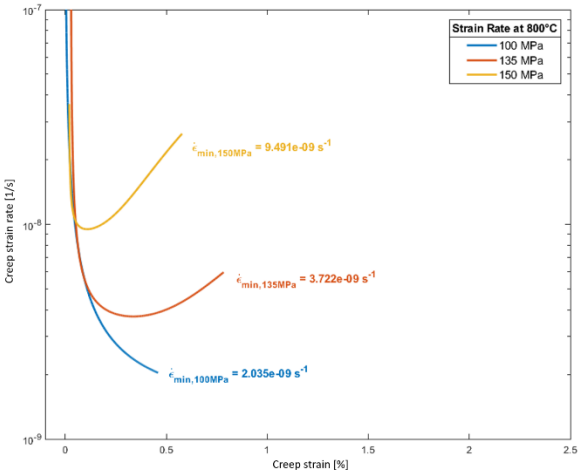

Figure 41: Strain rate-strain-graph for the third creep specimen at 800°C and 100MPa with the according minimal creep rate.

As already reported in literature by Kassner [74] and observed in the present work, γ-TiAl does not exhibit a pronounced steady-state creep stage but a minimum of the strain rate. In addition, when increasing the stress of the creep test, the stress exponent increases as well accepting values from 1 up to 20 [74]. The different appearance of the creep curves can be lead back to the complex microstructure and the enhanced number of influence parameters as described by [74]: grain size of the lamellar α_2/γcolonies, lamellar spacing, orientation of

the lamellas, volume fraction of precipitations, volume fraction of globular phases along the lamellar colony grains and morphology of the grain boundaries.

For the present work, the minimum of the strain rate was calculated as $\dot{\varepsilon}_{\mathrm{min,100MPa}} = 2.035 \cdot 10^{-9}\, s^{-1}$, $\dot{\varepsilon}_{\mathrm{min,135MPa}} = 3.722 \cdot 10^{-9}\, s^{-1}$ and $\dot{\varepsilon}_{\mathrm{min,150MPa}} = 9.491 \cdot 10^{-9}\, s^{-1}$ (see Figure 41). It is noteworthy, that the third stress was initiated when the sample already exhibited a pronounced increase of the strain rate for the second stress level. Therefore, the third stress level was tested, although the specimen was already subjected to major internal pores, as commonly reported for the third creep stage. For any further evaluation, the minimum of creep stress for 150 MPa was not considered. Due to the early failure of the first specimens and thus, a concomitant reduction of the stress, no literature data with the same parameters are available. Consistently, Hsiung et al [75] predicted for similar parameters a strain rate minimum of 10^{-9} to $10^{-8}\, s^{-1}$. Nevertheless, similar tests were conducted by [43,44,60,75,76] at slightly different temperatures or slightly different creep strains. Kastenhuber et al. [43,44,71] investigated the influence of temperature and strain on various TNM and TNM^{+} alloys, whereas TNM^{+} are considered to have a higher creep resistance due to additions of C and Si. As shown in Table 7, the minimal creep stresses were lower than comparable PM specimen and HIP/cast specimen. It can be shown, that even at same stress levels and only slightly elevated temperatures, a NLγ microstructure exceeds higher creep rates than a FL microstructure. This is also in accordance with literature [44,74]. As visible in Figure 41, the slope at the end of the recorded strain rate for 100 MPa was still not horizontal, meaning the minimum was not yet reached. Hence, the minimum of the strain rates should be lower than listed in Table 7.

It has to be taken into account, that the parameters of the respective creep tests are slightly different. Therefore, the minimum creep rate $\dot{\varepsilon}_{min}$ is predicted by following equation for dislocation glide reported by Zhang et al. [77] to provide a basis for comparison:

$$\dot{\varepsilon}_{min} = K_0 \cdot e^{-\frac{Q_L}{RT_{abs}}} \cdot \sinh\left(\frac{\sigma}{\sigma_0}\right), \tag{4.1}$$

whereas $\mathrm{K_0}$ is a material constant, which is proportional to the dislocation source density and lattice diffusional coefficient, $\mathrm{Q_L}$ is the activation energy for lattice diffusion which is nearly constant for TiAl alloys with 375 kJ/mol, R is the gas constant, T_{abs} is the absolute temperature and σ_0 is considered to be the internal stress for dislocation movement. $\mathrm{K_0}$ is reported to be $2.17 \cdot 10^{9}\, s^{-1}$ for FL microstructures with very fine lamellas [77]. Therefore σ_0 was fitted according to the obtained data in the course of this work and the prediction of the strain rate minimum was plotted as a function of the applied creep stress (see Figure 42). As it can be seen, the results of the creep tests, as well as the prediction of the strain rate minimum were in good accordance with prior experiments conducted by Kastenhuber et al. [43,44,71], as the data were in the same magnitude.

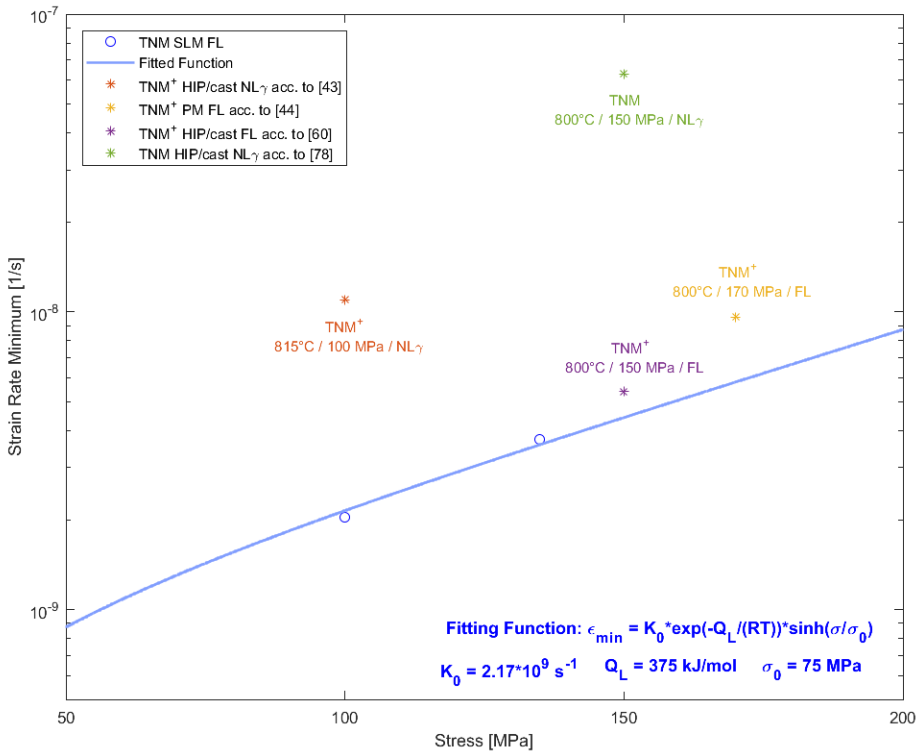

Figure 42: Prediction of the minimum of the strain rate according to the obtained data of this work (blue markers); red marker indicates the minimum of the strain according to literature [44].

The primary creep stage for TiAl was examined by Zhang et al. [78] and they found a relatively low dependency of the primary creep on microstructure below a certain threshold stress. As many application stresses does not exceed 150 MPa, primary creep is noteworthy for high stress applications only. Above the threshold stress, main mechanisms contributing to primary creep are stress-induced phase transformations, twinning and an enhancement in the dislocation density. Hsiung et al. [75] investigated the predominant creep mechanism of secondary creep within FL microstructures. Firstly, they exclude sliding of grain boundaries due to the interlocking of the boundary morphology. This special interpenetrating morphology can be observed especially in FL microstructures (see red arrow in Figure 39) and decrease creep rates due to missing of a slide-able boundary planes as observed for NL γ microstructures. They found as the predominant creep mechanism in the low stress regime interfacial sliding of lamellas due to Shockley dislocations resulting into stacking faults. After the creep tests, the specimens were analyzed in terms of fracture surface for specimen 1 and 2 and microstructural evolution during creep testing for specimen 3. The fracture surfaces of the premature broken samples are shown in Figure 43. An EDX measurement of areas with different appearance revealed major amounts of Nitrides and Oxides, which cover up a high proportion of the fracture surface (see Annex F, Figure 55 to Figure 58). Furthermore, hot crack like structures can be seen on the surface, indicating lack of fusions or other cavities. These phenomena weakened the material and caused premature failure of the specimens. As these defects occurred only at the creep specimens, it could be assumed, that an upscaling from the cubic specimen of the first printjobs to the creep specimen can not be done easily and require further parameter optimizations.

Table 7: Comparison of the SLM creep specimen with PM and HIP/cast specimen in terms of microstructure, creep stress, temperature, minimal creep rate and time of minimal creep rate.

	Microstructure []	**Stress** [MPa]	**Temperature** [°C]	$\dot{\varepsilon}_{min}$ [1/s]
TNM SLM	FL	100	800	$< 2.0 \cdot 10^{-9}$
TNM SLM	Fl	135	800	$3.7 \cdot 10^{-9}$
TNM SLM	FL	150	800	$9.1 \cdot 10^{-9}$
TNM⁺ PM [44]	FL	170	800	$9.6 \cdot 10^{-9}$
TNM⁺ HIP/cast [60] TNM+0.3C+0.3Si	FL	150	800	$5.4 \cdot 10^{-9}$
TNM⁺ HIP/cast [43] TNM+0.3C+0.3Si	NLγ	100	815	$1.1 \cdot 10^{-8}$
TNM⁺ HIP/cast [43] TN1.5Mo+0.5C	NLγ	100	815	$1.1 \cdot 10^{-8}$
TNM HIP/cast [76]	NLγ	150	800	$6.3 \cdot 10^{-8}$

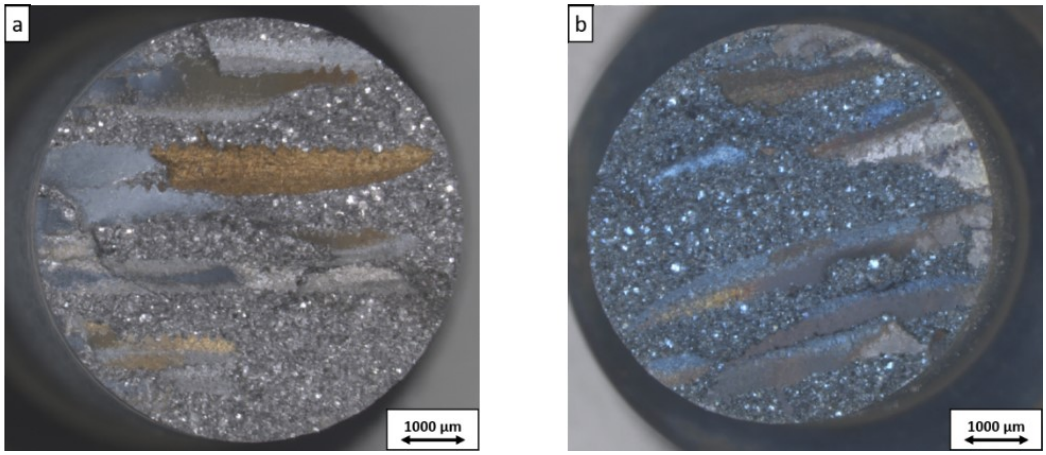

Figure 43: (a) Fracture surfaces of the creep specimen 1, cracked at room temperature while applying the load and (b) creep specimen 2, cracked at testing temperature of 800°C while applying the load.

The SEM images of the cross sections of the creep specimen showed the microstructural evolution during the creep testing (see Figure 59, Annex F). A higher fraction of pores compared to the not tested specimen was visible as the creep test was aborted in the third creep stage. This stage is characterized by the formation and growth of pores up to the fracture. Two different shaped types of pores are noticeable (see Figure 59a). On the one hand rounded shaped pores which very likely originate from the creep testing. On the other hand,

elongated shaped pores suggesting thermally stable nitride and oxide layers, which were observed at the fracture surface and did not spheroidize during the annealing treatment of the creep test. After an overall testing time of more than 385 hours at 800°C, very pronounced cellular reactions were observed at the grain boundaries, which are indicated by the red arrow in Figure 59b.

5 Summary and Outlook

The aim of this work was to evaluate the processability by means of SLM of an intermetallic β-solidifying titanium aluminide alloy, the so-called TNM alloy, by a parameter study. Furthermore, if the processability is given, a microstructure tailored for high temperature applications was adjusted and characterized. Subsequently, these results together with the mechanical tests were compared regarding already existing conventional TNM alloys.

First of all, a chemical analysis was conducted to evaluate the alloy composition before and after the SLM process. With regard to the process characteristics, the powder was alloyed with higher Al contents of 45 at.% compared to the conventional TNM alloys. As the process exceeds high temperatures within the melt pool, a selective evaporation of the element with the highest vapor pressure occurred, which is in the present work Aluminum. After processing the powder via SLM, the as-built specimens exhibited an Al concentration of approximately 43 at.%. What is more, a high impurity level of Oxygen of 1300 wt. ppm was already analyzed in the as-atomized powder and was increasing while manufacturing to up to 5400 wt. ppm. The insufficient cleaning of the SLM machine caused also cross contaminations with prior processed powders, leading to unusual alloying elements of the TNM system, like Fe or Cr. On this account and due to high melting points, Mo particles in an average size of 30µm were also visible in the microstructure.

Furthermore, a comprehensive study of the delivered feedstock powder was conducted. The powder batches had an average particle size of approximately 30µm. The surface of the powder was characterized in terms of satellites and solidification structure. XRD measurements revealed, that in the course of atomization and rapid cooling, the powder microstructure points to massive α_m or martensitic α'-phase. Only minor amount of β_o-phase occurs as interdendritic segregations. Due to diffusion-controlled processes, powder which was exposed to preheat temperatures up to 1200°C showed a globular microstructure with an increased content of β_o- and γ- phase.

The parameter study showed the influence of the preheat temperature, laser power, scan speed and line energy on the density and microstructural evolution of the specimen. The densities of the specimens were increased step by step due to the improvement of the parameters. Nearly dense specimens (ρ > 99.9%) were fabricated at printjob 3 and 4 with higher laser powers whilst reducing the line energy at the same time. The optimum regarding porosity was found for a laser power $P_L = 140W$, scan speed $v_s = 848\ mm/s$, resulting in a volume energy $E_v = 55J/mm^3$ and preheat temperature $T = 900°C$. Furthermore, it could be shown, that higher energies introduced into the system lead to a coarsening of the microstructure and a pronounced appearance of β_o-phase. This change of phase composition can be related to the selective evaporation of Al. According to the phase diagram of the TNM alloy under application of the lever rule, a loss of Al leads to an increase of the amount of β_o-phase. The microstructural evolution is strongly characterized by the melt pool, leading to chemical anisotropy. These alternating chemical compositions along the direction of building is characteristic for additive manufactured materials. Microprobe analysis revealed also this

chemical difference. Furthermore, a bimodal grainsize distribution within one laser track could be observed.

For the heat treatment study, DSC measurements were conducted to evaluate the respective temperatures of the HT. The temperatures, which are relevant for further heat treatments, are evaluated compared to data from literature. Due to the strong α/α_2 stabilizing effect of Oxygen and Aluminum, an α-single phase field occurred. This was proven with heat treatments in associated temperature field and a subsequent air cooling. Nevertheless, this presence enables the adjustment of a FL microstructure, which has optimized high temperature properties, compared to the NL γ microstructure. It was proved, that an annealing stage of 1300°C for 0.5h and a subsequent air cooling followed by a tempering stage of 850°C for 6h and a subsequent furnace cooling delivered a FL microstructure. The NLγ microstructure, obtained by decreasing the annealing to 1250°C, was characterized by a blocky-shaped γ-phase.

To evaluate the mechanical properties of the SLM specimen, three-point bending tests and creep tests were conducted. The bending tests revealed bending strengths comparable to data of literature. The fracture surface of the TNM SLM specimen showed a transgranular fracture, whereas the TNM PM reference sample revealed an intergranular fracture. The creep tests showed a minimum of creep rate comparable to literature data for FL microstructures, although the first creep specimens fractured while initial loading. The fracture surfaces were covered with oxide and nitride layers forming hot-crack-like structures. Beside this a brittle fracture surface was visible.

Intermetallic TNM alloys, manufactured by Selective Laser Melting, show a great potential regarding innovative production routes. Nevertheless, research faces different challenges regarding process technology and must overcome still existing obstacles to establish this processing as an alternative to conventional processing routes. First, the purity of the process has a major influence onto the feasibility of processing TNM with SLM, as interstitial impurities, like Oxygen, reduce the ductility noticeable and cross-contaminations of different processed powders might have a negative impact on the alloying composition and/or mechanical behavior. Furthermore, research work has to be done on process stability to ensure a fail-safe upscaling from testing specimens to structural components. From the physical metallurgy point of view, difficult processable metals, like intermetallic alloys, can be produced near-net-shape and therefore forging can be avoided. Furthermore, by adjusting the process parameters to an optimum for the microstructure, heat treatments can be conducted directly after the solidification of the melt pool within the installation space. For this reasons, expensive secondary treatments can be omitted, and the economic efficiency can be increased.

References

[1] IATA, Fact sheet climate change & CORSIA. www.iata.org/pressroom/facts_figures/fact_sheets/Documents/fact-sheet-climate-change.pdf. Januar 2019

[2] European commission, reducing emissions from aviation. ec.europa.eu/clima/policies/transport/aviation_en. Januar 2019

[3] IATA, 2036 forecast reveals air passengers will nearly double to 7.8 billion. www.iata.org/pressroom/pr/Pages/2017-10-24-01.aspx. Januar 2019

[4] B.P. Bewlay, S. Nag, A. Suzuki, M.J. Weimer, TiAl alloys in commercial aircraft engines, Materials at High Temperatures 33 (2016) 549–559.

[5] H. Clemens, S. Mayer, Design, processing, microstructure, properties, and applications of advanced intermetallic TiAl Alloys, Advanced Engineering Materials 15 (2013) 191–215.

[6] H. Clemens, H. Kestler, Processing and applications of intermetallic γ-TiAl-based alloys, Advanced Engineering Materials 2 (2000) 551–570.

[7] C. Leyens, M. Peters, Titanium and titanium alloys: Fundamentals and applications, Wiley-VCH, Weinheim, 2003.

[8] F. Appel, J.D.H. Paul, M. Oehring, Gamma titanium aluminide alloys: Science and technology, Wiley, Weinheim, 2012.

[9] S. Mayer, P. Erdely, F.D. Fischer, D. Holec, M. Kastenhuber, T. Klein, H. Clemens, Intermetallic β-solidifying γ-TiAl based alloys − from fundamental research to application, Advanced Engineering Materials 19 (2017) 1600735.

[10] D. Wimler, S. Kardos, J. Lindemann, H. Clemens, S. Mayer, Aspects of powder characterization for additive manufacturing, Practical Metallography 55 (2018) 620–636.

[11] Pratt & Whitney, Pratt & Whitney GTF PW1100G: PurePower PW1100G-JM engine cross section showing SKF products. news.cision.com/skf/i/purepower-pw1100g-jm-engine-cross-section-showing-skf-products%2Cc1290891.

[12] Ken Micallef, Airbus generates bionic design for flights of the future.

[13] W. Li, J. Liu, S. Wen, Q. Wei, C. Yan, Y. Shi, Crystal orientation, crystallographic texture and phase evolution in the Ti–45Al–2Cr–5Nb alloy processed by selective laser melting, Materials Characterization 113 (2016) 125–133.

[14] W. Li, J. Liu, Y. Zhou, S. Li, S. Wen, Q. Wei, C. Yan et al., Effect of laser scanning speed on a Ti-45Al-2Cr-5Nb alloy processed by selective laser melting: Microstructure, phase and mechanical properties, Journal of Alloys and Compounds 688 (2016) 626–636.

[15] W. Li, J. Liu, Y. Zhou, S. Wen, Q. Wei, C. Yan, Y. Shi, Effect of substrate preheating on the texture, phase and nanohardness of a Ti–45Al–2Cr–5Nb alloy processed by selective laser melting, Scripta Materialia 118 (2016) 13–18.

[16] J. Gussone, Y.-C. Hagedorn, H. Gherekhloo, G. Kasperovich, T. Merzouk, J. Hausmann, Microstructure of γ-titanium aluminide processed by selective laser melting at elevated temperatures, Intermetallics 66 (2015) 133–140.

[17] L. Löber, F.P. Schimansky, U. Kühn, F. Pyczak, J. Eckert, Selective laser melting of a beta-solidifying TNM-B1 titanium aluminide alloy, Journal of Materials Processing Technology 214 (2014) 1852–1860.

[18] G. Gottstein, Materialwissenschaft und Werkstofftechnik, Springer Berlin Heidelberg, Berlin, 2014.

[19] J.C. Schuster, M. Palm, Reassessment of the binary aluminum-titanium phase diagram, JPED 27 (2006) 255–277.

[20] E. Schwaighofer, H. Clemens, S. Mayer, J. Lindemann, J. Klose, W. Smarsly, V. Güther, Microstructural design and mechanical properties of a cast and heat-treated intermetallic multi-phase γ-TiAl based alloy, Intermetallics 44 (2014) 128–140.

[21] D. Hu, Role of boron in TiAl alloy development: a review, Rare Met. 35 (2016) 1–14.

[22] H. Clemens, S. Mayer, Intermetallic titanium aluminides in aerospace applications – processing, microstructure and properties, Materials at High Temperatures 33 (2016) 560–570.

[23] M. Schloffer, B. Rashkova, T. Schöberl, E. Schwaighofer, Z. Zhang, H. Clemens, S. Mayer, Evolution of the ω_o phase in a β-stabilized multi-phase TiAl alloy and its effect on hardness, Acta Materialia 64 (2014) 241–252.

[24] T. Klein, H. Clemens, S. Mayer, Advancement of compositional and microstructural design of intermetallic γ-TiAl based alloys determined by atom probe tomography, Materials 9 (2016).

[25] T. Klein, B. Rashkova, D. Holec, H. Clemens, S. Mayer, Silicon distribution and silicide precipitation during annealing in an advanced multi-phase γ -TiAl based alloy, Acta Materialia 110 (2016) 236–245.

[26] D. Herzog, V. Seyda, E. Wycisk, C. Emmelmann, Additive manufacturing of metals, Acta Materialia 117 (2016) 371–392.

[27] D. Gu, Laser additive manufacturing of high-performance materials, Springer Berlin Heidelberg, Berlin, 2015.

[28] A.B. Spierings, K. Dawson, T. Heeling, P.J. Uggowitzer, R. Schäublin, F. Palm, K. Wegener, Microstructural features of Sc- and Zr-modified Al-Mg alloys processed by selective laser melting, Materials & Design 115 (2017) 52–63.

[29] A. Gaitzenauer, M. Schenk, W. Kuchling, H. Clemens, P. Voigt, R. Hempel, S. Mayer, Gefüge und Eigenschaften einer mehrphasigen intermetallischen Titanaluminidlegierung für innovative Leichtbauanwendungen, Berg- und Hüttenmännische Monatshefte 158 (2013) 113–117.

[30] L.V.M. Antony, R.G. Reddy, Processes for production of high-purity metal powders, JOM 55 (2003) 14–18.

[31] M. Thomas, T. Malot, P. Aubry, C. Colin, T. Vilaro, P. Bertrand, The prospects for additive manufacturing of bulk TiAl alloy, Materials at High Temperatures 33 (2016) 571–577.

[32] Y. Liu, K. Chen, J. Zhang, Z. Hu, G. Lu, N. Kioussis, Electronic effects of oxygen and vanadium impurities in TiAl, Journal of Physics (1997) 9829–9843.

[33] T. Leitner, M. Schloffer, S. Mayer, J. Eßlinger, H. Clemens, R. Pippan, Fracture and R-curve behavior of an intermetallic β-stabilized TiAl alloy with different nearly lamellar microstructures, Intermetallics 53 (2014) 1–9.

[34] S.L. Semiatin, V.G. Ivanchenko, O.M. Ivasishin, Diffusion models for evaporation losses during electron-beam melting of alpha/beta-titanium alloys, Metall and Materi Trans B 35 (2004) 235–245.

[35] J. Schwerdtfeger, C. Körner, Selective electron beam melting of Ti–48Al–2Nb–2Cr: Microstructure and aluminium loss, Intermetallics 49 (2014) 29–35.

[36] H. Clemens, S. Mayer, Pulvermetallurgie von intermetallischen Titanaluminiden, Berg- und Hüttenmännische Monatshefte 160 (2015) 513–516.

[37] R. Gerling, H. Clemens, F.P. Schimansky, Powder metallurgical processing of intermetallic gamma titanium aluminides, Advanced Engineering Materials 6 (2004) 23–38.

[38] X. Zhou, K. Li, D. Zhang, X. Liu, J. Ma, W. Liu, Z. Shen, Textures formed in a CoCrMo alloy by selective laser melting, Journal of Alloys and Compounds 631 (2015) 153–164.

[39] Struers, Sicherheitsdatenblatt A3 (2017).

[40] W. Schatt, Pulvermetallurgie: Technologien und Werkstoffe, 2nd ed., Springer-Verlag Berlin Heidelberg, Berlin, 2007.

[41] G. Höhne, W. Hemminger, H.-J. Flammersheim, Differential scanning calorimetry: An introduction for practitioners, Springer-Verlag, Berlin, 1996.

[42] Y.-W. Kim, Ordered intermetallic alloys, part III: Gamma titanium aluminides, JOM 46 (1994) 30–39.

[43] M. Kastenhuber, Kurzzeitkriechverhalten intermetallischer TNM Titanaluminid-Legierungen. Masterarbeit, Leoben, 2013.

[44] M. Kastenhuber, T. Klein, H. Clemens, S. Mayer, Tailoring microstructure and chemical composition of advanced γ-TiAl based alloys for improved creep resistance, Intermetallics 97 (2018) 27–33.

[45] B. Heine, Werkstoffprüfung: Ermittlung von Werkstoffeigenschaften ; mit zahlr. Tabellen, 3rd ed., Fachbuchverl. Leipzig im Hanser Verl., München, 2015.

[46] F. Garofalo, D.B. Butrymowicz, Fundamentals of creep and creep-rupture in metals, Physics Today 19 (1966) 100–102.

[47] H. Haake, P. Riebensahm, P.W. Schmidt, Werkstoffprüfung, Springer Berlin Heidelberg, Berlin, Heidelberg, 1965.

[48] X. Shi, S. Ma, C. Liu, Q. Wu, Parameter optimization for Ti-47Al-2Cr-2Nb in selective laser melting based on geometric characteristics of single scan tracks, Optics & Laser Technology 90 (2017) 71–79.

[49] E.O. Olakanmi, R.F. Cochrane, K.W. Dalgarno, A review on selective laser sintering/melting (SLS/SLM) of aluminium alloy powders: Processing, microstructure, and properties, Progress in Materials Science 74 (2015) 401–477.

[50] GfE Metalle und Materialien GmbH, Product data sheet: titanium aluminides: γ-TiAl TNM - B1 Ingots. www.gfe.com/fileadmin/user_upload/pdfs/Produktspezifikationen_Titanium_Aluminides/PDB_gamma-TiAl_TNM-Ingot_V2.pdf.

[51] R. Bürstmayr, Additive manufacturing of a β-solidifying γ-titanium aluminide alloy. Masterarbeit, Leoben, 2018.

[52] D. Cormier, O. Harrysson, T. Mahale, H. West, Freeform fabrication of titanium aluminide via electron beam melting using prealloyed and blended powders, Research Letters in Materials Science 2007 (2007) 1–4.

[53] M.A. Morris, Dislocation mobility, ductility and anomalous strengthening of two-phase TiAl alloys: effects of oxygen and composition, Intermetallics (1996) 417–426.

[54] X. Wu, A. Huang, D. Hu, M.H. Loretto, Oxidation-induced embrittlement of TiAl alloys, Intermetallics 17 (2009) 540–552.

[55] T. Kawabata, T. Abumiya, O. Izumi, Effect of oxygen addition on mechanical properties of TiAl at 293–1273 K, Acta Metallurgica et Materialia 40 (1992) 2557–2567.

[56] A. Nérac-Partaix, A. Menand, Atom probe analysis of oxygen in ternary TiAl alloys, Scripta Materialia 35 (1996) 199–203.

[57] M. Lamirand, J.-L. Bonnentien, S. Guérin, G. Ferrière, J.-P. Chevalier, Effects of interstitial oxygen on microstructure and mechanical properties of Ti-48Al-2Cr-2Nb with fully lamellar and duplex microstructures, Metall and Mat Trans A 37 (2006) 2369–2378.

[58] A. Huang, M.H. Loretto, D. Hu, K. Liu, X. Wu, The role of oxygen content and cooling rate on transformations in TiAl-based alloys, Intermetallics 14 (2006) 838–847.

[59] J. Zollinger, J. Lapin, D. Daloz, H. Combeau, Influence of oxygen on solidification behaviour of cast TiAl-based alloys, Intermetallics 15 (2007) 1343–1350.

[60] T. Klein, L. Usategui, B. Rashkova, M.L. Nó, J. San Juan, H. Clemens, S. Mayer, Mechanical behavior and related microstructural aspects of a nano-lamellar TiAl alloy at elevated temperatures, Acta Materialia 128 (2017) 440–450.

[61] A. Strondl, O. Lyckfeldt, H. Brodin, U. Ackelid, Characterization and control of powder properties for additive manufacturing, JOM 67 (2015) 549–554.

[62] M. Kastenhuber, T. Klein, B. Rashkova, I. Weißensteiner, H. Clemens, S. Mayer, Phase transformations in a β-solidifying γ-TiAl based alloy during rapid solidification, Intermetallics 91 (2017) 100–109.

[63] S. Özbilen, Satellite formation mechanism in gas atomised powders, Powder Metallurgy 42 (1999) 70–78.

[64] C. Zhao, K. Fezzaa, R.W. Cunningham, H. Wen, F. de Carlo, L. Chen, A.D. Rollett et al., Real-time monitoring of laser powder bed fusion process using high-speed X-ray imaging and diffraction, Scientific Reports 7 (2017) 3602.

[65] C. Weingarten, D. Buchbinder, N. Pirch, W. Meiners, K. Wissenbach, R. Poprawe, Formation and reduction of hydrogen porosity during selective laser melting of AlSi10Mg, Journal of Materials Processing Technology 221 (2015) 112–120.

[66] T. Ma, R. Chen, D. Zheng, J. Guo, H. Ding, Y. Su, H. Fu, Effect of β-phase stabilizing elements and high temperature (1373–1693 K) on hydrogen absorption in TiAl alloys, International Journal of Hydrogen Energy 42 (2017) 86–95.

[67] Y. Su, X. Liu, L. Luo, L. Zhao, J. Guo, H. Fu, Hydrogen solubility in molten TiAl alloys, International Journal of Hydrogen Energy 35 (2010) 8008–8013.

[68] T. Schmoelzer, S. Mayer, F. Haupt, G.A. Zickler, C. Sailer, L. Lottermoser, V. Güther et al., Phase transition and ordering temperatures of TiAl-Mo alloys investigated by in situ diffraction experiments, MSF 654-656 (2010) 456–459.

[69] F. Appel, J.D.H. Paul, M. Oehring, U. Fröbel, U. Lorenz, Creep behavior of TiAl alloys with enhanced high-temperature capability, Metall and Mat Trans A 34 (2003) 2149–2164.

[70] J. Guyon, A. Hazotte, F. Wagner, E. Bouzy, Recrystallization of coherent nanolamellar structures in Ti48Al2Cr2Nb intermetallic alloy, Acta Materialia 103 (2016) 672–680.

[71] M. Kastenhuber, B. Rashkova, H. Clemens, S. Mayer, Effect of microstructural instability on the creep resistance of an advanced intermetallic γ-TiAl based alloy, Intermetallics 80 (2017) 1–9.

[72] H.Z. Niu, Y.J. Su, Y.S. Zhang, D.L. Zhang, J.W. Lu, W. Zhang, P.X. Zhang, Microstructural evolution and mechanical properties of a β-solidifying γ-TiAl alloy densified by spark plasma sintering, Intermetallics 66 (2015) 96–102.

[73] T. Voisin, J.-P. Monchoux, M. Hantcherli, S. Mayer, H. Clemens, A. Couret, Microstructures and mechanical properties of a multi-phase β-solidifying TiAl alloy densified by spark plasma sintering, Acta Materialia 73 (2014) 107–115.

[74] M.E. Kassner, Fundamentals of creep in metals and alloys, 3rd ed., Elsevier/Butterworth-Heinemann, Amsterdam, 2015.

[75] L.M. Hsiung, T.G. Nieh, Creep deformation of fully lamellar TiAl controlled by the viscous glide of interfacial dislocations, Intermetallics 7 (1999) 821–827.

[76] M. Schloffer, Gefüge und Eigenschaften der intermetallischen TNM-Legierung. Doctoral Thesis, Leoben, 2013.

[77] W.J. Zhang, S.C. Deevi, Analysis of the minimum creep rates of TiAl alloys, Materials Science and Engineering: A 362 (2003) 280–291.

[78] W.J. Zhang, S.C. Deevi, The controlling factors in primary creep of TiAl-base alloys, Intermetallics 11 (2003) 177–185.

Annex A

Table 8: Quantitative XRD analysis of the different powder fractions calculated by Rietveld refinement using Topas. Due to measurement and fitting inaccuracies, the fractions are given with a scattering of 3%.

	α_2 [%]	β_o [%]	γ [%]
Not heat affected powder (Batch 1)	98	2	0
Heat affected powder (Batch 1)	95	1	4
Sintered powder of 2. Printjob (Batch 1)	34	4	62
Not heat affected powder (Batch 2)	97	3	0

Annex B

Table 9: Analyzed geometrical factors for the powder without an influence of temperature, the powder with influence of temperature and the sintered powder conducted by the image analysis software Stream Motion 1.9.3 of Olympus Soft Imaging Solutions GmbH, Germany.

	Form factor []	**Elongation** []	**Sphericity** []	**Equivalent diameter** [µm]
Powder without influence of T	0.64 ± 0.15	1.16 ± 0.49	0.72 ± 0.22	22.89 ± 10.37
Powder with influence of T	0.63 ± 0.22	1.33 ± 0.42	0.69 ± 0.26	23.24 ± 10.88
Sintered powder	0.74 ± 0.13	1.20 ± 0.26	0.76 ± 0.20	21.90 ± 6.46

Table 10: Density measurements and geometrical factors for the specimens of printjob 1 conducted with image analysis software Stream Motion 1.9.3 of Olympus Soft Imaging Solutions GmbH, Germany; the highlighted lines indicate the specimen with the highest densities.

#	**Laser Power** [W]	**Energy Input** [J/mm³]	**Density** [%]	**Form factor** []	**Sphericity** []	**Equivalent diameter** [µm]
1.1	80	59	93.9	1.7	0.4	43.5
1.2	80	89	93.5	2.1	0.6	42.6
1.4	80	59	94.1	2.6	0.6	33.7
2.1	120	59	97.9	2.8	0.6	42.4
2.3	60	67	95.1	2.7	0.5	35.9
2.4	80	59	95.1	2.7	0.5	36.1
3.2	120	59	96.8	4.0	0.5	46.4
3.3	80	59	92.8	2.3	0.5	43.2
4.1	120	59	96.3	3.7	0.6	49.3
4.2	100	61	94.8	2.0	0.6	48.0
Mean value			95.0	2.7	0.5	42.1
Standard deviation			1.5	0.7	0.1	5.0

Table 11: Density measurements and geometrical factors for the specimens of printjob 2 conducted with image analysis software Stream Motion 1.9.3 of Olympus Soft Imaging Solutions GmbH, Germany; the highlighted lines indicate the specimen with the highest densities.

#	Laser Power	Energy Input	Density	Form factor	Sphericity	Equivalent diameter
	[W]	[J/mm³]	[%]	[]	[]	[µm]
0.1	80	59	94.6	2.6	0.5	40.3
1.1	80	59	92.7	1.2	0.5	38.1
1.2	80	89	94.4	1.1	0.6	44.0
1.3	80	59	93.7	1.2	0.5	38.4
2.1	120	59	97.1	2.5	0.6	39.1
2.2	160	59	98.7	2.4	0.6	34.4
2.3	60	67	93.4	1.1	0.6	44.5
3.2	120	59	96.4	2.6	0.6	49.5
3.3	80	59	93.3	1.2	0.6	42.0
4.2	100	61	96.8	1.1	0.5	40.0
Mean value			95.1	1.7	0.5	41.0
Standard deviation			1.9	0.7	0.1	4.0

Table 12: Density measurements and geometrical factors for the specimens of printjob 3 conducted with image analysis software Stream Motion 1.9.3 of Olympus Soft Imaging Solutions GmbH, Germany; the highlighted lines indicate the specimen with the highest densities.

#	Laser Power [W]	Energy Input [J/mm³]	Density [%]	Form factor []	Sphericity []	Equivalent diameter [µm]
0.1	120	60	98.4	1.0	0.6	30.6
0.2	140	60	99.8	1.1	0.6	18.7
1.1	160	60	99.3	0.6	0.5	32.6
1.2	120	55	99.8	1.0	0.6	19.7
1.4	160	55	99.8	1.0	0.7	26.5
2.1	120	50	98.5	0.8	0.5	37.1
2.2	140	50	98.7	1.0	0.6	24.1
2.3	160	50	99.9	0.9	0.5	16.7
2.4	120	60	98.7	0.9	0.5	25.9
3.1	120	60	99.0	0.9	0.7	36.1
3.2	120	60	99.4	1.1	0.6	21.6
3.3	120	60	99.3	0.9	0.5	25.2
3.4	120	60	98.4	0.9	0.6	34.6
4.1	140	60	99.7	1	0.7	24.2
4.2	160	60	99.4	0.6	0.2	24.9
Mean value			99.2	0.9	0.6	26.6
Standard deviation			0.6	0.1	0.1	6.2

Annex C

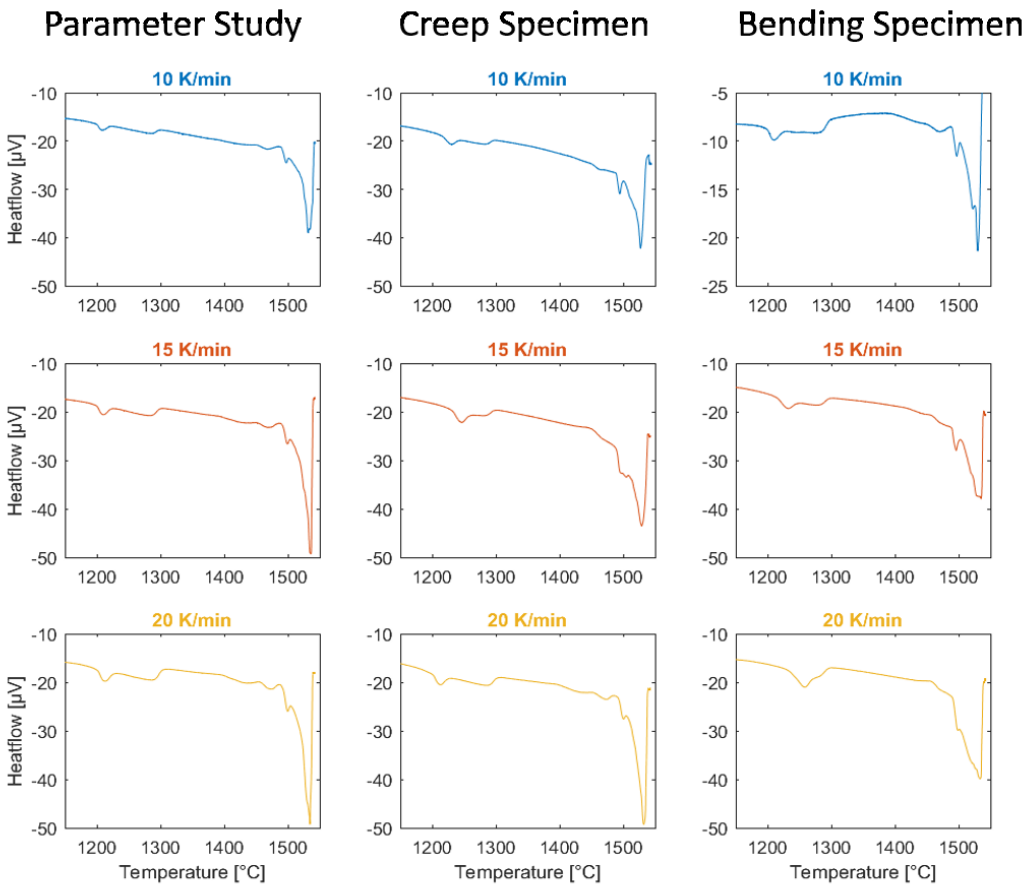

Figure 44: Overview of the measured DSC curves for the parameter study, the creep specimen and the bending specimen for heating rates of 10, 15 and 20 K/min.

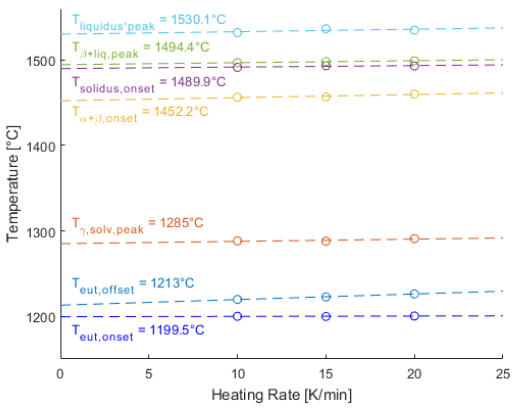

Figure 45: Measured temperatures of the parameter study of specimen 2.2 of printjob 3 for the different phase transitions by differential scanning calorimetry for heating rates of 10, 15 and 20 K/min; dotted lines are the respective linear regressions which are extrapolated to 0 K/min.

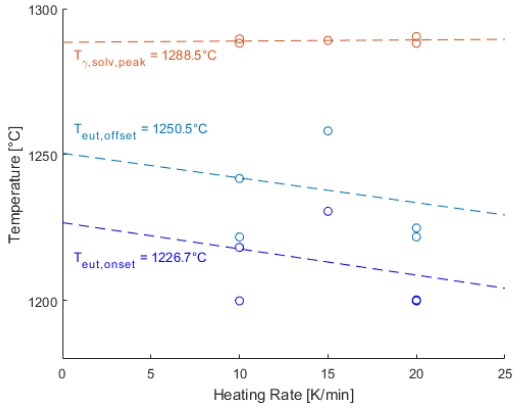

Figure 46: Measured temperatures of printjob 4 for the different phase transitions by differential scanning calorimetry for heating rates of 10, 15 and 20 K/min; dotted lines are the respective linear regressions which are extrapolated to 0 K/min.

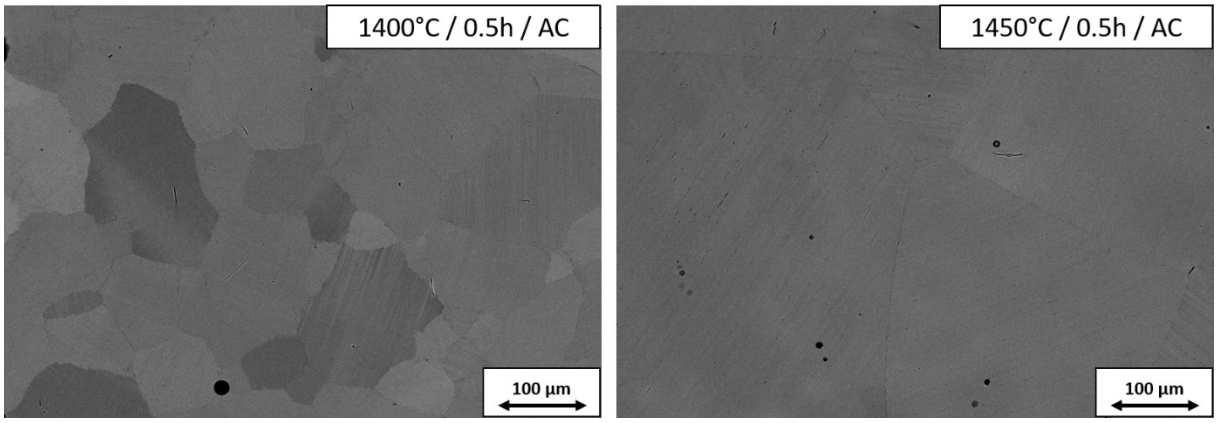

Figure 47: Microstructure of specimen 4.2 of the third printjob after 1400°C annealing for 0.5h with subsequent AC and microstructure of specimen 3.4 of the third printjob after 1450°C annealing for 0.5h and subsequent AC: both microstructures show supersaturated α_2-grains, whereas pronounced grain growth can only be seen for 1450°C annealing.

Annex D

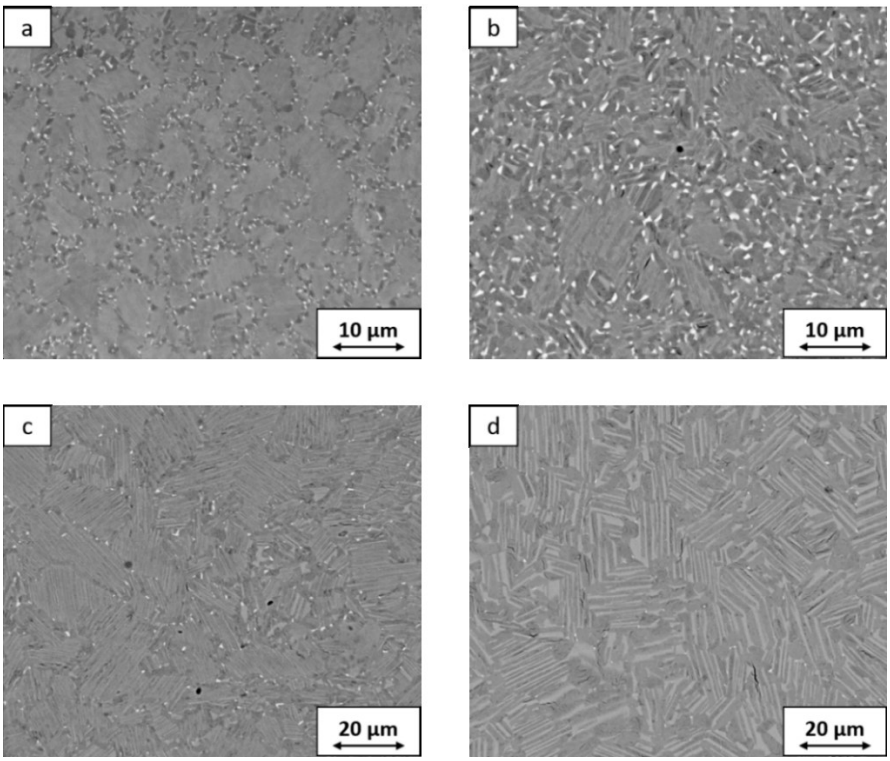

Figure 48: Microstructural comparison between the marginalized surface layer and the center of a specimen: (a) marginalized surface layer and (b) center of specimen 1.2 of printjob 1; (c) marginalized surface layer and (d) center of specimen 2.1 of printjob 2.

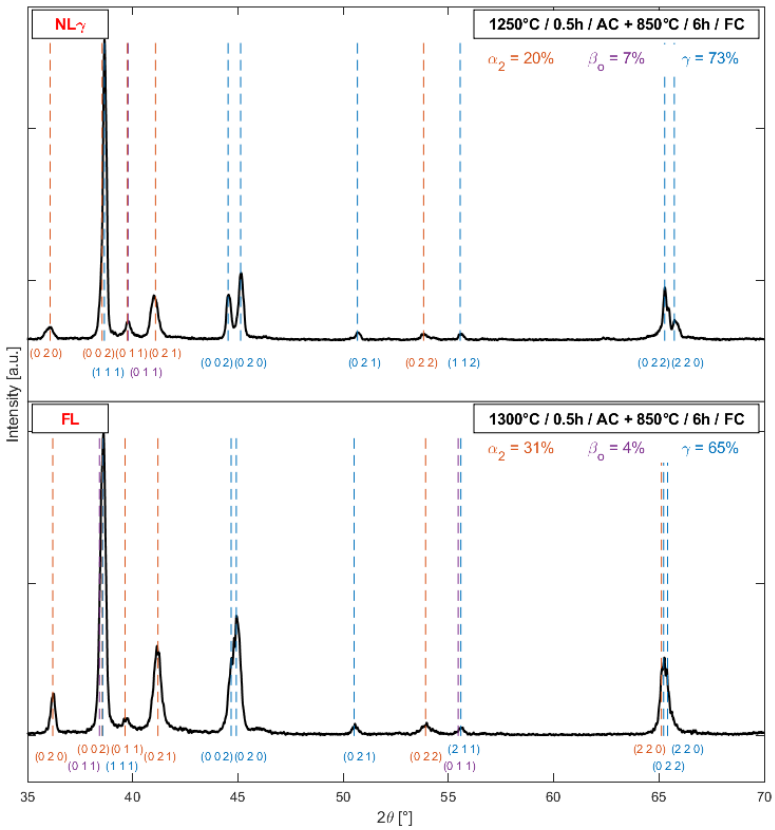

Figure 49: XRD measurements and phase fractions for the two main heat treatments investigated in this thesis.

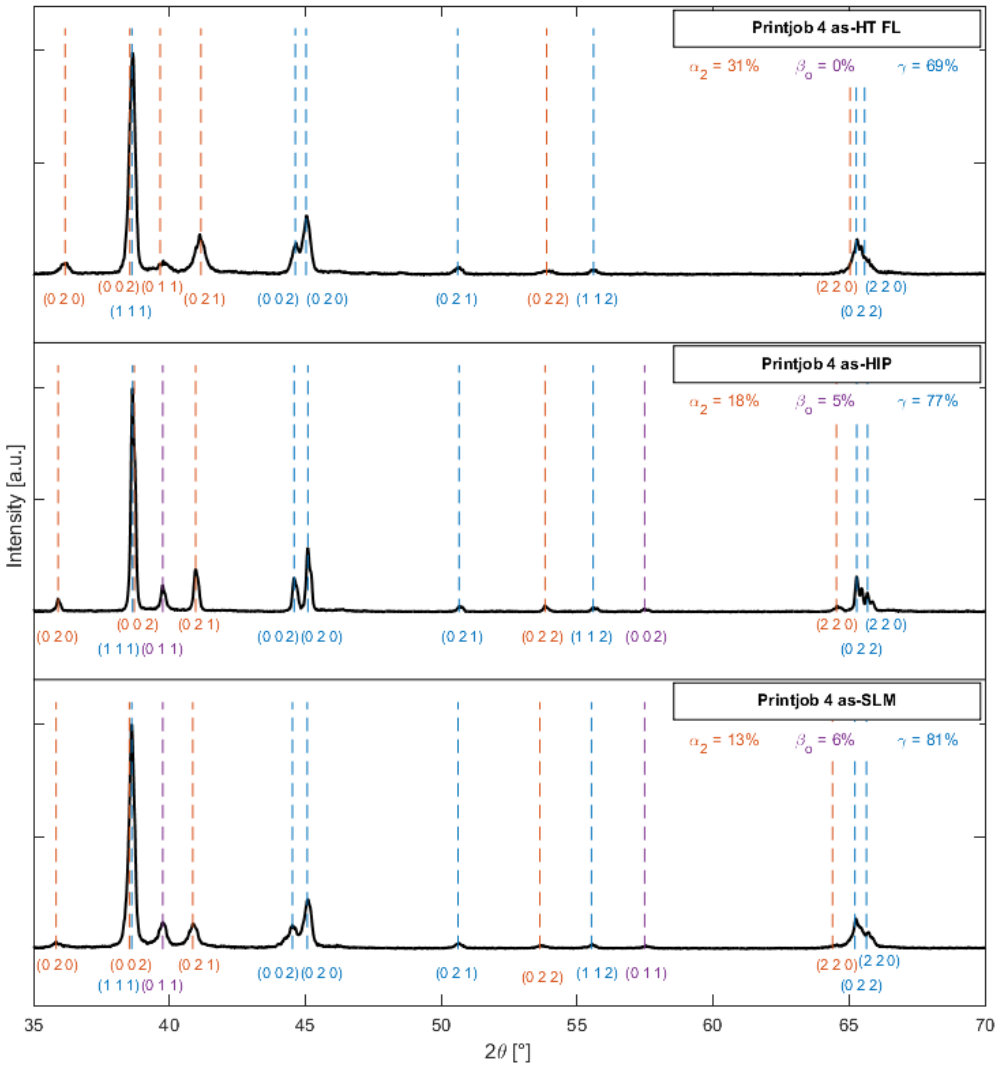

Figure 50: XRD measurements of different microstructural conditions (as-SLM, as-HIP and as-HT) together with the phase fractions.

Table 13: Hardness according to HV10 of different microstructural conditions and different printjobs.

	Printjob	Microstructure	HV10
1	4	as-SLM	465
2	4	as-HIP	362
3	4	supersaturated α_2-grains	399
4	4	FL	436
5	3	FL	420
6	1	NLγ	363

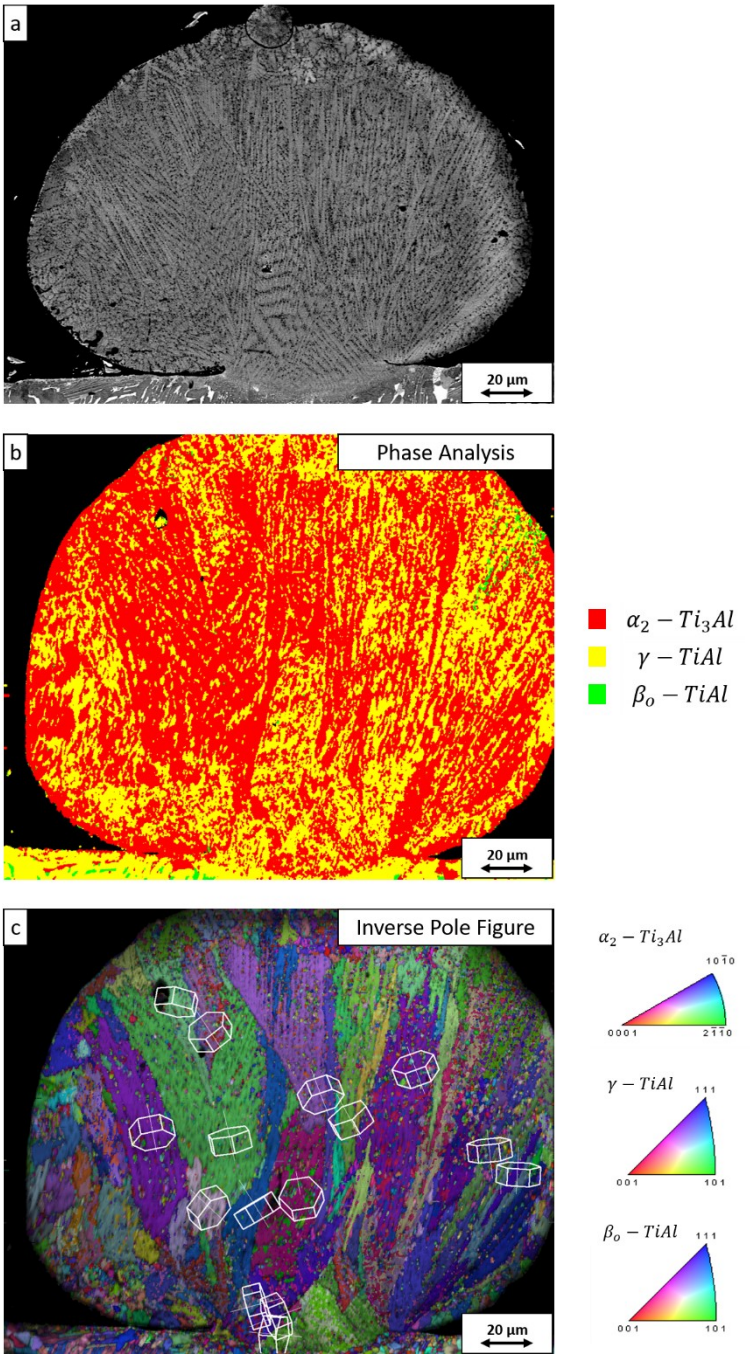

Figure 51: EBSD measurements on a Single Line Experiment: (a) SEM image of the respective single line; (b) phase analysis of the according single line, whereas the major proportion of the microstructure consists of α_2- and γ-phase; (c) Inverse Pole Figure (IPF) of the according single line with the orientations of the main hexagonal dendritic structures, whereas a growth towards the highest temperature gradient can be observed.

Annex E

Table 14: Comparison of the three-point bending tests of the TNM SLM specimens 1 – 4 wit a TNM PM reference sample and literature data.

	Microstructure []	**Stress** [MPa]
TNM SLM specimen 1	FL	906
TNM SLM specimen 2	FL	1081
TNM SLM specimen 3	FL	1008
TNM SLM specimen 4	FL	783
TNM PM	FL	898
TNM cast	FL	<900*
TNM SPS	FL	<850*

* material properties obtained by tensile tests at room temperature

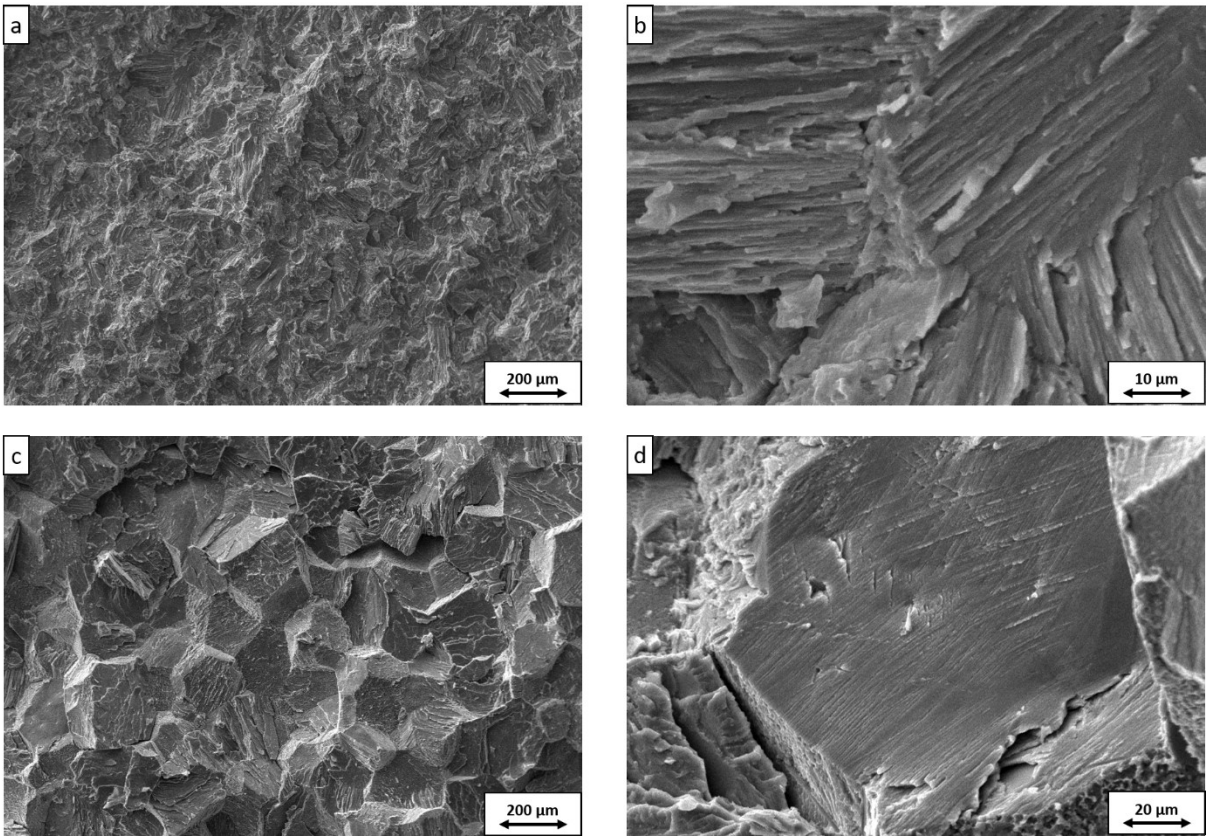

Figure 52: Fracture surfaces of the three-point bending tests: (a) overview of the fracture surface of a representative specimen revealing a brittle transgranular fracture; (b) detailed image of the fracture surface revealing a partly delamination of the single lamellas; (c) overview of the fracture surface of the TNM PM reference specimen revealing an intergranular fracture; (d) detailed image of the fracture surface.

Annex F

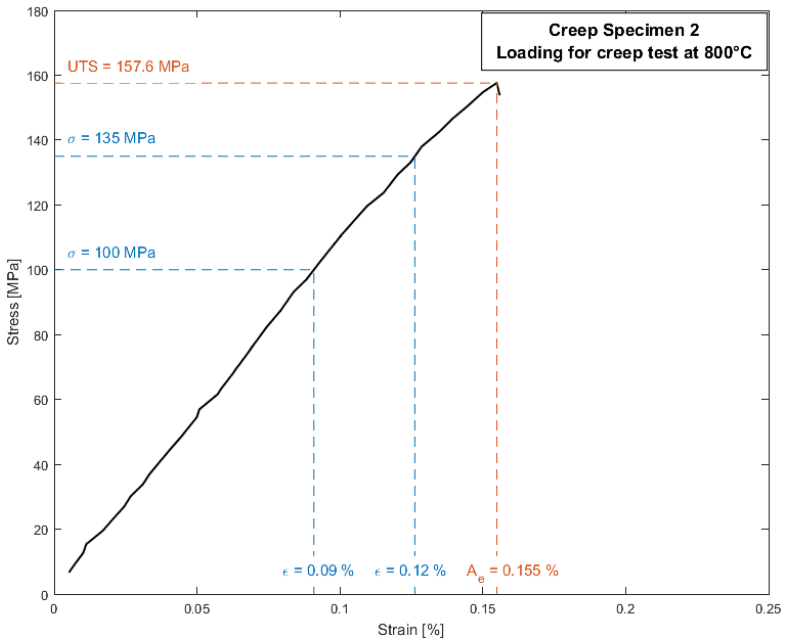

Figure 53: Recordings during loading of the creep test of creep specimen 2 at 800°C; fracture occured at a stress of 157.6 MPa with an elongation at break of 0.155%; blue marked stresses and elongations are in accordance with the creep test of specimen 3 to obtain the elastic contributions.

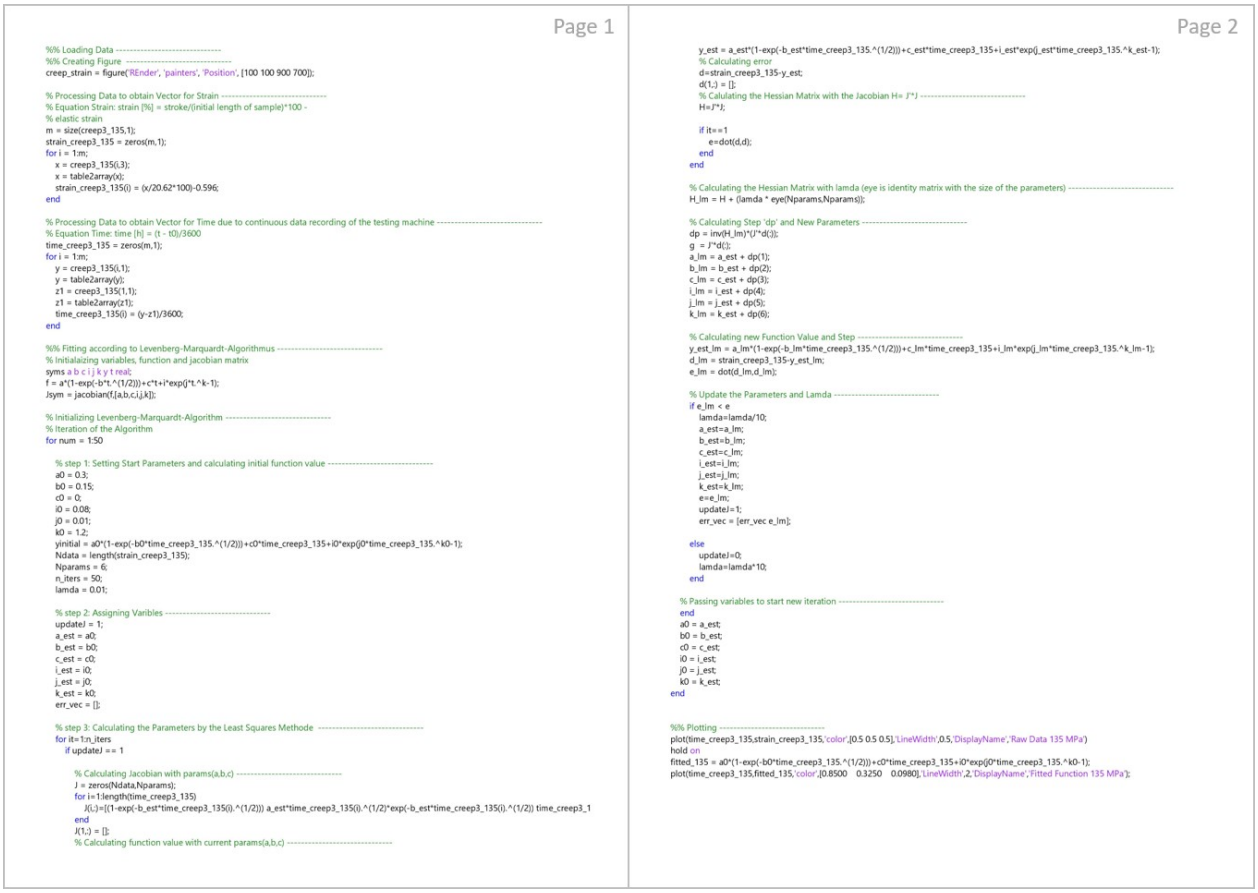

Page 1

```
%% Loading Data ------------------------------
%% Creating Figure ---------------------------
creep_strain = figure('RErender', 'painters', 'Position', [100 100 900 700]);

% Processing Data to obtain Vector for Strain ------------------------------
% Equation Strain: strain [%] = stroke/(initial length of sample)*100 -
% elastic strain
m = size(creep3_135,1);
strain_creep3_135 = zeros(m,1);
for i = 1:m;
    x = creep3_135(:,3);
    x = table2array(x);
    strain_creep3_135(i) = (x/20.62*100)-0.596;
end

% Processing Data to obtain Vector for Time due to continuous data recording of the testing machine ------------------------------
% Equation Time: time [h] = (t - t0)/3600
time_creep3_135 = zeros(m,1);
for i = 1:m;
    y = creep3_135(i,1);
    y = table2array(y);
    z1 = creep3_135(1,1);
    z1 = table2array(z1);
    time_creep3_135(i) = (y-z1)/3600;
end

%% Fitting according to Levenberg-Marquardt-Algorithmus ------------------------------
% Initialaizing variables, function and jacobian matrix
syms a b c i j k y t real;
f = a*(1-exp(-b*t.^(1/2)))+c*t+i*exp(j*t.^k-1);
Jsym = jacobian(f,[a,b,c,i,j,k]);

% Initializing Levenberg-Marquardt-Algorithm ------------------------------
% Iteration of the Algorithm
for num = 1:50

    % step 1: Setting Start Parameters and calculating initial function value ------------------------------
    a0 = 0.3;
    b0 = 0.15;
    c0 = 0;
    i0 = 0.08;
    j0 = 0.01;
    k0 = 1.2;
    yinitial = a0*(1-exp(-b0*time_creep3_135.^(1/2)))+c0*time_creep3_135+i0*exp(j0*time_creep3_135.^k0-1);
    Ndata = length(strain_creep3_135);
    Nparams = 6;
    n_iters = 50;
    lamda = 0.01;

    % step 2: Assigning Varibles ------------------------------
    updateJ = 1;
    a_est = a0;
    b_est = b0;
    c_est = c0;
    i_est = i0;
    j_est = j0;
    k_est = k0;
    err_vec = [];

    % step 3: Calculating the Parameters by the Least Squares Methode ------------------------------
    for it=1:n_iters
        if updateJ == 1

            % Calculating Jacobian with params(a,b,c) ------------------------------
            J = zeros(Ndata,Nparams);
            for i=1:length(time_creep3_135)
                J(i,:)=[(1-exp(-b_est*time_creep3_135(i).^(1/2))) a_est*time_creep3_135(i).^(1/2)*exp(-b_est*time_creep3_135(i).^(1/2)) time_creep3_1
            end
            J(1,:) = [];
            % Calculating function value with current params(a,b,c) ------------------------------
```

Page 2

```
            y_est = a_est*(1-exp(-b_est*time_creep3_135.^(1/2)))+c_est*time_creep3_135+i_est*exp(j_est*time_creep3_135.^k_est-1);
            % Calculating error
            d=strain_creep3_135-y_est;
            d(1,:) = [];
            % Calulating the Hessian Matrix with the Jacobian H= J'*J ------------------------------
            H=J'*J;

            if it==1
                e=dot(d,d);
            end
        end

        % Calculating the Hessian Matrix with lamda (eye is identity matrix with the size of the parameters) ------------------------------
        H_lm = H + (lamda * eye(Nparams,Nparams));

        % Calculating Step 'dp' and New Parameters ------------------------------
        dp = inv(H_lm)*(J'*d());
        g  = J'*d();
        a_lm = a_est + dp(1);
        b_lm = b_est + dp(2);
        c_lm = c_est + dp(3);
        i_lm = i_est + dp(4);
        j_lm = j_est + dp(5);
        k_lm = k_est + dp(6);

        % Calculating new Function Value and Step ------------------------------
        y_est_lm = a_lm*(1-exp(-b_lm*time_creep3_135.^(1/2)))+c_lm*time_creep3_135+i_lm*exp(j_lm*time_creep3_135.^k_lm-1);
        d_lm = strain_creep3_135-y_est_lm;
        e_lm = dot(d_lm,d_lm);

        % Update the Parameters and Lamda ------------------------------
        if e_lm < e
            lamda=lamda/10;
            a_est=a_lm;
            b_est=b_lm;
            c_est=c_lm;
            i_est=i_lm;
            j_est=j_lm;
            k_est=k_lm;
            e=e_lm;
            updateJ=1;
            err_vec = [err_vec e_lm];

        else
            updateJ=0;
            lamda=lamda*10;
        end

    % Passing variables to start new iteration ------------------------------
    end
    a0 = a_est;
    b0 = b_est;
    c0 = c_est;
    i0 = i_est;
    j0 = j_est;
    k0 = k_est;
end


%% Plotting ------------------------------
plot(time_creep3_135,strain_creep3_135,'color',[0.5 0.5 0.5],'LineWidth',0.5,'DisplayName','Raw Data 135 MPa')
hold on
fitted_135 = a0*(1-exp(-b0*time_creep3_135.^(1/2)))+c0*time_creep3_135+i0*exp(j0*time_creep3_135.^k0-1);
plot(time_creep3_135,fitted_135,'color',[0.8500  0.3250  0.0980],'LineWidth',2,'DisplayName','Fitted Function 135 MPa');
```

Figure 54: Examplary Levenberg-Marquardt-Algorithm to evaluate the creep test at 800°C and 135 MPa.

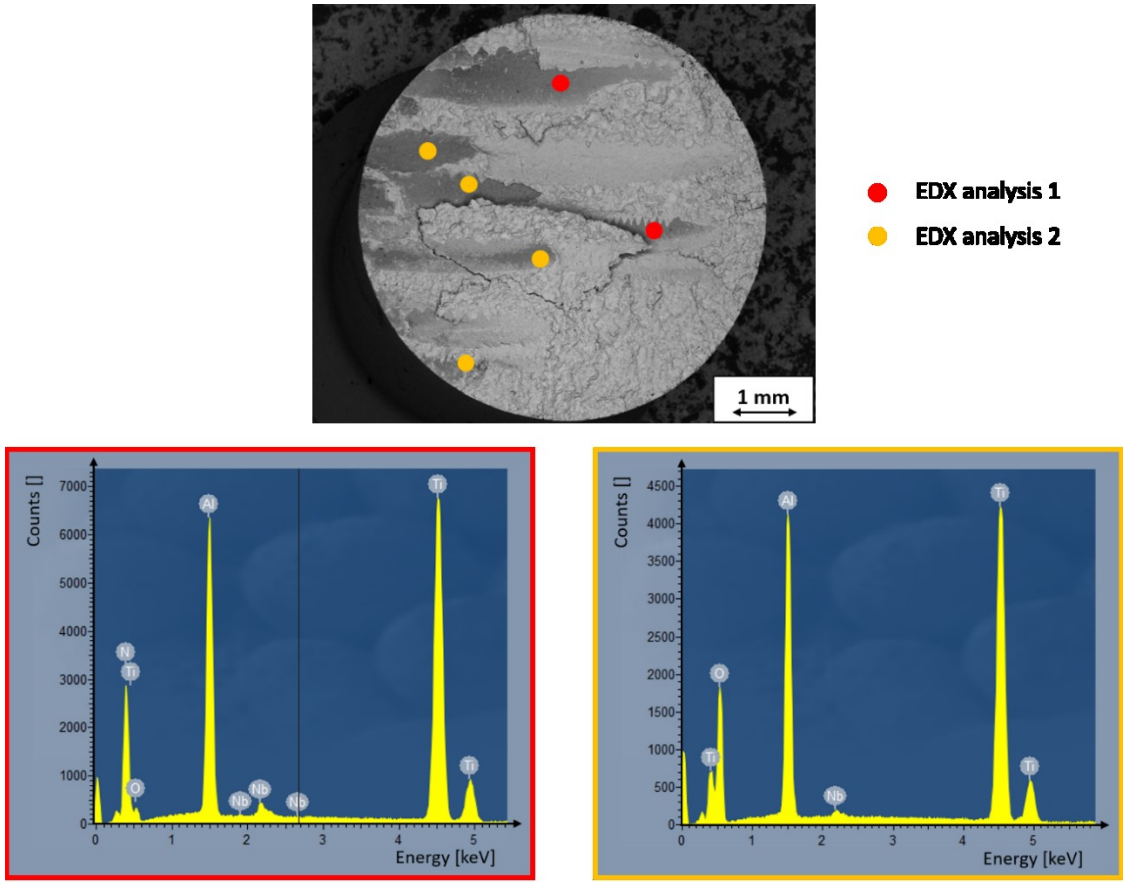

Figure 55: EDX spectra of the fracture surface of creep specimen 1 revealed major proportions of Oxide and Nitride layers.

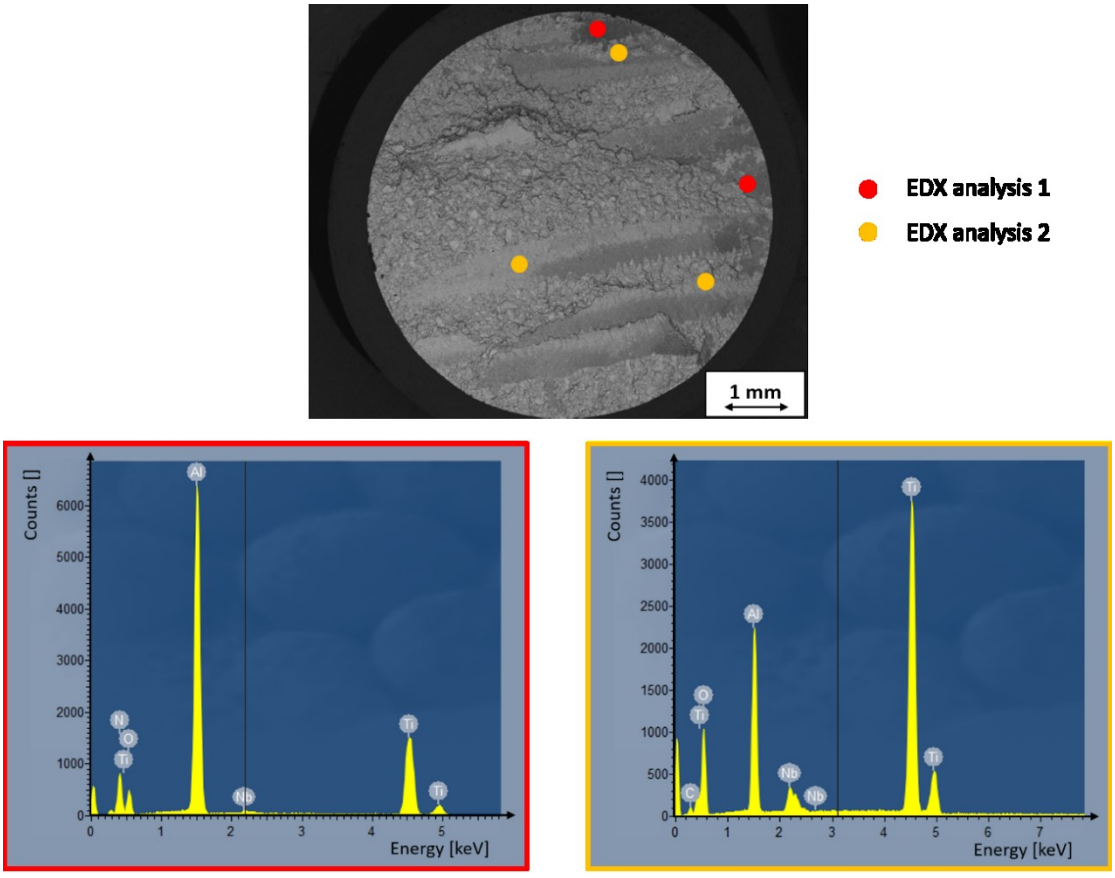

Figure 56: EDX spectra of the fracture surface of creep specimen 2 revealed major proportions of Oxide and Nitride layers.

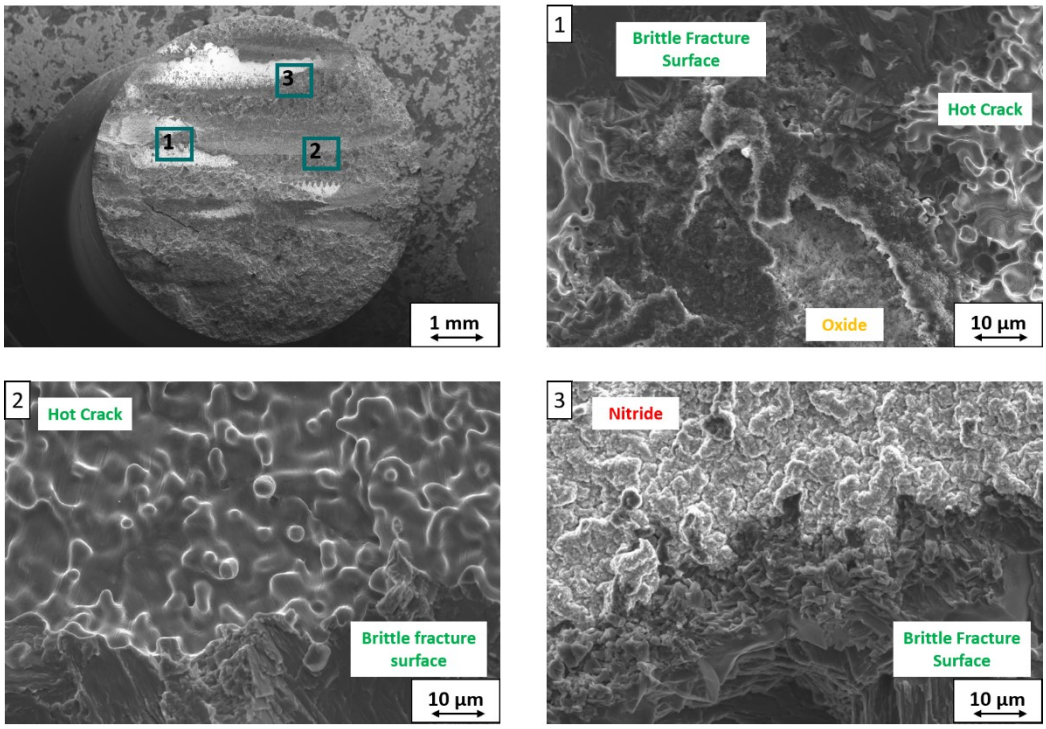

Figure 57: SEM images taken at the fracture surface of the creep specimen 1 revealing brittle fracture surfaces, similar to hot cracks, oxides and nitrides.

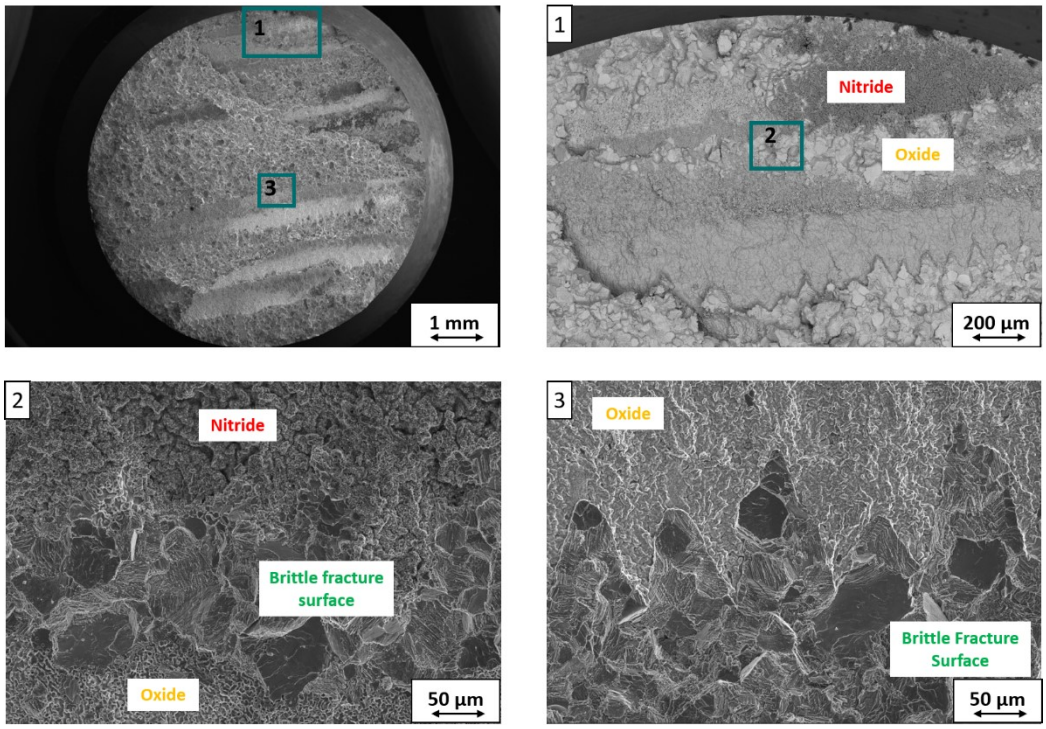

Figure 58: SEM images taken at the fracture surface of the creep specimen 2 revealing brittle fracture surfaces, similar to hot cracks, oxides and nitrides.

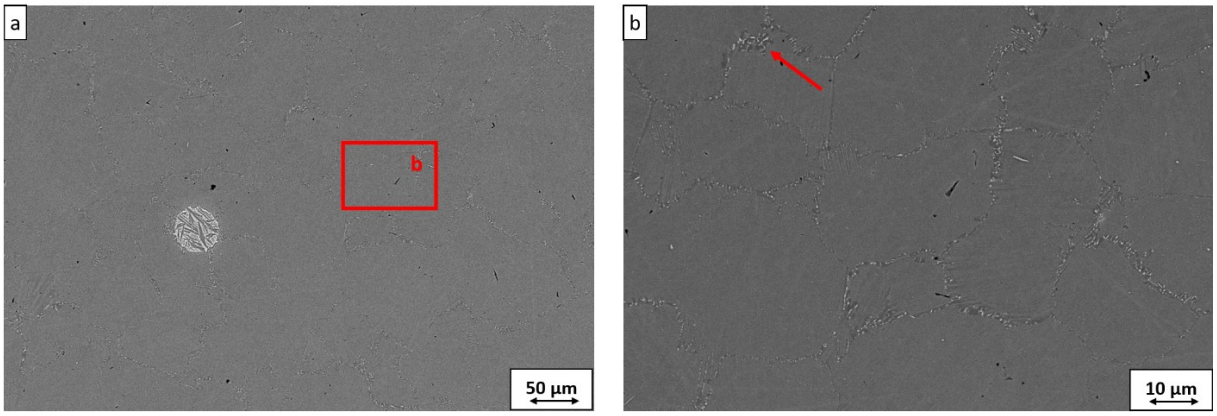

Figure 59: SEM image of the creep specimen 3 after creep testing with an overall testing time of 385h at 800°C: (a) giving an overview with a clearly visible Mo particle, small rounded shaped pores due to the creep testing and elongated shaped pores due to lack of fusions; (b) giving a detailed image of the microstructure showing a major amount of cellular reactions at the grain boundaries (red arrow).